1-1-2018

Development of Low Frequency Electron Paramagnetic Resonance Methods and Instrumentation for Biological Applications

Laura A. Buchanan
University of Denver

Recommended Citation

Buchanan, Laura A., "Development of Low Frequency Electron Paramagnetic Resonance Methods and Instrumentation for Biological Applications" (2018). *Electronic Theses and Dissertations*. 1535.
https://digitalcommons.du.edu/etd/1535

Development of Low Frequency Electron Paramagnetic Resonance Methods and Instrumentation for Biological Applications

Abstract

EPR is a powerful biophysical tool that can be used to measure tumor physiology. With the addition of magnetic field gradients, the spectral properties of paramagnetic species can be mapped. To facilitate EPR imaging, methods and instrumentation at frequencies between 250 MHz and 1 GHz were developed.

At low spin concentrations, the rapid scan background signal is often many times larger than the EPR signal of interest. To help remove the background contribution, a data acquisition procedure that takes advantage of a cross-loop resonator and bipolar power supplies was developed at 250 MHz. In this procedure, two scans are collected. Relative to the first scan, in the second scan the magnetic field (B_0) is reversed and the phase of the rapid scan field is offset by 180°. This results in an inversion of the EPR signal and no net change to the background. The difference between the scans is calculated to cancel the background and enhance the EPR signal by the square root of 2. The procedure was also applied to data at 700 MHz and 980 MHz.

A table-top arbitrary waveform generator (AWG) based rapid scan and pulse spectrometer was designed to operate at frequencies between 700 MHz and 1 GHz using both cross-loop and reflection resonators. The frequency range was selected to provide adequate signal to noise and an imaging penetration depth appropriate for imaging mice. Characterization of the spectrometer including the noise figure, gain, magnetic field homogeneity, source noise, resonators, and gradient fields is reported. To demonstrate the imaging capabilities of the instrument, rapid scan images were collected of nitroxide and trityl radicals *in vitro* up to 4 dimensions.

New methods were tested that use rapid scan, frequency steps, and field jumps to measure electron spin lattice relaxation (T_1) at 1 GHz. Overall good agreement of the relaxation times was observed between the new methods and conventional techniques. However, the uncertainty associated with the rapid scan method is greater due to the low number of points that define the recovery curve. In the frequency stepped method, the resonator bandwidth limits samples to ones with narrow lines. Preliminary results of the field jump method are presented.

Finally, excitation bandwidth and power requirements of a new exponential sine shaped pulse produced with an AWG are compared to conventional rectangular pulses at 1.5 GHz. For the same amount of power, a higher resonator Q can be utilized with the exponential sine pulse yielding higher sensitivity and an increased excitation uniformity.

Document Type

Dissertation

Degree Name

Ph.D.

Department

Chemistry and Biochemistry

First Advisor

Sandra S. Eaton, Ph.D.

Second Advisor

Gareth Eaton, Ph.D.

Third Advisor

Martin Margittai, Ph.D.

Keywords

Arbitrary waveform generator, EPR, Electron paramagnetic resonance, Imaging, Pulse shaping, Rapid scan

Subject Categories

Biomedical Devices and Instrumentation | Biophysics | Medical Biophysics

Publication Statement

Development of Low Frequency Electron Paramagnetic Resonance Methods and Instrumentation for Biological Applications

---

A Dissertation

Presented to

the Faculty of Natural Sciences and Mathematics

University of Denver

In Partial Fulfillment

of the Requirements for the Degree

Doctor of Philosophy

---

by

Laura A. Buchanan

November 2018

Advisor: Sandra S. Eaton

Author: Laura A. Buchanan
Title: Development of Low Frequency Electron Paramagnetic Resonance Methods and Instrumentation for Biological Applications
Advisor: Sandra S. Eaton
Degree Date: November 2018

Abstract

EPR is a powerful biophysical tool that can be used to measure tumor physiology. With the addition of magnetic field gradients, the spectral properties of paramagnetic species can be mapped. To facilitate EPR imaging, methods and instrumentation at frequencies between 250 MHz and 1 GHz were developed.

At low spin concentrations, the rapid scan background signal is often many times larger than the EPR signal of interest. To help remove the background contribution, a data acquisition procedure that takes advantage of a cross-loop resonator and bipolar power supplies was developed at 250 MHz. In this procedure, two scans are collected. Relative to the first scan, in the second scan the magnetic field (B_0) is reversed and the phase of the rapid scan field is offset by 180°. This results in an inversion of the EPR signal and no net change to the background. The difference between the scans is calculated to cancel the background and enhance the EPR signal by the square root of 2. The procedure was also applied to data at 700 MHz and 980 MHz.

A table-top arbitrary waveform generator (AWG) based rapid scan and pulse spectrometer was designed to operate at frequencies between 700 MHz and 1 GHz using both cross-loop and reflection resonators. The frequency range was selected to provide adequate signal to noise and an imaging penetration depth appropriate for imaging mice. Characterization of the spectrometer including the noise figure, gain, magnetic field homogeneity, source noise, resonators, and gradient fields is reported. To demonstrate the imaging capabilities of the instrument, rapid scan images were collected of nitroxide and trityl radicals *in vitro* up to 4 dimensions.

New methods were tested that use rapid scan, frequency steps, and field jumps to measure electron spin lattice relaxation (T_1) at 1 GHz. Overall good agreement of the relaxation times was observed between the new methods and conventional techniques. However, the uncertainty associated with the rapid scan method is greater due to the low number of points that define the recovery curve. In the frequency stepped method, the resonator bandwidth limits samples to ones with narrow lines. Preliminary results of the field jump method are presented.

Finally, excitation bandwidth and power requirements of a new exponential sine shaped pulse produced with an AWG are compared to conventional rectangular pulses at 1.5 GHz. For the same amount of power, a higher resonator Q can be utilized with the exponential sine pulse yielding higher sensitivity and an increased excitation uniformity.

Acknowledgements

Thank you to Drs. Sandra and Gareth Eaton for your constant support and guidance over the past 5 years. The work presented in this dissertation was financially supported by NIH NCI AIP grant CA177744 awarded to Gareth and Sandra Eaton and by NIH P41EB002034 awarded to Howard Halpern.

Thanks to my committee: Dr. Martin Margittai, Dr. Dinah Loerke, and Dr. David Patterson and external chair Dr. Peter Laz.

I would like to thank Dr. George Rinard for the countless simulations and theoretical work that laid the foundation for many of my experiments. My sincere thanks to Richard Quine who helped with the instrument design, construction, and for the many hours spent trouble shooting with me. In the words of the wise man, “When nothing works at all, you just have to get back to something that does.”

Thanks to Dr. Josh Biller for teaching me how to spell EPR and to Dr. Zhelin Yu for taking time to help me with Python and Matlab programming. Thanks to my colleagues, Yilin Shi, Joseph McPeak, and Lukas Woodcock for working with me on many projects.

I also would like to thank my family for their support over the past five years. Lastly, I would like to thank my husband, James Bench, who encouraged and supported me every step of the way.

Table of Contents

List of Figures

List of Tables

Chapter 1: Introduction to EPR

1.1 Motivation

Electron paramagnetic resonance (EPR) is a widely used biophysical technique that yields vital information about biological systems. The spectral characteristics of molecular probes containing unpaired electrons are used to monitor environments of interest, typically through change in electron spin relaxation rates, hyperfine couplings, or line shape. EPR can be used to probe distance distributions between spin labels on a protein, trap free radical species significant to biological systems, determine ligand binding environment, or for imaging [1-4]. The focus of this dissertation will be developing methods and instrumentation central to EPR imaging.

Multidimensional EPR imaging has the power to spatially resolve dynamic spectral properties of molecular probes yielding a wealth of information including the local oxygen concentration, redox and pH status within tissue [5-7]. Frequencies between 250 MHz and 1 GHz are typically chosen for EPR imaging. The selection of frequency for imaging is a tradeoff between signal to noise, which increases with increasing frequency, and depth of penetration, which decreases with increasing frequency [8]. The depth of penetration decreases from approximately 7 cm at 250 MHz to 1 cm at 1 GHz in water and fat tissue. This range of frequencies permits imaging small animals such as mice and rabbits.

To perform in vivo EPR imaging, an EPR active probe must be injected into the patient or animal. Some probes are more appropriate than others for measuring oxygen concentration. Triarylmethyl molecules are carbon-based radicals with a narrow line EPR spectrum [9]. The spectral line width of these molecules broadens due to collisions with molecular oxygen in its triplet state. With proper calibration, these molecules are accurate reporters of local oxygen concentration [10]. Their relative stability, long relaxation time, sensitivity to oxygen, and simple spectra make them ideal candidates for oximetry studies.

There are no commercial EPR imaging spectrometers available below 1 GHz. The development of a 700 MHz to 1 GHz rapid scan and pulse EPR imaging spectrometer described in chapter 3 is done in collaboration with Bruker Biospin, the University of Chicago, and the University of Maryland. Of central interest to the collaborations is the ability to perform quantitative imaging of oxygen in tumors. Local oxygen concentration within a tumor is crucial knowledge for physicians who deliver radiation therapy. In 1955 it was reported that local oxygen concentration varied spatially within a tumor and could possibly have implications for radiation treatment of tumors [11, 12]. Since then, it has been shown that some tumors contain regions of low oxygen concentration that are resistant to radiation [13]. Although a variety of chemical, optical, nuclear and magnetic techniques exist for measuring oxygen concentration, EPR is positioned as a quantitative, potentially relatively inexpensive, non-invasive technique by which to assess levels of local oxygen concentration. Precise knowledge of oxygen concentration is valuable for designing targeted radiation therapy plans and creating better patient outcomes.

1.2 Differences between NMR and EPR

Given the popularity of nuclear magnetic resonance (NMR), it is useful to start the discussion of EPR by considering the similarities and differences between the two. EPR and NMR share many of the same fundamental theories and are complimentary techniques, but also have key differences. Most fundamentally, NMR studies nuclear spins exclusively and EPR studies unpaired electron spins. In many ways, EPR borrows from NMR but lags behind in development waiting for technological advances.

One difference between the two techniques is sensitivity which is determined by the larger gyromagnetic ratio, γ, the electron has compared to the proton. The gyromagnetic ratio, γ, of a particle relates the magnetic moment of a charged particle to its spin angular momentum and can be defined as the Larmor frequency divided by the external magnetic field B_0, expressed in units of $\frac{\text{rad}}{\text{s}*\text{T}}$. The electron has a gyromagnetic ratio ~ 1.76 x 10^{11} $\frac{\text{rad}}{\text{s}*\text{T}}$. and the proton has a value of 2.6752 x 10^{8} $\frac{\text{rad}}{\text{s}*\text{T}}$. The ratio between the two is ~ 660, giving the electron a much higher sensitivity than the proton for a given spin concentration. To make up for this, NMR spin concentrations are typically in the molar (M) range while EPR is in the mM range. EPR is not studied in higher concentrations due to the shortened relaxation times that makes pulse EPR challenging and exchange broadening in continuous wave (CW) EPR. The gyromagnetic ratio can be expressed in terms of $\gamma/2\pi$ such that the units become frequency divided by magnetic field strength. This is a useful conversion factor for finding the resonant magnetic field for a given microwave or radio frequency. For example, at 1 GHz, the corresponding EPR field would be 355 Gauss (G) while the NMR field would be 235,000 G! (1 G = 1 x 10^{-4} T)

Another difference between NMR and EPR is the timescale on which relaxation occurs. Protons in diamagnetic species have millisecond to second spin relaxation times while electron spin relaxation times of organic radicals typically range from nanoseconds to microseconds at room temperature. For this reason, development of pulsed EPR spectrometers has experienced technical delays. As instrumentation has improved over the years, more EPR pulse spectrometers have become available. The bandwidths required for EPR are much larger compared to NMR. NMR deals with spectral splitting of kHz, while EPR it is on the order of MHz. Difficulty in generating pulses to uniformly excite such large bandwidths is another reason pulsed EPR has lagged behind pulsed NMR in terms of development.

1.3 EPR Theory

Unpaired electrons have an intrinsic property called spin ($\vec{S}$). The spin quantum number, m_s, represents the spin angular momentum of the electron. According to quantum

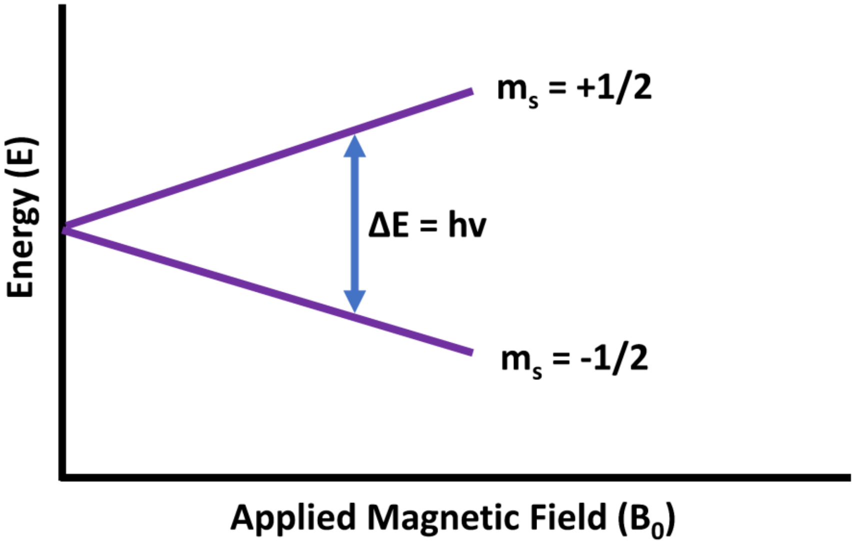

Figure 1.1: Energy level splitting diagram for a free electron.

mechanics, free electrons have two possible spin states with projections on the external field of m_s = +/- ½. These states are degenerate in the absence of a magnetic field. When placed in an external magnetic field, unpaired electrons align either parallel or anti-parallel with the external magnetic field, splitting the degeneracy into two discrete energy states. This splitting is called the Zeeman effect (Figure 1.1). The upper energy state with higher energy and quantum number, $m_s = +½$ is aligned against the field. The alignment of the spin vector with the field represents the lower energy state of the two, $m_s = -½$. The population difference between the two energy states, n_{upper} and n_{lower}, can be described with a Maxwell-Boltzmann distribution:

$$\frac{n_{\mathrm{upper}}}{n_{\mathrm{lower}}} = e^{\frac{-h\upsilon}{kT}} \qquad \text{eq. 1.1}$$

where h is Plank's constant, υ is microwave frequency, k is the Boltzmann constant, and T is temperature in Kelvin. At equilibrium, there is a small population difference between the two states that depends on temperature and the energy gap between the two states. At X-band, at room temperature, the population difference is less than 1%. Thus, the net spin transition that is observed with EPR is a very small fraction of the total number of spins. The energy difference between the two states increases linearly with respect to the external magnetic field, B_0, as depicted in Figure 1.1. The energy difference between the two states with relationship to the magnetic field is described by equation 1.2:

$$\Delta E = g\beta B \qquad \text{eq. 1.2}$$

where g is a unitless property of the unpaired electron that arises from both spin and orbital angular momentum. The g-factor varies for different molecules and is a reporter of electronic environment. The Bohr Magneton, β, is a constant that describes the magnetic moment of an unpaired electron. Resonance is achieved when the microwave energy applied, hυ, matches the energy difference between the spin states induced by the external magnetic field. When the applied microwave power is too high relative to the spin relaxation the population difference can be disturbed from equilibrium resulting in saturation.

We know from NMR that nuclei of certain elements including H, ^{13}C, and ^{14}N also have quantum mechanical spin ($\vec{I}$). Because protons and electrons have a magnetic dipole, they produce a small local magnetic field. Hyperfine interactions occur when a nuclear spin interacts with a neighboring electron spin. A simple example of a hyperfine interaction is that of an unpaired electron (S= ½) with a ^{14}N nucleus (I=1). A ^{14}N nucleus with I = 1 has spin states m_I of +1, 0, -1. This leads to an additional splitting of the Zeeman energy (Figure 1.2). The selection rule of $\Delta m_i = 0$ means that three EPR transitions are possible and a spectrum with three lines is observed.

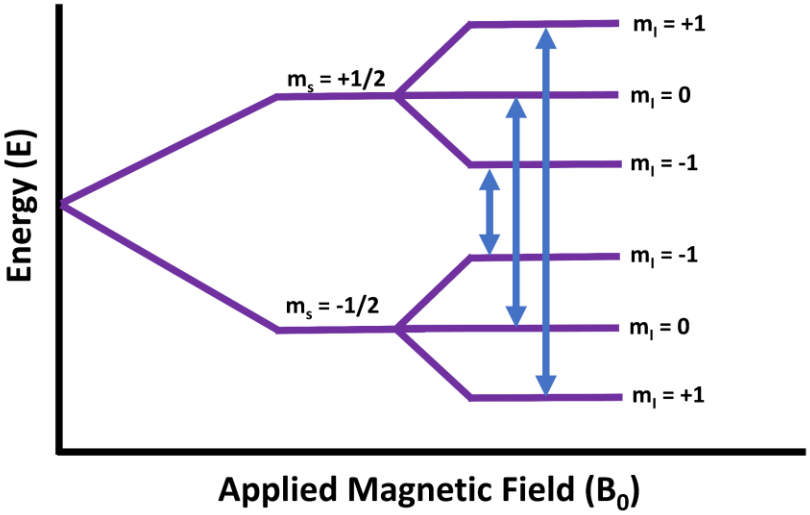

Figure 1.2: Energy level diagram of an unpaired electron coupled to one ^{14}N nucleus.

1.4 Continuous Wave EPR

In a standard CW EPR experiment, the magnetic field is slowly stepped though resonance while the microwave frequency is held constant. This technique is most commonly performed between 9 to 10 GHz because that was the frequency at which commercial instruments were first sold. In a CW experiment, the field is simultaneously modulated as it is stepped, typically at 100 kHz, and the spectrum is detected as a first derivative of the absorption spectrum using a 100 kHz phase lock-in detection system. Since the detection bandwidth is very narrow, much of the high frequency noise is discarded. CW EPR spectra are useful for extracting hyperfine, g values, and line shapes which yield information about the mobility and electronic environment of the molecule.

1.5 Pulse EPR

The laboratory magnetic field is conventionally defined as the Z axis. In pulsed EPR, a static magnetic field is applied and short microwave pulses are applied to tip the net magnetization of the spins into the X-Y plane, which is also referred to as the detection plane. The simplest pulse experiment is one which consists of only a single pulse. A typical single pulse experiment would use a π/2 pulse. A perfect π/2 pulse places the spins in the detection plane where they immediately begin to relax back to equilibrium. The net magnetization begins to de-phase rotating around the Z axis, creating a free induction decay (FID). The frequency of the FID contains information about how far offset from resonance the magnetic field is for a given microwave excitation frequency.

A two-pulse experiment consists of two pulses separated by a time, τ, to create an echo (Figure 1.3) in an ensemble of spins with a distribution of resonance frequencies. The first pulse is typically π/2 which places the spins into the X-Y plane. A perfect π/2 pulse gives the maximum signal amplitude. After each pulse the spins immediately begin to de-phase. Some time, τ, later a π pulse is applied to refocus the spins, creating an echo. During the refocusing period, the spins that were moving slowly away from each other are now moving faster towards the same point. When they have refocused completely, the peak of the echo is observed (Figure 1.3). This occurs at time, τ, measured from the center of the second pulse. Incrementing the time, τ, between the pulses increases the time during which the spins are allowed to de-phase before being refocused. This leads to less coherence between the spins resulting in a decreased echo amplitude. The amplitude of the echo signal is proportional to the number of spins that were refocused.

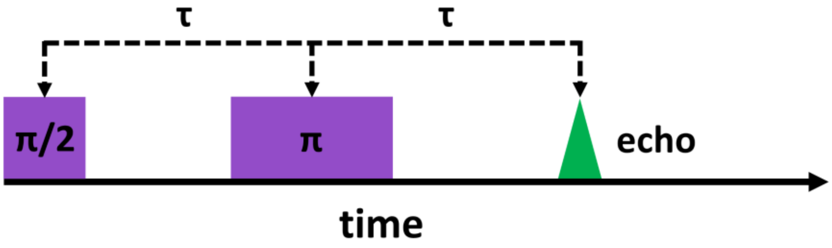

Figure 1.3: Typical two pulse spin echo sequence. The time, τ, between the pulses is from center to center of the pulses. An echo is observed at time, τ, from the center of the second pulse. T_2 is measured by observing the change in the echo amplitude as a function of 2τ.

Relaxation Times T_1 and T_m

Pulse experiments are used to directly measure electron relaxations times T_1 and T_2 as defined in the Bloch equations [14]. T_1 is the electron spin-lattice relaxation time and can be described as the time it takes for the net magnetization to return to thermal equilibrium by releasing energy to the environment. T_2, or spin-spin relaxation, is the process by which the net magnetization in the X-Y plane randomizes. It reveals information about neighboring spins within the system, whether they be electron or nuclear spins. T_2 is especially sensitive to concentration and temperature effects as well as mobility of the molecule. Because many processes affect T_2, it is rare that the true T_2 of the Bloch equations is measured but rather T_m, the phase memory time, which considers all processes that affect echo dephasing. In a 2-pulse experiment, T_m is measured by fitting the echo decay amplitude plotted as function of 2τ with an exponential (Figure 1.3).

T_1 can be measured via a 3-pulse experiment called inversion recovery. The sequence of pulses is shown in Figure 1.4 for an inversion recovery experiment. The first π pulse is used to invert the spins along the -Z axis. Ideally, the pulse is short enough to uniformly invert all spins in the spectrum. The time, T, between the first and second pulses is varied. The second and third pulses are a spin-echo detection sequence to monitor echo amplitude. The initial echo when T is short is inverted signifying that the net magnetization is in the -Z direction. As T is incrementally increased, the echo amplitude increases from -Z to +Z. The return of magnetization to the +Z axis plotted as a function of T can be fit with an exponential decay to find T_1.

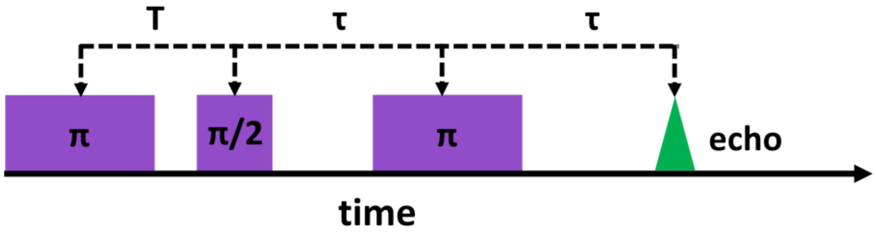

Figure 1.4: Typical three pulse inversion recovery experiment. The time, T, between the pulses is from center to center of the first two pulses. T_1 is measured by observing the change in the echo amplitude as a function of T.

Inversion recovery experiments are sensitive to spectral diffusion which can lead to measuring a time constant that is shorter than the true T_1. Spectral diffusion is the transfer of energy from excited spin packets to spins that are not on resonance. This is especially problematic in inversion recovery experiments in which the pulse does not excite the entire bandwidth of the spectrum or the excitation profile of the pulse is nonuniform.

Saturation Recovery

Instead of using a 3-pulse experiment to measure T_1, a technique called saturation recovery can be used. In this technique, a long saturating pulse at relatively high B_1 is applied. This is followed by a low power continuous wave observe period. The low power is needed to decrease the degree of saturation and allow the spins to return to equilibrium with minimum perturbation. Power is not completely turned off in order to keep a measurable projection of the magnetization in the X-Y plane. Saturation recovery typically has low-signal to noise due to the low power used during the observe period. The signal to noise in a saturation recovery experiment is lower than what would be observed in a standard CW experiment performed at the same power because saturation recovery does not use field modulation or lock-in detection.

1.6 Rapid Scan EPR

Rapid scan (RS) EPR is a technique that has been rigorously developed in the Eaton lab over the last two decades [15-22]. The signature “wiggles” in rapid scan NMR were first described by Bloembergen et. al in 1948 [23]. The wiggles are removed using deconvolution to yield the slow scan spectrum. In rapid scan EPR, the microwave frequency is held constant while the magnetic field is swept back and forth rapidly compared to T_2. Scanning through resonance faster than the spins can relax requires that the transient signal be deconvolved to recover the slow-scan spectrum. It is advantageous to scan rapidly in order to collect many averages in a small amount of time. Also, because the time spent on resonance is a small portion of the entire scan, a higher microwave power can be used in RS compared to CW. Rapid scan uses quadrature direct-detection, so a lock-in detection amplifier is not needed. The absorption signal and dispersion signals are collected in rapid scan. By combining the two quadrature channels, the signal to noise can be improved by square root of 2 [18]. Rapid scan spectra yield the same information as a CW spectrum but has increased signal to noise for the same acquisition time [24-26].

Rapid Scan Imaging

Linear magnetic field gradients are used to encode spatial information in spectral data [27]. The effect of applying a linear gradient can be thought of as viewing an object from an angle in a spectral-spatial plane. Data are collected as a function of the spectral angle, α. The gradient strength is stepped and a projection is collected at each gradient value. The additional magnetic field due to the gradient is felt by the sample and the relative field becomes equation 1.3, where r is the spatial location of the sample in three dimensions.

$$\Delta B = G * r \qquad \text{eq. 1.3}$$

Using an inverse Radon transformation, the spatial information can be reconstructed from the projections [28]. Filtered-back projection (FBP) algorithms are most commonly used to reconstruct images up to four dimensions, with the fourth dimension being the spectral dimension. In FBP, the magnetic field gradient strength is related to the spectral and spatial dimensions of the object as well as the spectral angle by equation 1.4.

$$G = \frac{\Delta B}{\Delta L} \tan(\alpha) \qquad \text{eq. 1.4}$$

where ΔB and ΔL are the spectral and spatial dimensions of the object, respectively. In general, the spatial resolution of an image is determined by the minimum spectral linewidth, the maximum gradient, and the number of projections that are collected. For a constant spectral linewidth, the resolution of an image is improved by increasing the maximum gradient or the number of projections.

Data are collected for α from -90° to 90°, with ±90° being practically impossible to achieve because it would require an infinitely large gradient. The majority of spectral information is from small projection angles while spatial information is greatest at large angles. The signal to noise inherently decreases as the gradient strength increases. However, in rapid scan data, the absorption spectra signal to noise falls off linearly with increasing gradient strength. First derivative CW data signal to noise falls off quadratically with increasing gradient strength, thus, making rapid scan a higher signal to noise imaging technique compared to CW [29].

The focus of this dissertation is on EPR method and instrument development at low frequency. Chapter 2 outlines a magnetic field reversal method that reduces background signals in rapid scan spectra. Chapter 3 characterizes a new 700 MHz to 1 GHz EPR spectrometer and demonstrates imaging capabilities with rapid scan. Chapter 4 covers work on developing new methods to measure T_1 using rapid scan EPR and frequency or field stepped EPR. Chapter 5 describes a new exponential sine shaped pulse implemented at 1.5 GHz.

Chapter 2: Background Reduction in Rapid Scan EPR Spectroscopy

2.1 Introduction

One key difference between rapid scan (RS) and continuous wave (CW) EPR is the way the spectra are detected. In CW, the detection is phase sensitive relative to the phase of the modulation frequency and detected at a single frequency – the modulation frequency. This detects the slope of the absorption spectrum and throws away high frequency noise and low frequency background signals that contribute to baseline problems. In rapid scan, the spectra are directly detected using a bandwidth of a few MHz. This allows for a wide range of frequencies that includes both crucial data as well as noise and unwanted background signals. Low frequency background signals that oscillate at the rapid scan frequency (kHz range) or its harmonics are a challenge for rapid scan EPR due to the overlap of frequencies between the EPR and background signals. The background signals are caused by mechanical vibrations from the interaction of the main magnetic field, B_0, and the rapidly changing magnetic field produced by current in the rapid scan coils, the motor-effect. This type of background is decreased by providing a more rigid and shock absorbing material, Sorbethane^{TM}, to encase the scan coils. The rapid scan coils are located near the resonator which contains conducting material. The rapidly changing current also produces eddy currents in the resonator which contribute to the detected background signals.

Rapid scan background is often many times larger than the signal of interest. It is sometimes hard to separate broad, weak signals from the background. One way to remove background is to do an off-resonance subtraction. The off-resonance spectrum should contain only background and no EPR signal. This type of background removal works best at higher fields, e.g. X-band (~9.5 GHz), where the off-resonance step is a small percentage of the total field. However, the background shape, amplitude, and phase have been observed to depend on the magnetic field value. This makes collecting background off-resonance that is identical to background on-resonance problematic. At VHF (very high frequency, includes 250 MHz), the field is only 90 G and rapid scan sweeps of 75 G are routinely used to capture a three-line nitroxide spectrum. With these parameters, off-resonance subtraction is not practical. Also, at low frequency signal intensity decreases relative to higher frequencies [30] making separation of signal from background more difficult at low frequency relative to higher frequencies.

It has also been shown that background signals can be removed using post processing methods. A paper published in 2009 outlines a post-processing procedure in which the rapid scan background signals are assumed to be first and second harmonics of the scan frequency and subtracts these frequencies in the Fourier domain [31]. The procedure works well for pure sinusoidal background but makes assumptions about the background which are not always true. Furthermore, if the background is not sinusoidal at all, the procedure can actually introduce background rather than remove it.

The new background removal data acquisition method that will be described makes no assumptions about the shape, amplitude, or phase of the background and theoretically can be done at any EPR frequency. Implementation of this method at VHF is described in [32].

2.2 Method Description

In this new method, two on-resonance scans denoted scan 1 and scan 2 are separately collected. The two scans differ from each other in two ways. The first difference is the polarity of the magnetic field, B_0. The second is the phase of the rapid scan field relative to the data acquisition trigger.

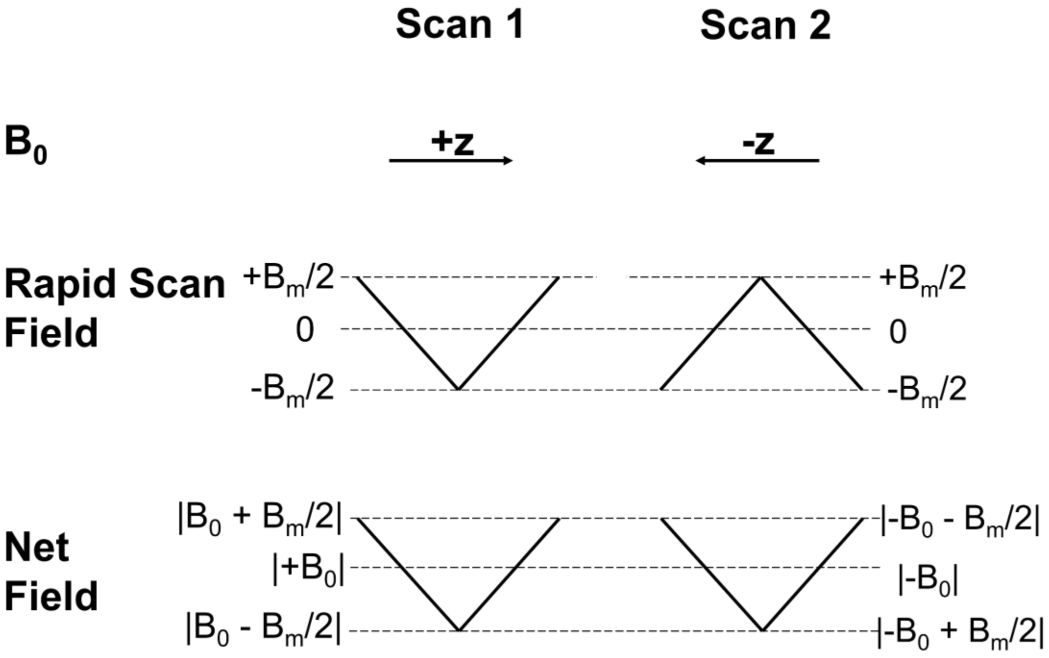

Figure 2.1: Schematic of background reduction method procedure. In scan 1 the magnetic field, B_0, is in the positive Z direction. The rapid scan field is modulated from $+B_m/2$ to $-B_m/2$ making the first half cycle a down-field scan. In scan 2 the magnetic field, B_0, is in the negative Z direction. The rapid scan field is modulated from $-B_m/2$ to $+B_m/2$ making the first half cycle an up-field scan. The magnitude of the net field in scan 1 and scan 2 is the same. Figure is reproduced with permission from Ref. 32.

In rapid scan EPR, the scans are typically either sinusoidal or triangular shaped and modulated from $+B_m/2$ to $-B_m/2$ centered around B_0. Thus, the direction of the scan can be thought of as “up” in which the field is scanned from low field to high field or “down” in which the field is scanned from high field to low field. Using this new method, the data acquisition trigger in scan 2 is offset by 180° relative to scan 1. This shift interchanges “up” and “down” scans relative to the start of data acquisition. Since the direction of both the rapid scan field and B_0 field are changed, the magnitude of the net field for both scans is the same. A schematic of each scan and the resulting net field is shown in Figure 2.1.

The net result of changing both the polarity of B_0 and the relative position of the acquisition trigger in scan 2 is that the signal is inverted and the background is not inverted relative to scan 1. This allows for scan 2 to be subtracted from scan 1. The result is a cancellation of the background and an increase in signal. The signal to noise increases by a factor of $\sqrt{2}$ since there are twice as many averages in the combined scan 1 - scan 2 compared to scan 1. Because of this increase in signal to noise, the number of averages for a single scan can be decreased, so that the total collection time for the B_0 reversal method remains the same as for a single scan in which the method is not used.

From the perspective of the spins, the inversion of the signal in scan 2 relative to scan 1 is a result of the mechanical structure of the cross-loop resonator (CLR) used in the experiment. In a CLR, the detection resonator is physically oriented 90° away from the excitation resonator and thus from B_1. The voltage induced in the detection resonator is always 90° out of phase with B_1. When B_0 is reversed the direction that the spins are rotating is changed by 180°. In one B_0 direction the phase of the EPR signal is +90° relative to B_1 and in the other it is -90° relative to B_1. The net result is that the EPR signal phase is inverted by 180° in scan 2 relative to scan 1. A CLR is a key component that is required for this method to work. The structure of the CLR does not affect the phase of the background relative to the direction of B_0. From the perspective of the background, the direction of the mechanical vibrations and eddy currents reverse when B_0 is reversed. The 180° shift of the data acquisition trigger in scan 2 relative to scan 1 brings the polarity of the background signal in scan 2 back into phase with scan 1. The net result is that the EPR signal inverts and the background does not, permitting subtraction of scan 2 from scan 1. The subtraction of scan 2 from scan 1 can be performed before or after the deconvolution procedure and produces the same spectrum.

The setting time of the main magnetic field, B_0, is about 1.3 s. Therefore, scan 1 and scan 2 are collected separately, in blocks of averages, as opposed to flipping the magnetic field after each acquisition trigger. For imaging experiments, scan 1 and scan 2 are acquired at each gradient before stepping to the next gradient.

2.3 VHF Experimental

A 16 mm CLR described in [33] was used for experiments at 259 MHz, which is in the band called VHF. It was fitted with rapid scan coils that have a coil constant of 27 G/A. The rapid scan field was driven by the coil driver (RSCD) described in [34]. The amplitude and harmonic composition of the background are scan frequency dependent. Frequencies were scanned using a chirp pulse generated by the RSCD from about 1.2 kHz to 7.5 kHz to map out the scan frequency dependent amplitude of the background caused by mechanical resonances. The chirp scan result is shown in Figure 2.2. Relatively low background amplitudes are observed at scan frequencies between 2 and 3 kHz and also above 5 kHz. Data collected at 259 MHz used scan frequencies from 2-3 kHz and around 10 kHz.

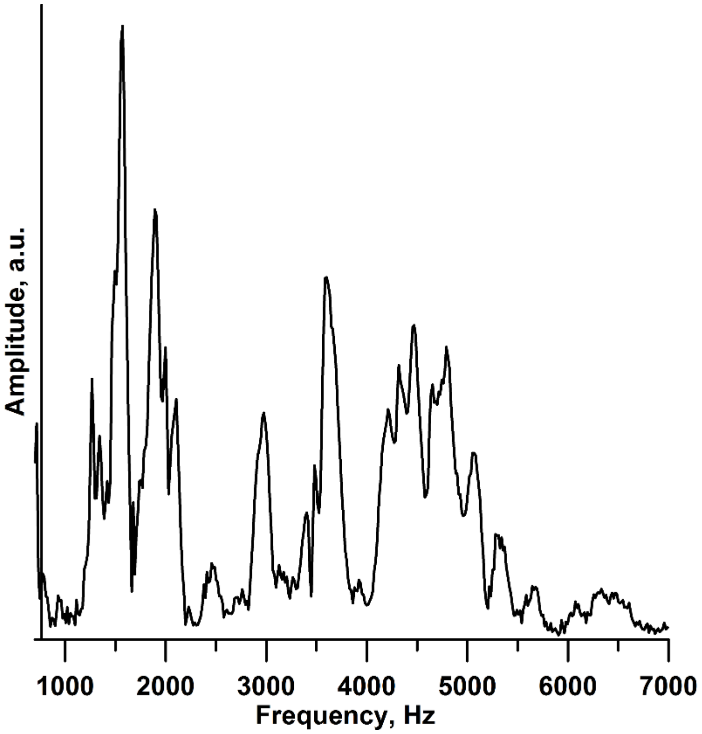

Figure 2.2: Background profile of the 16 mm empty VHF CLR operating at 259 MHz. A chirp of scan frequencies from about 1.2 kHz to 7.5 kHz was obtained with a sinusoidal sweep of approximately 17 G. The black trace is an averaged scan with a total acquisition time of 2.24 min. Incident power on the CLR was 316 mW. B_0 = 93.8 G. Figure is reproduced with permission from Ref. 32.

A 25 mm CLR was used for imaging experiments at 254 MHz [35]. The resonator was fitted with rapid scan coils that have a coil constant of about 18.8 G/A. A chirp of the scan frequencies (Figure 2.3) showed regions of low amplitude above 3 kHz. Imaging experiments were performed at 2.213 kHz.

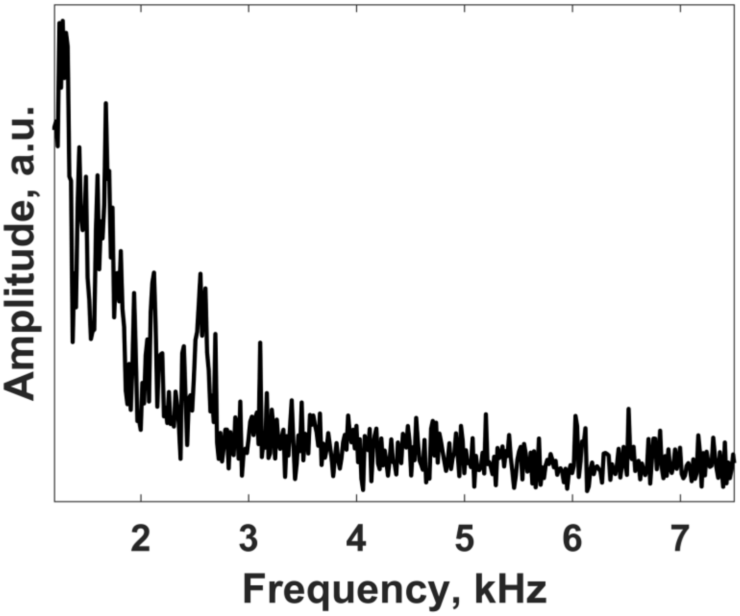

Figure 2.3: Background profile of the 25 mm empty VHF CLR operating at 254 MHz. A chirp of scan frequencies from about 1.2 to 7.5 kHz was obtained with a sinusoidal sweep of approximately 13.7 G. The black trace is an averaged scan with a total acquisition time of 2.2 min. The incident power on the CLR was 65 mW. B_0 = 91 G.

All experiments performed at VHF used the spectrometer described in [36]. The air-core magnet is powered by recently purchased bipolar power supplies manufactured by CAEN Technologies. A CAENels FAST-PS-1K5 30-5 controls the main magnetic field and a CAENels FAST-PS 2040-600 supply controls the Z-gradient field. Remote commands were sent to the power supplies over ethernet and to the RSCD over RS-232 using locally written python code. The python code synchronized the changing magnetic fields with the Bruker data acquisition software to facilitate automatic data collection.

Samples

Tempone and CTPO were purchased from Sigma-Aldrich. Trityl-CD_3 and OX63 were obtained from GE Healthcare via Howard J. Halpern, University of Chicago. A 0.1 mM OX63 (tris-(8-carboxyl-2,2,6,6-tetrakis(2-hydroxyethyl)-1,3,5,7-tetrathia-2,6-dihydro-s-indacene-4-yl) methyl sodium salt), solution was prepared in 2 mM HEPES (4-(2-hydroxyethyl)-1-piperazine-ethanesulfonic acid) buffer. Aqueous solutions of 0.2 mM OX63, 0.2 mM trityl-CD_3 (methyltris(8-carboxy-2,2,6,6-tetramethyl(d3)-benzo[1,2-d:4,5-d0]bis(1,3)dithiol-4-yl)-tri sodium salt), 0.1 mM CTPO (3-carbamoyl-2,2,5,5-tetramethyl-3-pyrroline-1-yloxy), 1 mM Tempol (4-hydroxy-2,2,6,6-tetramethylpiperidin-1-oxyl), 0.5 mM Tempone, and 1 mM ^{15}N per-deuterated Tempone (PDT, Cambridge Isotope Laboratories, Tewksbury, MA) solutions also were prepared. The aqueous trityl-CD_3, Tempol, PDT, and 0.1 mM OX63 solutions were bubbled with N_2 and flame sealed to prevent oxygen from interacting with the sample. The CTPO, Tempone and 0.2 mM OX63 samples were air saturated. Two lithium phthalocyanine (LiPc) samples (1.1 mm ID x 3 mm long) were flame sealed after being evacuated on a high vacuum line. Data were acquired at microwave powers that did not saturate the EPR signal.

2.4 VHF Results

Figure 2.4 shows rapid scan data acquired with a triangular scan for a 0.5 mM Tempone sample. The scan frequency was 2 kHz and the sweep width was 50.8 G. Figure 2.4A shows scan 1 and Figure 2.4B shows scan 2. Figure 2.4C shows scan 1 – scan 2. In each panel, the blue and orange traces represent the in-phase (I) and quadrature (Q) channels, respectively. The signal was phased to show all absorption in the I channel and all dispersion in the Q channel, but that is not necessary. Rapid scan data are collected in the time domain (top axis), but for triangular scans this can be converted to the field domain (bottom axis) without deconvolution when wiggles are not present. In Figure 2.4C, the background was successfully removed.

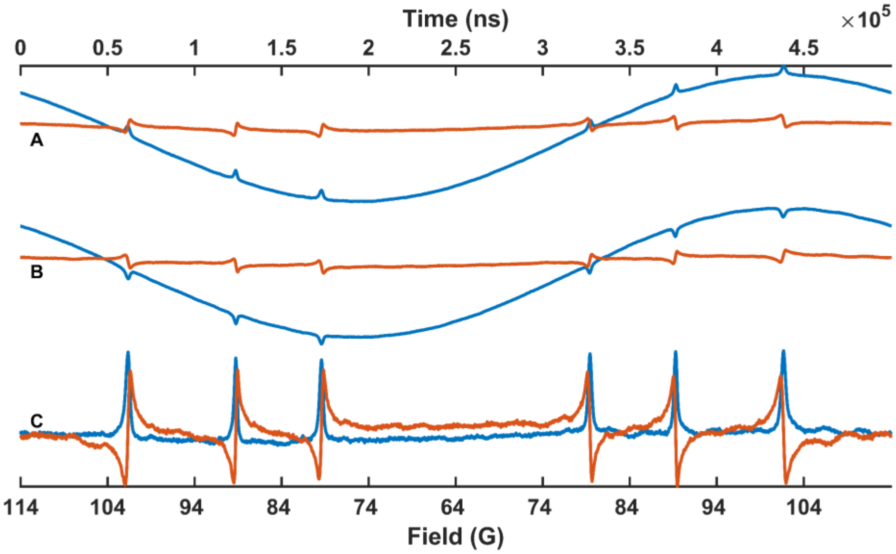

Figure 2.4: Triangular scans of 0.5 mM Tempone at 259 MHz. Blue and orange traces are absorption and dispersion EPR signal, respectively. (A) scan 1 (B) scan 2 (C) scan 1 - scan 2. Figure is reproduced with permission from Ref. 32.

Although background signals in rapid scan are typically the first harmonic of the scan frequency, occasionally higher harmonics are present. The B_0 reversal background removal procedure also removes the second harmonic. Figure 2.5 shows a single averaged cycle of rapid scan data acquired with a sinusoidal scan at 10.243 kHz and sweep width of 42 G. The background shown in Figure 2.5A and B clearly has second harmonic contributions. The subtraction of scan 2 from scan 1 (Figure 2.5C) shows that the background has been removed. Sinusoidal scans require deconvolution to produce a spectrum with a field axis, which is done in post-processing.

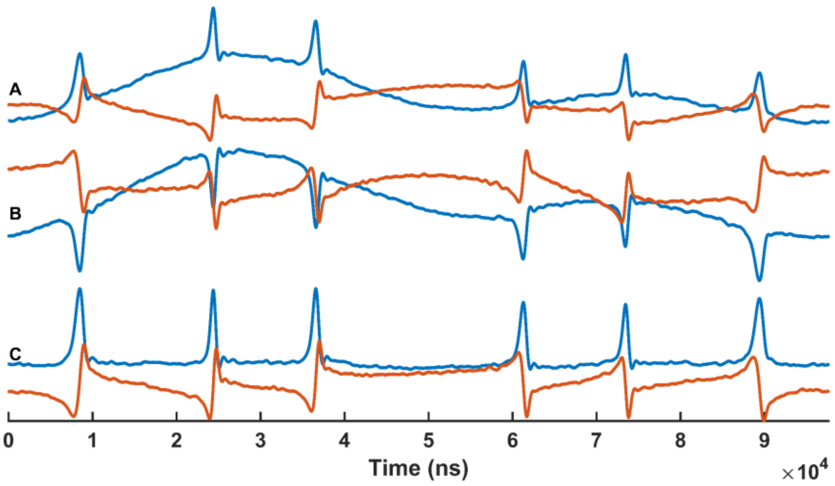

Figure 2.5: Sinusoidal scans of 0.5 mM Tempone at 259 MHz. Blue and orange traces are absorption and dispersion EPR signal, respectively. (A) scan 1 (B) scan 2 (C) scan 1 - scan 2. Figure is reproduced with permission from Ref. 32.

Sinusoidal rapid scans of 0.1 mM CTPO are shown in Figure 2.6 before and after sinusoidal deconvolution. The deconvolution routine included the post-processing background removal procedure described in [31]. The spectrum was obtained with a rapid scan frequency of 10.242 kHz and a 40 G scan width. For this data set, the best result was obtained by first subtracting scan 2 from scan 1 and then performing deconvolution which included the post-processing background removal procedure. The deconvolved spectrum in Figure 2.6D has a flatter baseline than the deconvolved spectrum in Figure 2.6B.

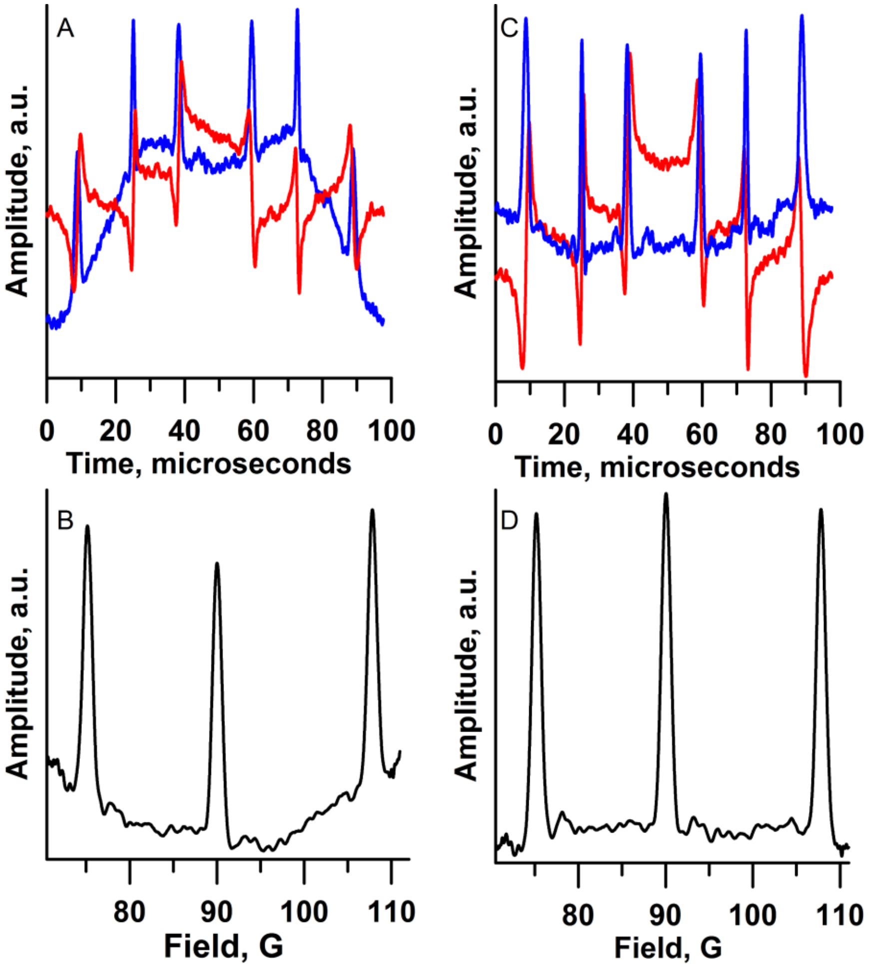

Figure 2.6: Sinusoidal scans of 0.1 mM CTPO 259 MHz. (A) Averaged full cycle of scan 1. (B) Deconvolved spectrum corresponding to A. (C) Averaged full cycle of scan 1 – scan 2. (D) Deconvolved spectrum corresponding to part C. Figure is reproduced with permission from Ref. 32.

To demonstrate this technique for a spectrum containing a narrow line, triangular rapid scan data were acquired for a 0.2 mM trityl-CD_3 sample at 259 MHz, shown in Figure 2.7. The scan frequency was 2 kHz and the sweep width was 18.5 G. The data were deconvolved using a locally-written linear deconvolution Matlab routine that does not use a post-processing background removal procedure. After deconvolution and without the B_0 reversal procedure, the deconvolved spectrum contains a linearly sloping baseline (Figure

2.7B). The B_0 reversal procedure removes the rapid scan background prior to linear deconvolution (Figure 2.7C) resulting in a deconvolved spectrum with a flat baseline (Figure 2.7D) and does not distort the line shape of the narrow signal.

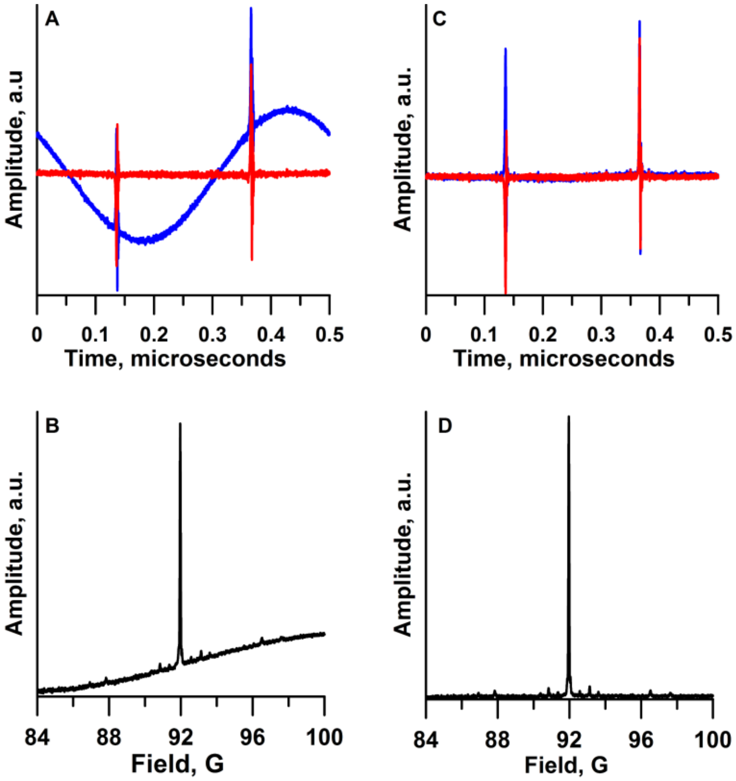

Figure 2.7: Triangular rapid scans of 0.2 mM trityl-CD_3 at 259 MHz. (A) Averaged full cycle of scan 1. (B) Deconvolved spectrum corresponding to A. (C) Averaged full cycle of scan 1 – scan 2. (D) Deconvolved spectrum corresponding to part C. Note the ^{13}C hyperfine lines are visible in parts B and D. Figure is reproduced with permission from Ref. 32.

To extend this technique to EPR imaging, the relationship between B_0 and gradient must also be considered. The direction of the gradient must be reversed along with B_0 to maintain the same absolute magnitude of B_0 at the location of the imaged sample. This is schematically depicted in Figure 2.8. In the absence of a gradient, the magnetic field strength at a spatial location is B_0. Application of a gradient adds or subtracts from the magnetic field, B_0, depending upon the polarity of the gradient. For example, when B_0 is positive and a positive gradient is applied, the EPR signal spatially encodes the position of the sample by appearing to move up the B_0 axis by an amount equal to the gradient strength times the distance from the center of the resonator to the sample. When B_0 is reversed, the direction of the gradient must also be reversed to maintain an absolute field magnitude at the sample location.

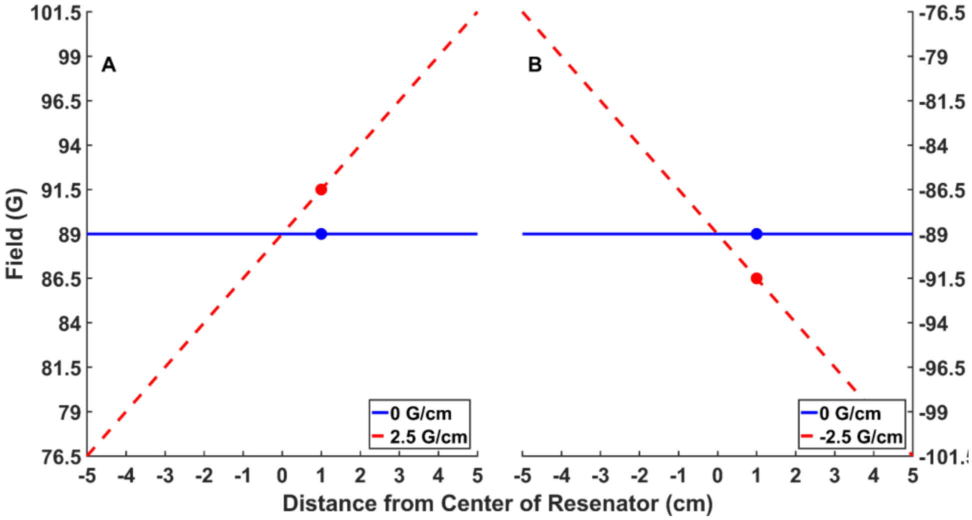

Figure 2.8: Schematic of gradient reversal. The net magnetic field as a function of space is shown before (blue) and after (red) application of a gradient. Dots represent net magnetic field strength at +1 cm. (A) scan 1 with a positive B_0 and positive gradient strength. (B) scan 2 with a negative B_0 and negative gradient strength. Figure is reproduced with permission from Ref. 32.

Since the application of a gradient changes the net magnetic field at the sample, the background signal amplitude changes as a function of gradient strength. Gradient fields also broaden spatially extended samples, which decreases the signal to noise at high gradient field strengths. Triangular rapid scan data were acquired in the presence of a 10 G/cm gradient for a 0.1 mM CTPO sample to demonstrate the power of the B_0 reversal method. Without the B_0 reversal method the CTPO signal is indistinguishable from the rapid scan background signal (Figure 2.9A). After subtraction of scan 2 from scan 1 (Figure 2.9B), the signal is detectable. The residual background may be a result of imperfect resonator position within the gradient field.

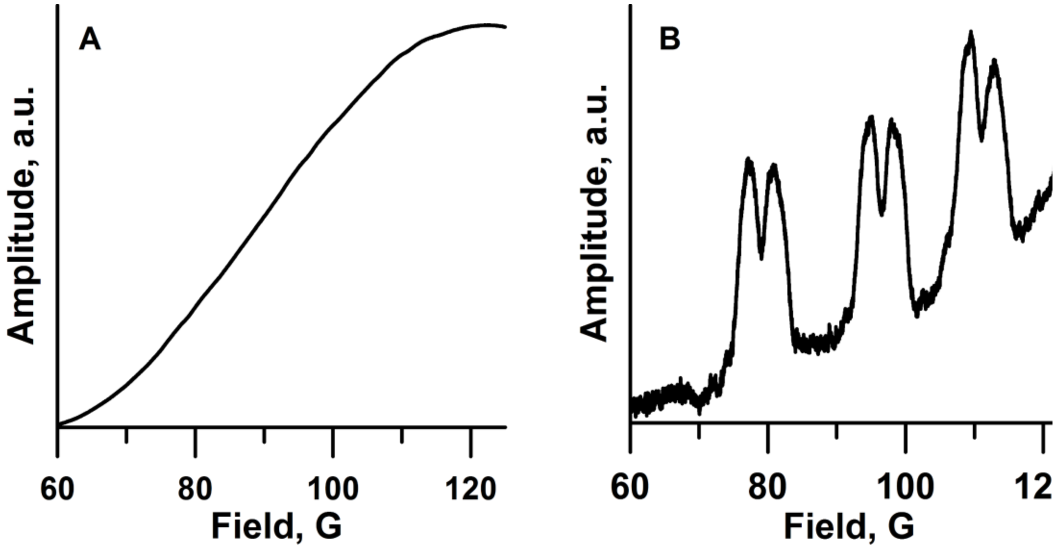

Figure 2.9: Triangular rapid scans of 0.1 mM CTPO in the presence of a 10 G/cm Z gradient at 259 MHz. (A) scan 1. (B) scan 1 – scan 2. Figure is reproduced with permission from Ref. 32.

VHF Imaging

Rapid scan images were collected at VHF using a 25 mm VHF CLR operating at 254 MHz. Two imaging phantoms were constructed for imaging. One phantom consisted of two deoxygenated LiPc samples separated by 1 cm (Figure 2.10A). A second imaging phantom was constructed that consisted of one cylinder 25 mm in diameter x 16 mm long filled with 0.1 mM OX63 and two half cylinders 25 mm in diameter x 16 mm long containing 1mM ^{14}N Tempol and 1 mM ^{15}N PDT, respectively (Figure 2.10C).

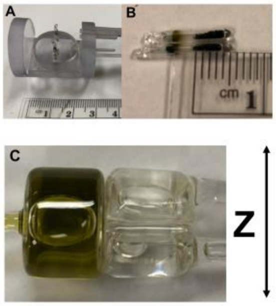

Figure 2.10: Imaging phantoms. (A, B) Two LiPc samples. (C) Aqueous phantom consisting of 0.1 mM OX63, 1 mM Tempol, and ^{15}N PDT. Figure adapted from Ref. 35.

The B_0 reversal method was incorporated into image data acquisition via a locally written python program. Sinusoidal scans of the phantom shown in Figure 2.10A at 0 G/cm and at -5 G/cm are shown in Figure 2.11. Due to the narrow linewidth of LiPc, large gradient values are not needed to distinguish the two LiPc signals when they are spatially separated by 1 cm. Thus, 5 G/cm was a reasonable maximum gradient value to use. The B_0 reversal method cleanly removed the background at all gradient strengths from -5 G/cm to +5 G/cm.

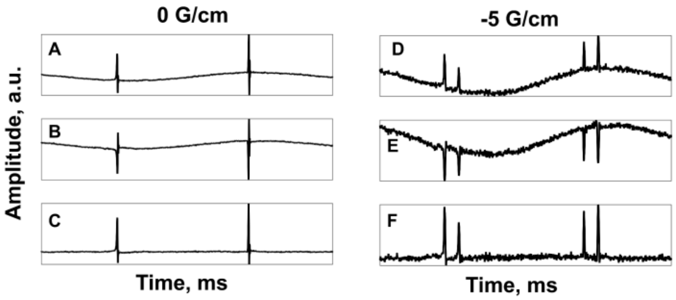

Figure 2.11: Sinusoidal rapid scans of two LiPc samples at 254 MHz. B_0 = 91.35 G, scan frequency = 2.213 kHz, sweep width = 30 G, incident power = 3.2 mW. (A, D) scan 1 (B, E) scan 2 (C, F) scan 1 – scan 2 in the absence or presence of a magnetic field gradient.

A 2-dimensional spectral-spatial image was collected of the LiPc phantom along the X axis. Image reconstruction did not use any other background removal procedure except for the B_0 reversal method. The reconstructed images do not show significant differences between scan 1 only (Figure 2.12A) versus scan 1 – scan 2 (Figure 2.12B), indicating, that for this sample and set of conditions, the reconstruction program is insensitive to the sloping baseline of deconvolved projections. LiPc is a spectrally sharp signal that stands out well against low frequency background.

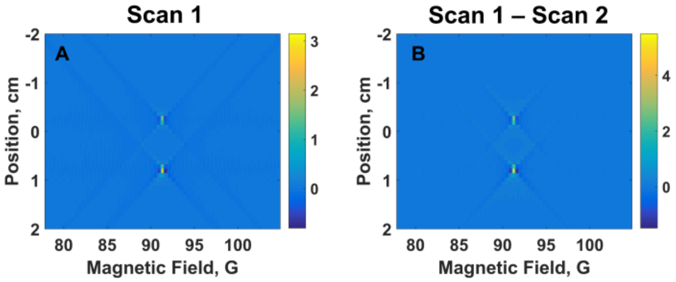

Figure 2.12: Reconstructed 2D spectral-spatial images of two LiPc samples separated by 1 cm at 254 MHz. B_0 = 91.35 G, Z-gradient = +/- 5 G/cm, 201 projections, scan frequency = 2.213 kHz, sweep width = 30 G, incident power = 3.2 mW, spatial resolution = 1 mm. (A) Reconstruction of scan 1 only. (B) Reconstruction of scan 1 – scan 2. Data is published in [35].

Sinusoidal scans of the aqueous phantom shown in Figure 2.10C at 0 G/cm and -10 G/cm are shown in Figure 2.13. The B_0 reversal method reduced the background at most gradient strengths but did not eliminate the background completely as it did for the LiPc phantom. The residual background is likely due to an impurity signal in the Pyrex tubing located at approximately 45 G. The sweep width used for data collection was 75 G centered around 91.42 G which extended into the Pyrex signal.

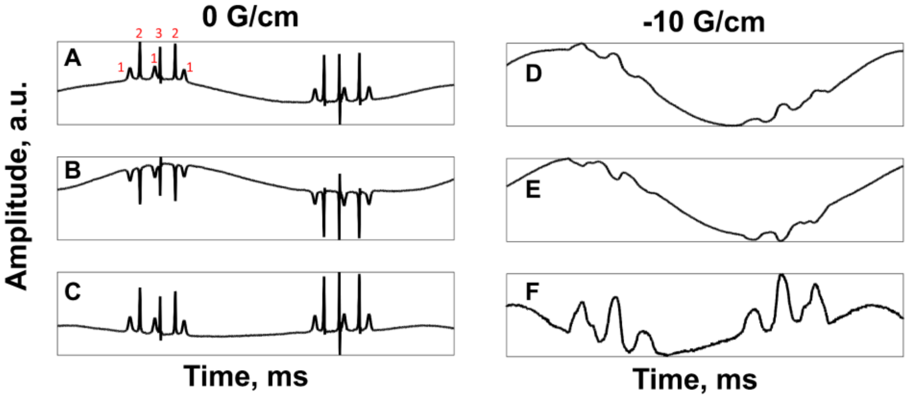

Figure 2.13: Sinusoidal rapid scans of aqueous phantom (Figure 2.10C) containing 0.1 mM OX63 (signal 3), 1 mM ^{14}N Tempol (signal 1), and ^{15}N PDT (signal 2) at 254 MHz. B_0 = 91.42 G, scan frequency = 2.213 kHz, sweep width = 75 G, incident power = 26 mW. (A, D) scan 1 (B, E) scan 2 (C, F) scan 1 – scan 2, in the absence or presence of a magnetic field gradient.

A 2-dimensional spectral-spatial image of this phantom was collected by varying the gradient along Z from – 10 G/cm to +10 G/cm. Images reconstructed from scan 1 (Figure 2.14A) and scan 1 – scan 2 (Figure 2.14B) are almost identical, indicating again that the image reconstruction software is insensitive to low frequency background signals when the signal is easily discernable from the background signal. Image reconstruction did not use any other background removal procedure except for the B_0 reversal method.

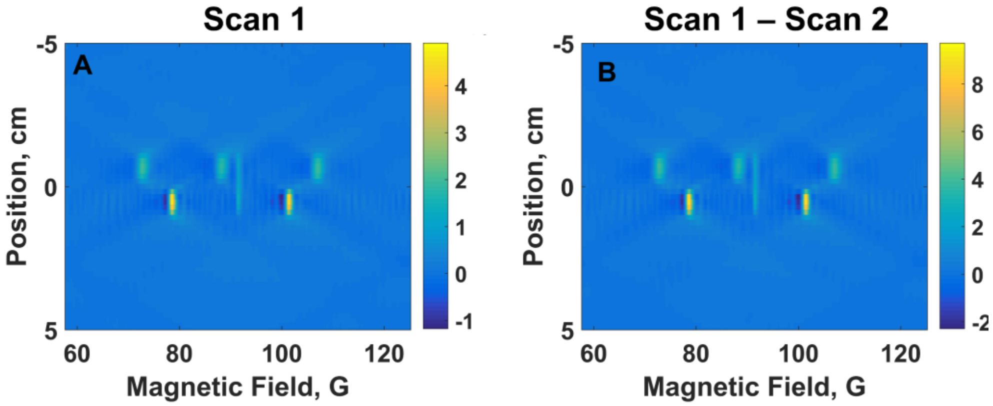

Figure 2.14: Reconstructed 2D spectral-spatial images of aqueous phantom (Figure 2.10C) containing 0.1 mM OX63, 1 mM ^{14}N Tempol and ^{15}N PDT at 254 MHz. B_0 = 91.42 G, Z-gradient = +/- 10 G/cm, 201 projections, scan frequency = 2.213 kHz, sweep width = 75 G, incident power = 26 mW, spatial resolution = 2 mm. (A) Reconstruction from scan 1 only. (B) Reconstruction from scan 1 – scan 2. Data is published in [35].

2.5 UHF Experimental

The B_0 reversal method was also tested at 700 MHz which is within the band called UHF (ultra-high frequency). The spectrometer used is described in [37] and also uses CAEN Technologies power supplies to control the main magnetic field and gradient field. The same python programs that were employed at VHF were transferred to the 700 MHz spectrometer. The resonator is a 25 mm diameter CLR consisting of two saddle coils (Figure 3.4, p.58). The rapid scan coils surrounding the CLR have a coil constant of about 15.6 G/A. A chirp of scan frequencies between 1.2 and 7.5 kHz generated by the RSCD showed scan frequencies above 2 kHz were in regions with relatively low amplitude (Figure 2.15). The B_0 reversal method was tested at 3.1 kHz.

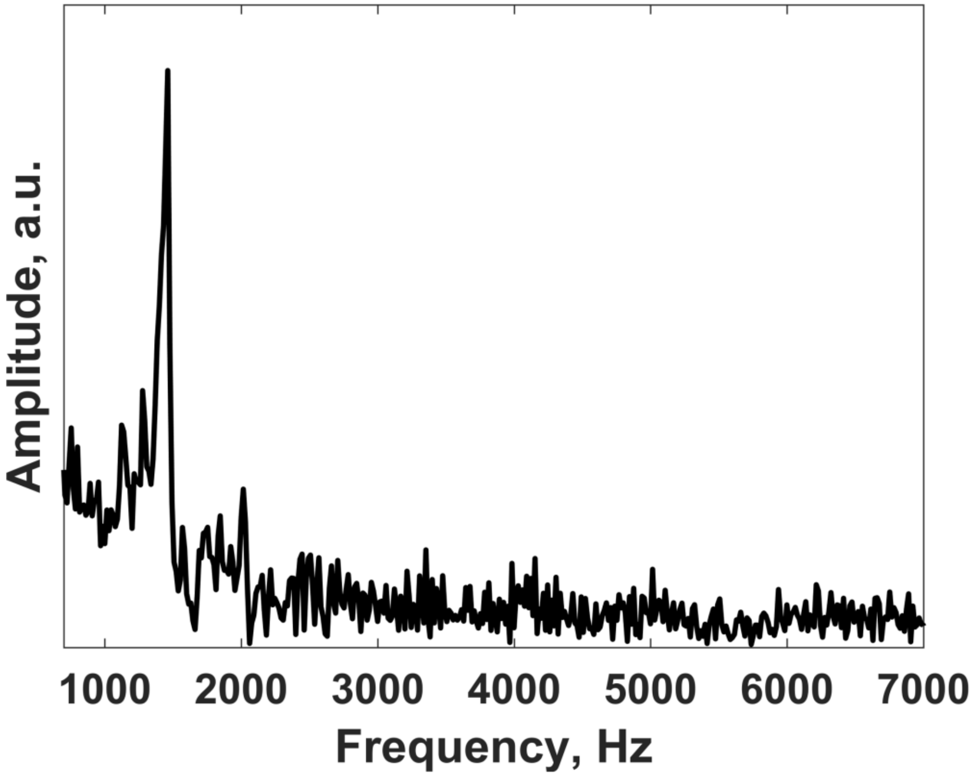

Figure 2.15: Background profile of the 25 mm 700 MHz CLR containing an aqueous sample. A chirp of scan frequencies from about 1.2 kHz to 7.5 kHz was obtained with a sinusoidal sweep of approximately 25.6 G. The black trace is an averaged scan with a total data acquisition time of approximately 2.2 min. The incident power on the CLR was approximately 20 mW. B_0 = 252.8 G.

2.6 UHF Results

Figure 2.16 shows sinusoidal rapid scan data acquired for a phantom containing 0.1 mM OX63, 1 mM ^{14}N Tempol, and 1 mM ^{15}N PDT (Figure 2.10C). Subtracting scan 2 from scan 1 reduced the background amplitude by about 20% but did not completely eliminate it (Figure 2.16C). Two additional scans, denoted scan A and scan B were collected. These new A and B scans were collected at B_0 = 0 G with the same rapid scan polarities as scan 1 and scan 2, respectively. The background signal was completely removed by subtracting the corresponding 0 G scans from scan 1 and scan 2 before subtracting scan 2 from scan 1 (Figure 2.16D). This indicates that there is a component of the background signal that does not depend entirely on $B_{0,}$ as it did at VHF. It is hypothesized that the non-field dependent background is caused by the eddy currents in the resonator that are coupled into the detection system.

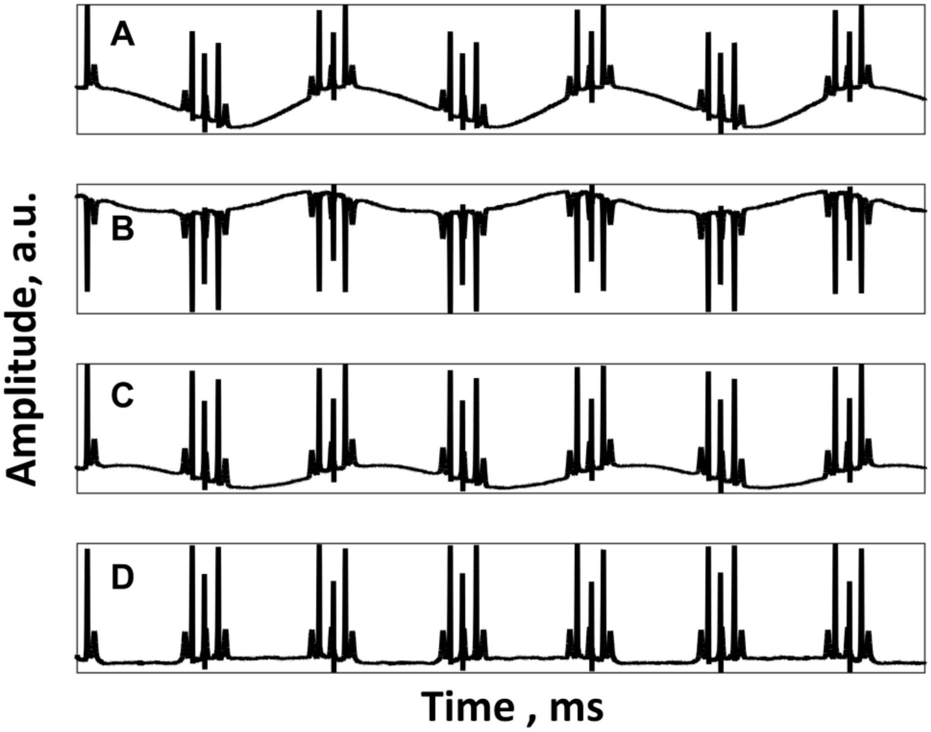

Figure 2.16: Sinusoidal rapid scans of phantom (Figure 2.10C) containing 0.1 mM OX63, 1 mM ^{14}N Tempol, and 1 mM ^{15}N PDT at 708 MHz. Only the absorption channel is shown for simplicity. B_0 = 252.8 G, scan frequency = 3.133 kHz, sweep width = 75 G, incident power = 20 mW. (A) scan 1 (B) scan 2 (C) scan 1 - scan 2 (D) (scan 1 – scan A) – (scan 2 – scan B).

Figure 2.17 shows sinusoidal scan data for the phantom containing 0.1 mM OX63, 1 mM ^{14}N Tempol, and 1 mM ^{15}N PDT (Figure 2.10C) with the addition of a 10 G/cm gradient along the Z axis. The B_0 reversal method (scan 1 – scan 2) reduced the background by about 70 % (Figure 2.17C). Additional scans at 0 G at each rapid scan polarity (scan A and scan B) were required for subtraction to remove the background entirely (Figure 2.17D). Interestingly, when the gradient strength was varied, it was necessary to collect a 0 G spectrum at each gradient value in addition to scan 1 and scan 2 to remove the background. This implies that there is an interaction between the gradient strength and the

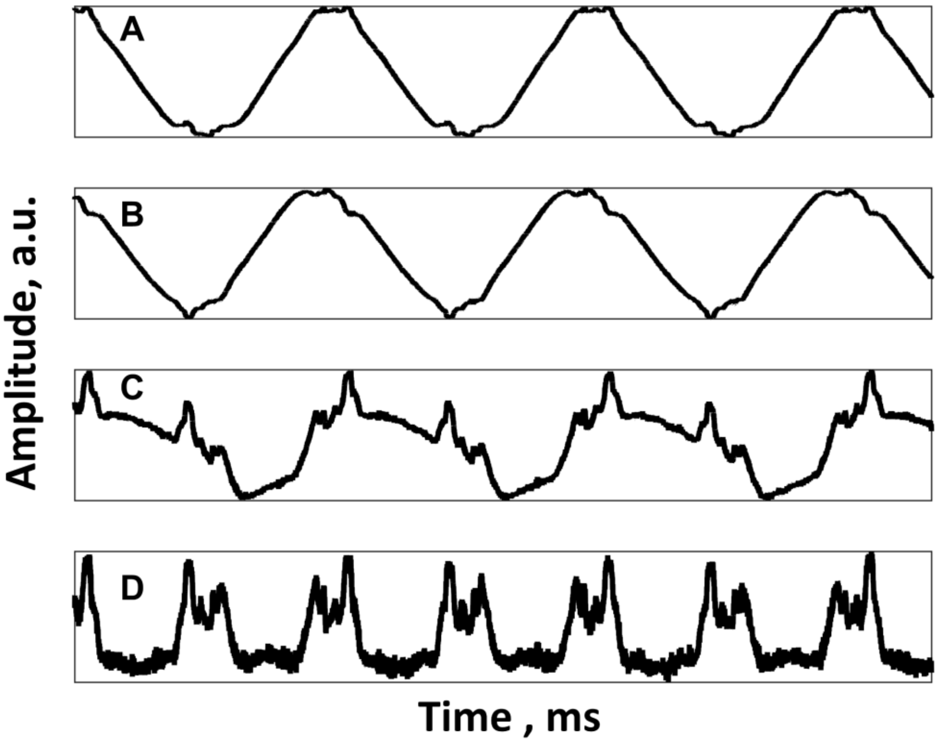

Figure 2.17: Sinusoidal rapid scans of phantom containing 0.1 mM OX63, 1 mM ^{14}N Tempol, and 1 mM ^{15}N PDT with a 10 G/cm gradient applied at 708 MHz. Only the absorption channel is shown for simplicity. B_0 = 252.8 G, scan frequency = 3.133 kHz, sweep width = 75 G, incident power = 20 mW. (A) scan 1 (B) scan 2 (C) scan 1 - scan 2 (D) (scan 1 – scan A) – (scan 2 – scan B).

eddy currents in the resonator caused by the rapid scan field, independent of B_0. Although these observations are not completely understood at this point, it is hypothesized that the differing mechanical structures of the two resonators (one at VHF and one at UHF) causes the different relative contributions of field-dependent and field-independent background at the two RF frequencies.

To investigate the dependence of background on B_0 and Z-gradient field strength, background signals were collected in the empty ~700 MHz resonator as a function of either B_0 (Figure 2.18) or gradient strength (Figure 2.19). The background amplitude was measured once as a peak-to-peak height for both the rapid scan channels. For the original B_0 reversal method to work as expected, these data sets should be symmetric around 0 G, but they are clearly not. The background changes as a function of both B_0 and Z-gradient field strength, but the pattern appears somewhat random in Figure 2.18. The plot of background vs. gradient strength shows that the background dependence on gradient field strength is symmetric around 2 G/cm in one channel and has a roughly linear dependence on gradient field strength in the other channel (Figure 2.19). The linear trend appears to depend not just on the gradient strength, but also on the direction of the gradient. This is further evidence that the background in this resonator at UHF is not as easily defined as being solely dependent on B_0 as it was at VHF. To remove background at UHF using the B_0 reversal method, additional scans A and B at 0 G are required for each gradient setting.

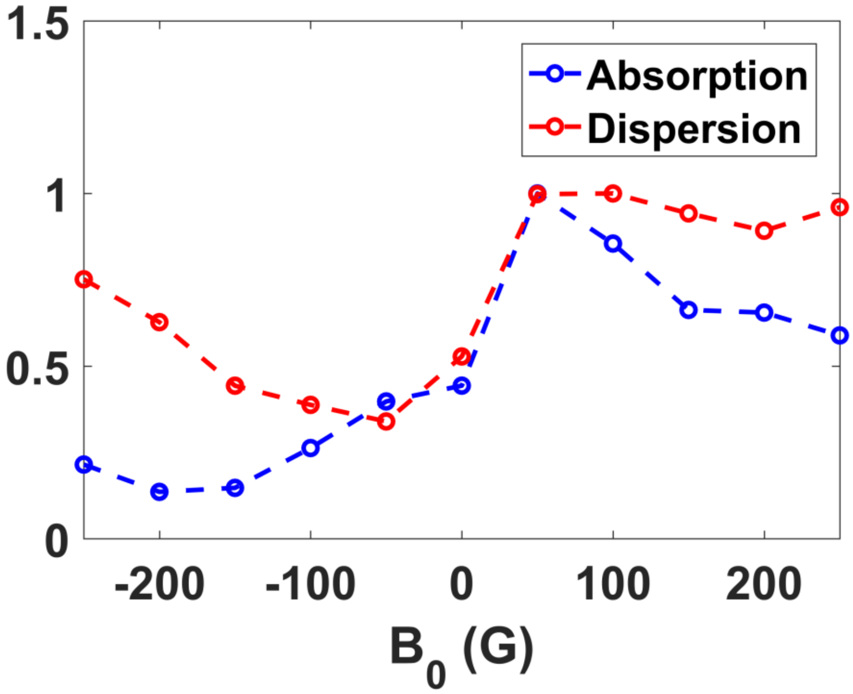

Figure 2.18: Background amplitude for empty 700 MHz resonator as a function of B_0. The blue and red traces represent the two rapid scan detection channels. Incident power = 20 mW, scan frequency = 3.133 kHz, sweep width = 75 G.

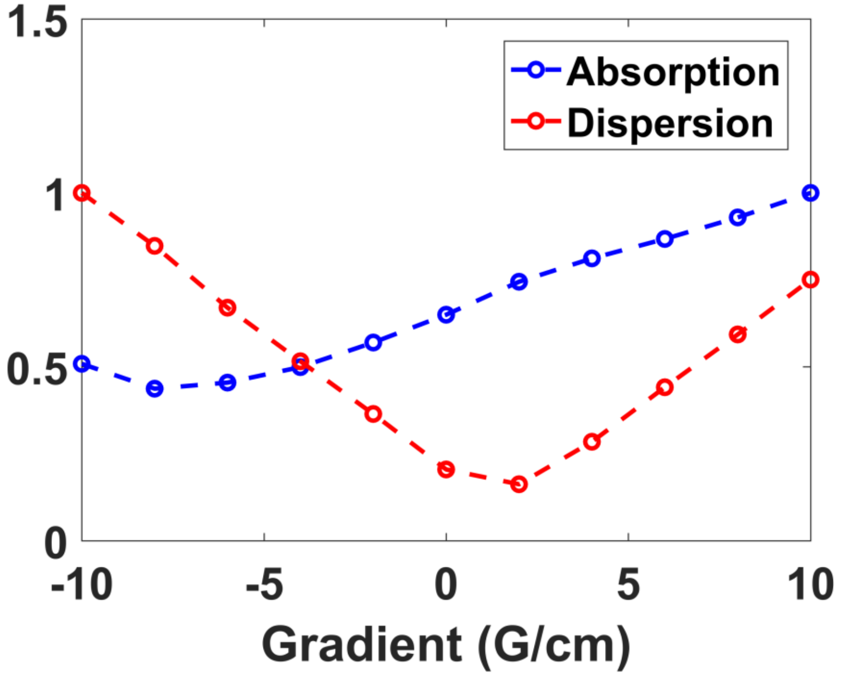

Figure 2.19: Background amplitude for empty 700 MHz resonator as a function of gradient strength. The blue and red traces represent the two rapid scan detection channels. Incident power = 20 mW, scan frequency = 3.133 kHz, sweep width = 75 G, B_0 = 0 G.

UHF Imaging

Two dimensional spectral-spatial images were acquired using sinusoidal scans for the phantom containing 0.1 mM OX63, 1 mM ^{14}N Tempol, and 1 mM ^{15}N PDT (Figure 2.20C) at 700 MHz. The rapid scan background at 3.13 kHz was purely sinusoidal at the first harmonic of the scan frequency. A comparison of Figure 2.20 and 2.21 shows that for this sample and conditions chosen, the B_0 reversal method works as well as a post processing background removal procedure [31]. Figure 2.22A shows that if both procedures are applied, background is introduced rather than removed because the post-processing procedure assumes a sinusoidal background. Also, the image reconstruction software appears to be insensitive to the sloping baseline in Figure 2.22A.

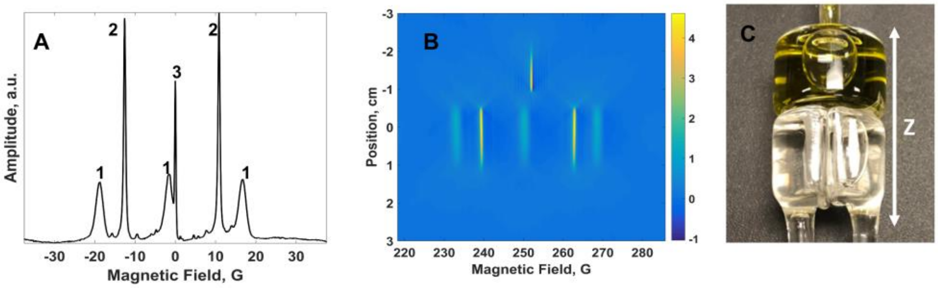

Figure 2.20: 2D spectral-spatial imaging at 708 MHz based on scan 1 only with post-processing background removal routine described in [31] collected at 708 MHz. B_0 =252.8 G, sinusoidal scan frequency = 3.133 kHz, sweep width = 75 G, Z-gradient = +/-10 G/cm, 0.1 G/cm steps, incident power = 20 mW, spatial resolution = 0.5 mm. (A) Zero gradient spectrum. Signal 1 corresponds to 1 mM Tempol, signal 2 corresponds to 1 mM ^{15}N PDT, and signal 3 corresponds to 0.1 mM OX63 (B) Reconstructed image. The Z-gradient distinguishes the OX63 from the nitroxide signals along the Z axis (C) Imaging phantom consists of 0.1 mM OX63 (top), 1 mM Tempol (bottom left) and 1 mM ^{15}N PDT (bottom right).

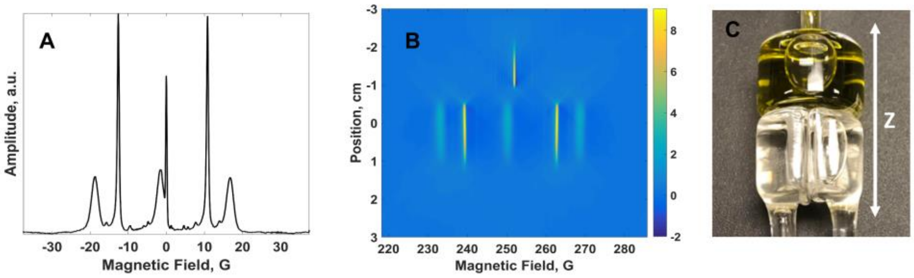

Figure 2.21: 2D spectral-spatial imaging at 708 MHz based on (scan 1- scan A) - (scan 2 - scan B) without the post-processing background removal routine described in [31]. B_0 =252.8 G, sinusoidal scan frequency = 3.133 kHz, sweep width = 75 G, Z-gradient = +/-10 G/cm, 0.1 G/cm steps, incident power = 20 mW, spatial resolution = 0.5 mm. (A) Zero gradient spectrum. (B) Reconstructed image. The Z-gradient distinguishes the OX63 from the nitroxide signals along the Z axis (C) Imaging phantom consists of 0.1 mM OX63 (top), 1 mM Tempol (bottom left) and 1 mM ^{15}N PDT (bottom right).

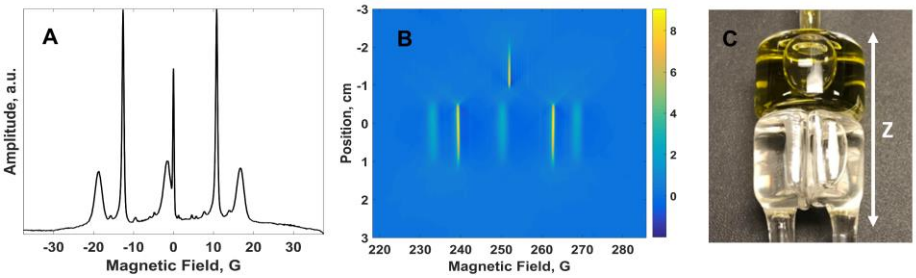

Figure 2.22: 2D spectral-spatial imaging at 708 MHz based on **(**scan 1 - scan A) - (scan 2 - scan B) with the post-processing background removal routine described in [31]. B_0 =252.8 G, sinusoidal scan frequency = 3.133 kHz, sweep width = 75 G, Z-gradient = +/-10 G/cm, 0.1 G/cm steps, incident power = 20 mW, spatial resolution = 0.5 mm. (A) Zero gradient spectrum. (B) Reconstructed image. The Z-gradient distinguishes the OX63 from the nitroxide signals along the Z axis. (C) Imaging phantom consists of 0.1 mM OX63 (top), 1 mM Tempol (bottom left) and 1 mM ^{15}N PDT (bottom right).

2.7 L-band Experimental

A resonator built similarly to the 700 MHz CLR was constructed to operate at approximately 980 MHz by Dr. George Rinard. To test the background method, the same magnet and spectrometer were used as at 700 MHz [37], with the only difference being the resonator and a DC block present between the resonator and the input to the detection system on the bridge. The DC block was initially introduced to reduce electrical coupling between the resonator and detection system. The DC block also provides better resonator coupling and an improved tuning pattern. The B_0 reversal method was tested using a sinusoidal rapid scan frequency equal to 4.888 kHz and a 32 G sweep width. Experiments have not been repeated without the DC block at 980 MHz because the CLR is difficult to tune without it. However, at 700 MHz, the presence or absence of the DC block did not change the relative contributions of field dependent and independent background.

Figure 2.23: 3D printed cylinder sample holder used for L-band imaging experiments. Each chamber was filled with 0.2 mM OX63. A 2 mm divider separates the cylinder into two equal compartments along the Z axis.

A 0.2 mM aqueous solution of OX63 was placed in a 3D printed cylinder 25 mm OD x 32 mm long printed with acrylonitrile butadiene styrene (Figure 2.23). A 2 mm divider separated the tube into equal chambers along the Z direction. The sample was air saturated.

2.8 L-band Results

Initially, the same modified B_0 reversal procedure that was used at 700 MHz was applied at 980 GHz. The two additional scans, A and B were collected at zero Gauss. Interestingly, the background at 1 GHz was entirely field independent, whereas at 700 MHz only a portion of the background was field independent. At 980 MHz, the zero gauss scans, A and B, were sufficient to remove background from scans 1 and 2, respectively. The relative contributions of field dependent and independent background may depend on rapid scan frequency or resonator design. Figure 2.24 shows sinusoidal rapid scans collected at

980 MHz of the 3-D printed phantom (Figure 2.23) containing aqueous 0.2 mM OX63 at 0 G/cm.

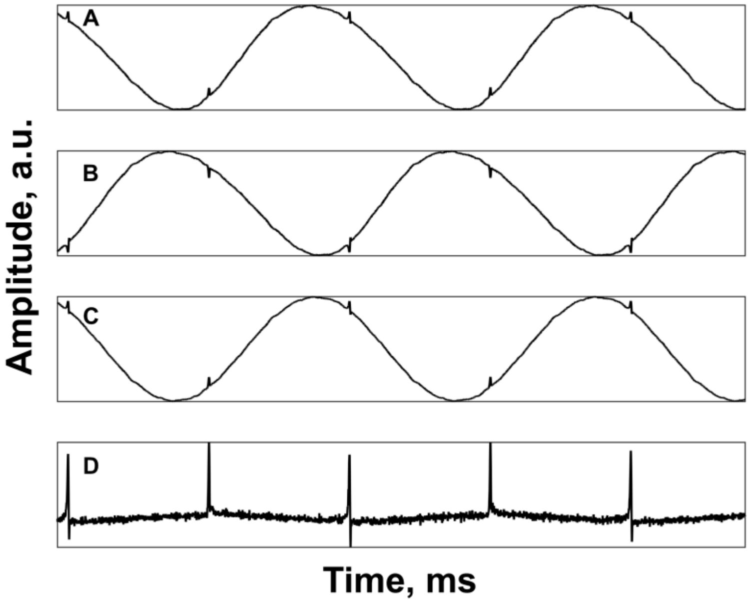

Figure 2.24: Sinusoidal rapid scans of phantom (Figure 2.23) containing 0.2 mM OX63 at 980 MHz. Only one channel is shown for simplicity. B_0 = 350.2 G, scan frequency = 4.888 kHz, sweep width = 32 G, incident power = 10 mW. (A) scan 1 (B) scan 2 (C) scan 1 - scan 2 (D) (scan 1 – scan A) – (scan 2 – scan B).

When the B_0 reversal method is working as expected based on the results at VHF, the EPR signal is inverted and the background remains unchanged in scan 2 relative to scan 1. At 980 MHz, the EPR signal and background inverted in scan 2 relative to scan 1 (Figure 2.24B), indicating that the background did not invert when B_0 was reversed. Further evidence that the background does not depend on B_0 was observed in scan A (Figure 2.25B), collected at 0 G. The background did not change shape or amplitude when the field was decreased to 0 G. Thus, the background can be removed at 980 MHz under the

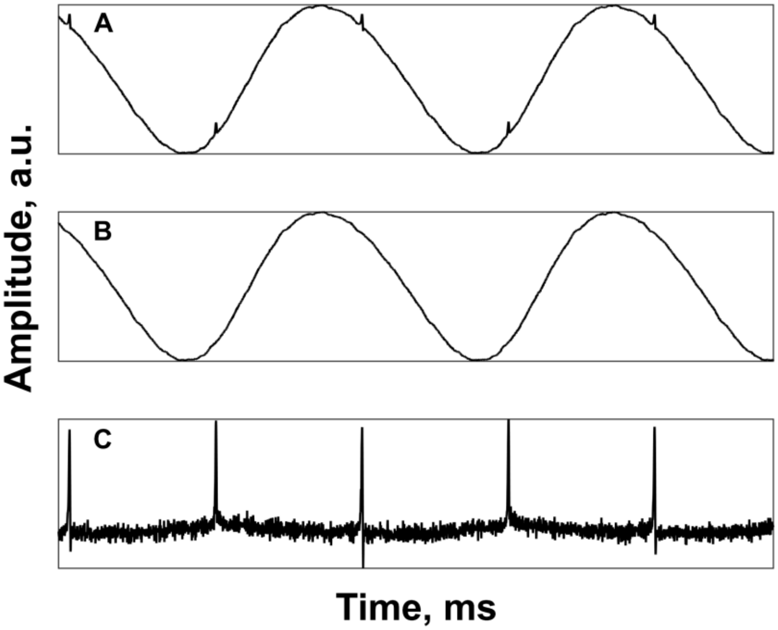

Figure 2.25: Off resonance subtraction of sinusoidal scans of phantom containing 0.2 mM OX63 at 980 MHz. Only one channel is shown for simplicity. B_0 = 350.2 G, scan frequency = 4.888 kHz, sweep width = 32 G, incident power = 10 mW. (A) scan 1 (B) scan A (C) scan 1 – scan A.

conditions reported by subtracting an off-resonance spectrum (Figure 2.25C) because the background did not change as a function of B_0.

An image was collected of the phantom containing 0.2 mM OX63 at 980 MHz using Z gradient that varied +/- 10 G/cm for a total of 101 projections. Reconstructed images are shown in Figure 2.26. When an off-resonance spectrum is not subtracted, the background in scan 1 is significant and affects the image quality (Figure 2.26A). After the off-resonance subtraction of scan A, the background is reduced and the image is improved (Figure 2.26B). The B_0 reversal method and the post processing background removal method [31] were not used in reconstruction of the images shown in Figure 2.26.

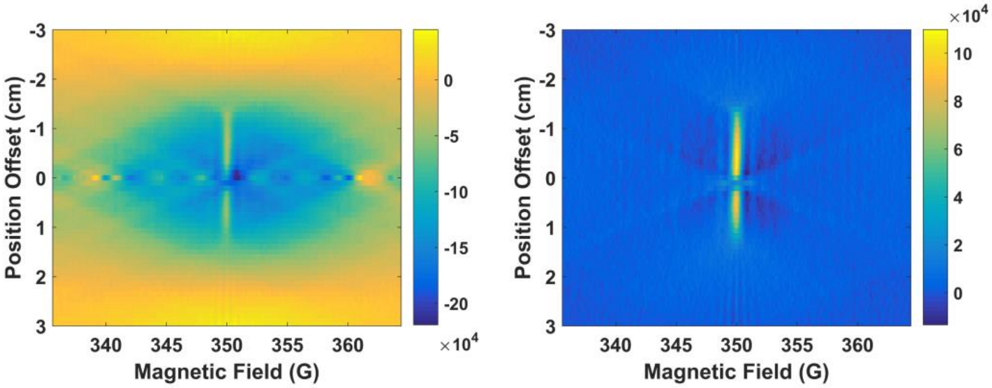

Figure 2.26: 2D spectral-spatial images of phantom containing 0.2 mM OX63 at 980 MHz. B_0 = 350.2 G, scan frequency = 4.888 kHz, sweep width =32 G, Z-gradient = +/-10 G/cm, 0.2 G/cm steps, incident power = 10 mW, spatial resolution = 1 mm. (A) scan 1. (B) scan 1 – scan A.

2.9 Summary and Future Directions

Eliminating background signals is a major step towards improving rapid scan data collection. Separation of EPR signal from background signal is most effectively accomplished when no assumption is made about the background. The field dependent rapid scan background using the 16 mm resonator at VHF for both triangular and sinusoidal scans was removed by using a new data acquisition procedure that reverses B_0 and offsets the data acquisition trigger by 180° between scans, denoted as scan 1 and scan 2. Rapid scan images of one aqueous and one non-aqueous phantom were collected at VHF in the 25 mm CLR. The B_0 reversal method was more successful for the non-aqueous phantom than for the aqueous phantom (Figures 2.11 and 2.13). Future work at VHF should test the B_0 reversal procedure on a variety of imaging phantoms, especially weak or broad samples, using both the 16 mm and 25 mm CLRs.

At 700 MHz, the rapid scan background was more complicated than at VHF but background can still be removed using the data acquisition procedure outlined at VHF with the addition of acquiring two 0 G scans (scan A and scan B), with other conditions the same as in scan 1 and scan 2. When a gradient is applied, all four scans had to be acquired at each gradient value. Plots of background versus B_0 and gradient strength showed that the background was not symmetric in either case about 0 G as we would expect for field dependent background. In the future, the reproducibility of the background as a function of B_0 and gradient strength (Figures 2.18 and 2.19) should be investigated. Two-dimensional spectral-spatial imaging at 700 MHz showed that the new B_0 reversal method, when combined with the 0 G scans, worked as well as the post-processing method described in [31].

At 980 MHz, the background was entirely field independent and the B_0 reversal method was not used. Instead, the background at 980 MHz was successfully removed by subtracting an off-resonance scan at each projection. The image quality is improved after off resonance subtraction.

There is a dominant contribution of field independent background at 700 MHz and 980 MHz but not in the 16 mm VHF resonator. This may be due to differences in resonator design. At 700 MHz and 980 MHz, both the driven and sample resonators of the CLRs are saddle coils oriented orthogonal to one another with axial symmetry along the direction of B_0. At VHF, the 16 mm CLR has a driven resonator that is a saddle coil and a sample resonator that is a classic loop gap resonator with many parallel fine wires [33]. The 25 mm VHF resonator uses a saddle coil for the driven resonator and a loop gap resonator for the sample resonator. Future work should aim to unravel the contributions to background at various RF frequencies in relation to resonator design and scan frequency.

Chapter 3: A 700 MHz to 1 GHz Rapid Scan and Pulse EPR Spectrometer

3.1 Introduction

Development of EPR spectrometers has primarily been at X-band due to the availability of commercial components. X-band has also been found to be a convenient tradeoff between increasing signal and limitations on sample size at higher frequencies. More recently, as technology has advanced, the EPR community has moved to lower frequencies for imaging applications.

Sato-Akaba et. al recently reported development of a digital CW-EPR spectrometer that uses a band-pass subsampling method to detect EPR spectra at 750 MHz [38]. Sato et. al reported a 700 MHz CW spectrometer that utilizes a 20 mm diameter high Q loop gap resonator to increase signal intensity in EPR experiments [39]. Krishna et. al developed a pulse EPR spectrometer operating at 300 MHz to detect tumor oxygenation in mice [40].

Two collaborations, one with the University of Chicago/University of Maryland and another with Bruker Biospin, have contributed to development and testing of a low frequency (700 MHz to 1 GHz) table-top imaging spectrometer at DU. The frequency selection permits imaging depths appropriate for mice studies [41]. New features of this spectrometer include a small table-top electromagnet powered by compact bipolar ethernet controlled power supplies, a 25 mm cross-loop resonator large enough to accommodate a mouse, and an arbitrary waveform generator (AWG) as the radiofrequency (RF) source. This spectrometer is described in Ref. [37].

3.2 Spectrometer Design

A block diagram of the 700 MHz to 1 GHz spectrometer is shown in Figure 3.1. The spectrometer is designed to perform rapid scan and pulse EPR. All components of the spectrometer were selected to operate between 700 MHz and 1 GHz except for the resonator which is narrow-banded but can be interchanged. The RF source is an 8-bit Tektronix 70002A AWG with an 8 Gs/s internal clock. The maximum output frequency of the AWG is 1.6 GHz. It has two independently controlled output channels each with two 1-bit markers that are used as trigger or activation signals for other components of the system. Although the two channels are independently controlled, they are derived from the

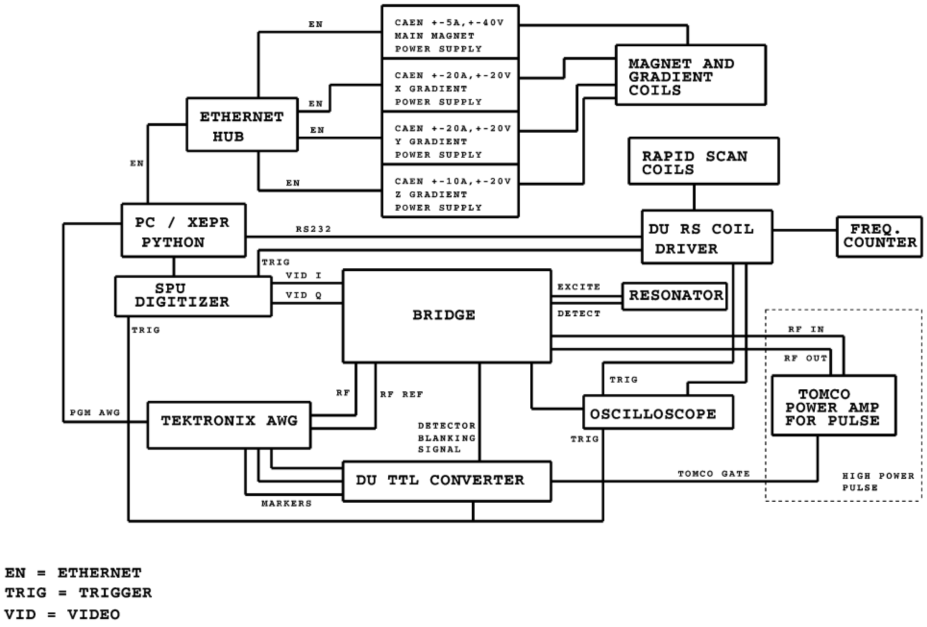

Figure 3.1: System diagram of 700 MHz to 1 GHz spectrometer. Figure is reproduced with permission from Ref. 37.

same clock and phase locked to each other. Two channels of RF from the AWG are routed to the bridge whose role is to amplify the RF prior to excitation of the spins in the resonator and also to amplify and detect the EPR signal after the resonator. The output of the bridge is two quadrature channels, I and Q, that are digitized by a Bruker Signal Processing Unit (SPU).

When used for rapid scan experiments, the AWG generates two channels of RF that are supplied to the bridge. The rapid scan coil driver (RSCD) described in [34] generates the rapidly changing magnetic field in coils external to the resonator. The RSCD also provides the digitizer trigger to the SPU. No marker signals are generated from the AWG during rapid scan experiments.

When used in high power pulse mode, an optional path shown in the dotted box of Figure 3.1 is used. In this path, RF pulses generated by the AWG exit the bridge and are amplified externally by a Tomco (400 MHz to 1 GHz) pulse amplifier before returning to the bridge and routed to the resonator. Marker signals generated by the AWG are amplified from 1 V to 2.75 V peak-to-peak by a locally built TTL converter. The higher voltage is necessary to trigger the detector blanking switch in the bridge that protects the detection system during high power pulses, and to activate pulse gates to form high power pulses using a Tomco amplifier. One additional marker signal is optionally passed through the TTL converter and split to trigger both a high-speed oscilloscope (Lecroy WaveRunner 640zi) and the SPU digitizer.

Rapid scan and pulse EPR require static magnetic fields. In addition, for imaging experiments, gradient magnetic fields are stepped to different strengths and combinations that correspond to projection angles. Magnetic fields are current controlled using four compact bipolar power supplies manufactured by CAEN Technologies. Commands sent over ethernet use locally written python code to change the magnetic field settings. The code is integrated with the Bruker data acquisition software (Xepr) to automate data collection for multi-dimensional imaging experiments and includes routines to perform the B_0 reversal method described in Chapter 2 and Ref. 32.

3.3 Arbitrary Waveform Generator

The RF source is a central piece of any spectrometer. In the past, at X-band, first klystrons and more recently Gunn diodes were used to generate continuous wave (CW) microwaves [42, 43]. To form pulses, high attenuation switches were used to turn the RF on and off. Recently, AWGs became available at the speeds needed to generate EPR frequencies. The programmability of AWGs allows for different experiments to be performed on the same instrument with ease. However, the power level of AWGs is typically low and must be amplified. The output of the AWG 7002A that was used for the experiments described here is about -2 dB_m. Of the two RF outputs, one is used for excitation (channel 1), and the other as the reference arm (channel 2).

Pulsed and CW waveforms were generated using locally written Matlab code and transferred to the AWG via USB. CW waveforms were generated by calculating the greatest common divisor (GCD) between the clock frequency of the AWG and the resonator frequency. This method was used to calculate the minimum number of points needed in a waveform such that the starting and ending point of the waveform did not have any discontinuity between each other. Any discontinuity in the waveform contributes to the phase noise of the source. When waveforms were created in this manner, the overall noise of the AWG was reduced (Figure 3.2) to the level that is equivalent to that of a Fluke 6082A which is a known low-noise source that we use in the 250 MHz spectrometer [44]. Another low-noise source, a Wenzel 500-29237C clock, was used as the external clock for the AWG [45]. The Wenzel clock outputs RF at a single frequency, 12.5 GHz, but can be divided down to 6.25 GHz and supplied to the AWG as an external clock. Driving the AWG in this way reduced the source noise of the AWG to the same level as using either the GCD method or the Fluke source. There is a constant level of thermal and digitizer noise up to about 0.15 mW (Log(power) = -3.8). Above about 0.15 mW, noise in the detected signal due to the AWG internal clock noise increases more rapidly compared to the Wenzel clock, Fluke source, and GCD +AWG method. Common powers used for rapid

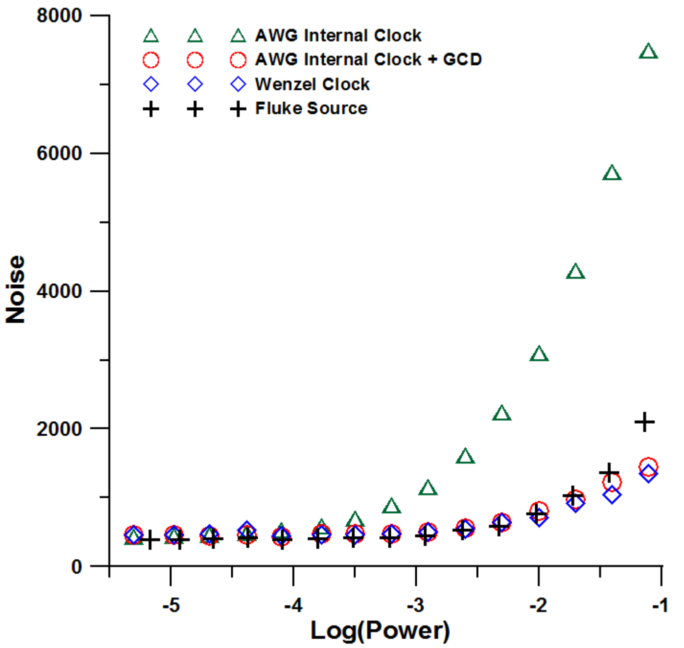

Figure 3.2: Source noise vs. Log(power) for several 700 MHz RF sources. Figure is reproduced with permission from Ref. 37.

scan experiments on this instrument fall between 0.6 mW and 80 mW which corresponds to Log(power) = -3.2 and -1.1 in Figure 3.2. In this region it is advantageous to use either the Wenzel clock, Fluke source, or the GCD +AWG method to reduce phase noise.

3.4 Bridge Design

A block diagram of the bridge is shown in Figure 3.3. All components of the bridge were selected to operate in the 700 MHz to 1 GHz range (Table 3.1). The bridge consists mostly of amplifiers and switches. The selection of paths in the bridge depends on the energized state of the mechanical and electrical switches (SW1 – SW7) as well as one transfer

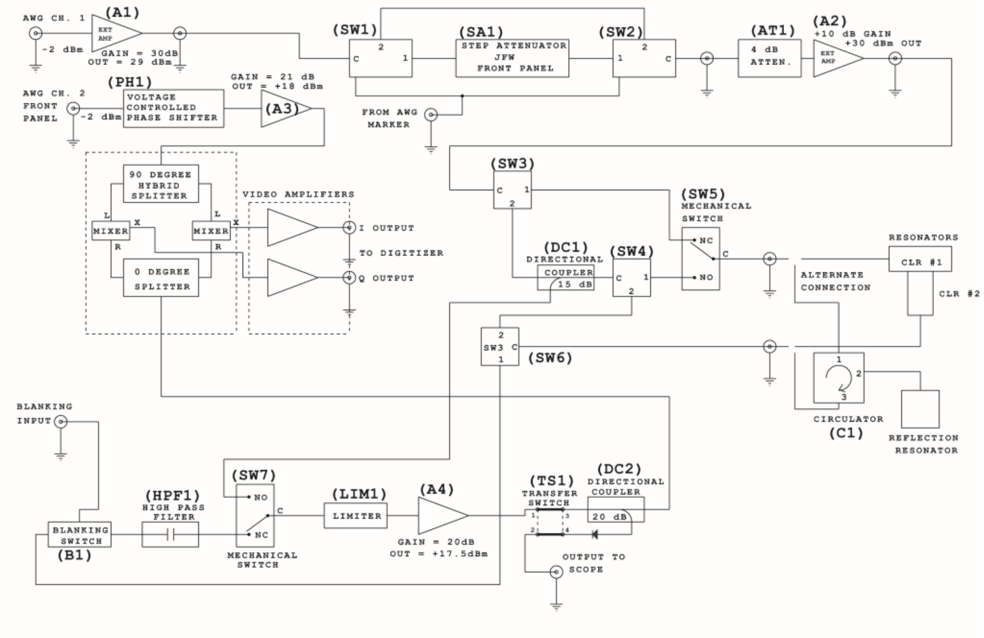

Figure 3.3: Block diagram of 700 MHz to 1 GHz bridge. Figure is reproduced with permission from Ref. 37.

Table 3.1: List of microwave components in 700 MHz to 1 GHz bridge. Table is reproduced with permission from Ref. 37.

Reference Designator	Device Type	Manufacturer	P/N	Gain	Output Level
(A1)	Amplifier	MiniCircuits	ZRL-1200+	+30 dB	+29 dBm
(SW1)	Electronic Switch	MiniCircuits	ZFSWA2-63DR		
(SA1)	Step Attenuator	JFW	50DR-001SMA		
(SW2)	Electronic Switch	MiniCircuits	ZFSWA2-63DR		
(AT1)	Fixed Attenuator			-4 dB	
(A2)	Amplifier	MiniCircuits	ZHL-1010+	+10 dB	+30 dBm
(PH1)	Voltage controlled phase shifter	Bel Power Solutions	HP1001		360^o for 10 V input
(A3)	Amplifier	MiniCircuits	ZX60-2522M-S+	+21 dB	+18 dBm
(SW3)	Electronic Switch	MiniCircuits	ZX80-DR230-S+		
(SW4)	Electronic Switch	MiniCircuits	ZX80-DR230-S+		
(SW5)	Mechanical Switch	MiniCircuits	MSPT-2-18-12+		
(SW6)	Electronic Switch	MiniCircuits	ZX80-DR230-S+		
(DC1)	Directional Coupler	MiniCircuits	ZFDC-15-5-S+	-15 dB	
(B1)	Electronic Switch	MiniCircuits	ZASWA-2-50DR+		
(HPF1)	High Pass Filter	MiniCircuits	SHP-700+		
(SW7)	Mechanical Switch	MiniCircuits	MSPT-2-18-12+		
(LIM1)	Limiter	MiniCircuits	VLM-33-S+		
(A4)	Amplifier	MiniCircuits	ZX60-P33ULN+	+20 dB	+17.5 dBm
(TS1)	Transfer Switch	MiniCircuits	MTS-18-12B		
(DC2)	Directional Coupler	MiniCircuits	ZX30-20-4	-20 dB	
(C1)	Circulator	UTE Microwave Inc	CT-1260-O		

Table 3.2: Switching logic for tune and operate paths.[a] Table is reproduced with permission from Ref. 37.

Path	**SW 1**	**SW 2**	**SW 3**	**SW 4**	**SW 5**	**SW 6**	**SW 7**	**TS1**
Tune CLR 1	C-1	C-1	C-2	C-1	C-NO	-	C-NO	1-2/3-4
Tune CLR 2	C-1	C-1	C-2	C-2	-	C-2	C-NO	1-2/3-4
Isolation/ Tune LGR	C-1	C-1	C-1	-	C-NC	C-1	C-NC	1-2/3-4
Operation	C-1	C-1	C-1	-	C-NC	C-1	C-NC	1-3/2-4

[a] The labeling of the switches is shown in Figure 3.3. An entry such as C-1 means that common position of the electronic switch is connected to output 1. An entry such as C-NO means that a mechanical switch is in the position that is identified as normally open.

switch (TS1). These switches select for operation or tuning paths. The tuning paths were made as similar as possible to operation paths to prevent changes in resonator coupling between tune and operate mode. The state of the switches for each path is shown in Table 3.2.

Bridge Inputs

The RF inputs to the bridge include the two AWG channels. Channel 1 is externally amplified before entering the bridge. The RF exits the bridge after SW2 to be externally amplified further. The Tomco pulse amplifier can be substituted for the amplifier, A2, which is shown in Figure 3.3. When the Tomco amplifier is used, additional attenuation is required at the input of the amplifier to keep the input power at about 0 dB_m. The RF again exits and re-enters the bridge at the resonator. The bridge was designed to operate with a CLR, but with the addition of an external circulator (C1) it can be used with a reflection resonator. Inputs requiring 1-bit marker signals are shown for the blanking switch (B1) and for SW1 and 2 (Figure 3.3). The blanking switch protects the detector when sent a 1-bit signal in the high state. The passive, non-blanked state is the low state. SW 1 and 2 were added as a modification to the bridge in October 2017 to facilitate saturation recovery experiments by providing the option to transiently bypass the JFW attenuator. For normal rapid scan and pulse operation SW1 and SW2 are in the low (passive) state in which the common terminal is connected to the RF 1 output (C-1), as listed in Table 3.2. When SW 1 and 2 are sent a 1-bit signal in the high state, the common (C) to RF 2 output is activated (C-2).

Bridge Outputs

Outputs of the bridge include the tuning signal and the I/Q quadrature channels. For any of the tuning paths, the transfer switch (TS1) is in the 1-2/3-4 position, and the output of the resonator (tuning signal) is directed out of the bridge to be digitized on a high-speed oscilloscope. Tuning the CLRs described here involves identifying and matching the frequencies of the two resonators and then adjusting the isolation between them to minimize RF transmission at the resonant frequency. Tuning the reflection resonators described here involves only identifying the resonant frequency. During the tuning procedure, a waveform generated by the AWG sweeps frequencies surrounding the center frequency of the resonator. The reflection from the resonator is detected on the scope which takes the Fourier Transform of the RF in real time. This displays a power spectrum as a function of frequency, similar to what is seen on a network analyzer. This allows the user to visually locate the resonator dip for tuning.

The outputs of a locally built double balanced quadrature mixer are the I and Q channels. The mixer is a key component in the bridge whose role is to combine the reference arm frequency with the excitation RF modulated by the EPR signal. After mixing the two together, the result is the sum and difference of the two frequencies. The difference of the frequencies is detected and the signals are routed through two video amplifiers whose bandwidth is about 2.4 MHz. The noise figures (NF) for the I and Q channel video amplifiers are 15.4 dB and 15.9 dB, respectively [37].

Noise Figure

The end-to-end overall gain and NF of the detection system were measured at 700 MHz using the +40 dB video gain setting and the procedure described in Ref. [46, 47] using a Fluke 8922A true RMS voltmeter with a sensitivity of -65 dB_m. A 32.4 dB calibrated noise source was connected in place of the sample resonator and the noise was measured at the output of the video amplifiers. The measured NF and gain of the I channel were 11.2 ± 0.7 dB and 48.9 ± 0.1 dB, respectively.

The spectrometer can be modeled using the Friis equation for cascading amplifiers, given in Ref. [47]. Four terms were used to model the system. Two terms represent the first

Table 3.3: Noise figure and gain values at 700 MHz. Table is reproduced with permission from Ref. 37.

	Noise Figure (dB)	**Gain (dB)**
Loss Before First Stage	+6.7	-6.7
First Stage Amplifier (A4)	+0.4	+21
Loss Between First and Second Stage Amplifiers	+5.5	-5.5
Second Stage Amplifier	+15.4	+40

and second stage amplifiers, respectively. The first stage amplifier, A4, has +21 dB gain and 0.4 dB NF. The second stage is the video amplifiers with +40 dB gain and 15.4 dB NF. Two additional terms are used in the Friis to account for losses in the system. Loss was measured by observing the peak to peak voltage on a 50-ohm scope before and after each component in the system. A total loss of -6.7 dB was measured from the resonator to the first amplifier, A4. An additional loss of -1 dB was measured between A4 and the 0° splitter leading into the quad mixer. There is an estimated total loss of -4.5 dB originating from the splitter and mixer amounting to a total loss of -5.5 dB. When these gains and NFs, summarized in Table 3.3, are inserted into the Friis equation [47], a total NF of 9.9 dB is calculated, which is in reasonable agreement with the measured value of 11.2 dB.

3.5 Resonators

Dr. George Rinard constructed two CLR and two reflection resonators that resonate at frequencies between 700 MHz and 1 GHz to be used on this spectrometer. Interchanging the resonators is quick and simple to do. CLRs are used on many of our low frequency spectrometers [33]. CLRs do not need to be critically coupled because source power is not reflected back to the detector. Instead, a CLR is composed of two orthogonal resonators that are usually a combination of saddle coils or LGRs. In normal operation, they are used in transmission mode and the RF excites the first resonator typically referred to as a “driven” resonator. A voltage (EPR signal) is induced in the second resonator called the “sample” resonator. The isolation between the driven and sample resonators is adjusted to minimize RF transmission to the sample resonator. Good isolation reduces phase noise commonly associated with RF sources.

700 MHz CLR

A 700 MHz CLR is shown in Figure 3.4. In this CLR, both the driven and sample resonators are saddle coils. Characteristics of the resonator listed in Table 3.4 were measured on a HP8719D network analyzer with an aqueous sample in the resonator. This resonator can be used for rapid scan or pulse experiments. The rapid scan coils that are used with this resonator have 88 turns of 220/46 Litz wire and a coil constant of about 15.7 G/A measured by comparing ^{13}C hyperfine for trityl-CD_3 to literature vales [48]. The inductance of the coils is about 1.9 mH, calculated by resonating the coils with a known capacitance, C and then solving for the inductance (L) using equation 3.1.

$$L = \frac{1}{(2\pi f)^2 C} \quad \text{eq. 3.1}$$

The efficiency of the driven resonator was calculated by using equation 3.2 to solve for the B_1 needed to achieve a 90° pulse and then measuring the corresponding power.

$$\text{flip angle} = \gamma B_1 T_p \quad \text{eq. 3.2}$$

The efficiency is about 0.11 G $\sqrt{W}$. Resonator efficiency describes the conversion of power to B_1, which is the microwave (RF) magnetic field in the resonator that excites the spins.

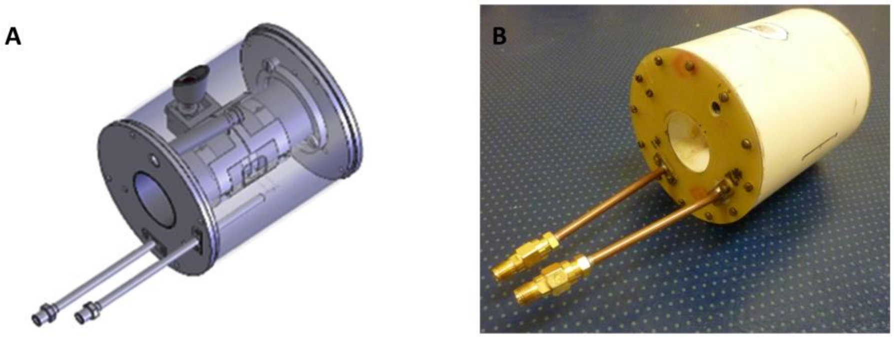

Figure 3.4: 25 mm 700 MHz CLR. (A) Drawing of 700 MHz CLR. (B) Picture of 700 MHz CLR. Figure is reproduced with permission from Ref. 37.

Table 3.4: Characteristics of the 25 mm 700 MHz CLR.

Typical resonant frequency with aqueous sample	697-704 MHz
Driven resonator Q	40
Sample resonator Q	40
Isolation with aqueous sample	30-35 dB
Efficiency of driven resonator	$0.11\ G/\sqrt{W}$
Length of sample resonator	38 mm
Diameter of sample resonator	25 mm

700 MHz LGR for Small Samples

A 2.4 mm inner diameter (ID) Alderman-Grant LGR [49] made by George Rinard was mounted on the end of a ¼ inch square ruler. This resonator, shown in Figure 3.5, resonates at around 732 MHz, has a Q of 54, and was used for low power pulse experiments and small non-aqueous samples.

A substantial improvement in signal to noise was observed when the 2.4 mm resonator was placed inside the 25 mm CLR. To quantify this phenomenon, two of the 2.4 mm resonators, containing deoxygenated Lithium phthalocyanine (LiPc) sealed in 2 mm outer diameter (OD) glass tubing were mounted on a plexiglass support. The plexiglass and small resonator assembly is shown in Figure 3.6. When it is placed inside the 25 mm CLR, the small resonators couple to the larger CLR. Rotation of the sample holder changes the coupling such that the frequency of the small resonators matches the frequency of the CLR. Rapid scan spectra of LiPc were measured at 3.88 kHz using the CLR with and without the assembly shown in Figure 3.6. The signal to noise increased by a factor of 140 (Figure 3.7) when the small resonator assembly was present. The increase in signal to noise is likely due to a concentration of the B_1 field at the sample, yielding a higher filling factor than the 25 mm CLR alone.

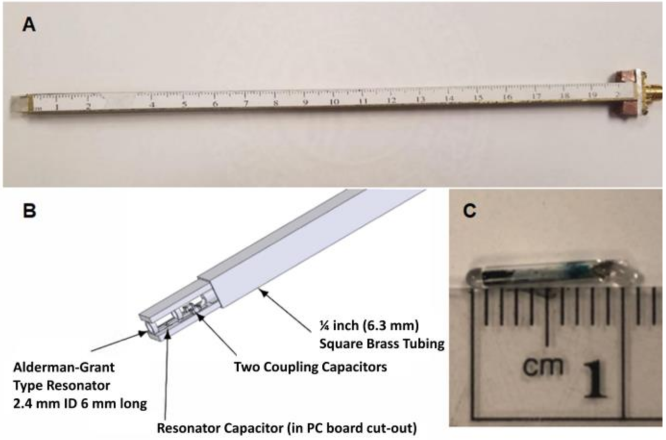

Figure 3.5: 2.4 mm 732 MHz LGR. (A) Picture of 732 MHz LGR assembly used to probe magnetic field uniformity. (B) Sketch of field probe pictured in part A. (C) LiPc sample used for field homogeneity, magnet stability, and signal to noise enhancement measurements. Figure is reproduced with permission from Ref. 37.

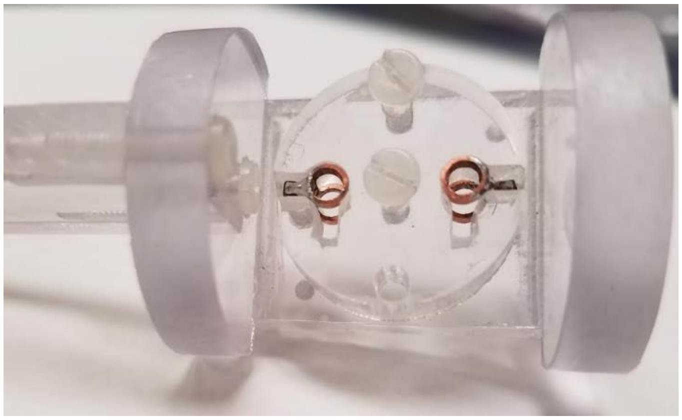

Figure 3.6: 700 MHz 25 mm CLR sample holder shown with two 700 MHz 2.4 mm ID Alderman-Grant resonators.

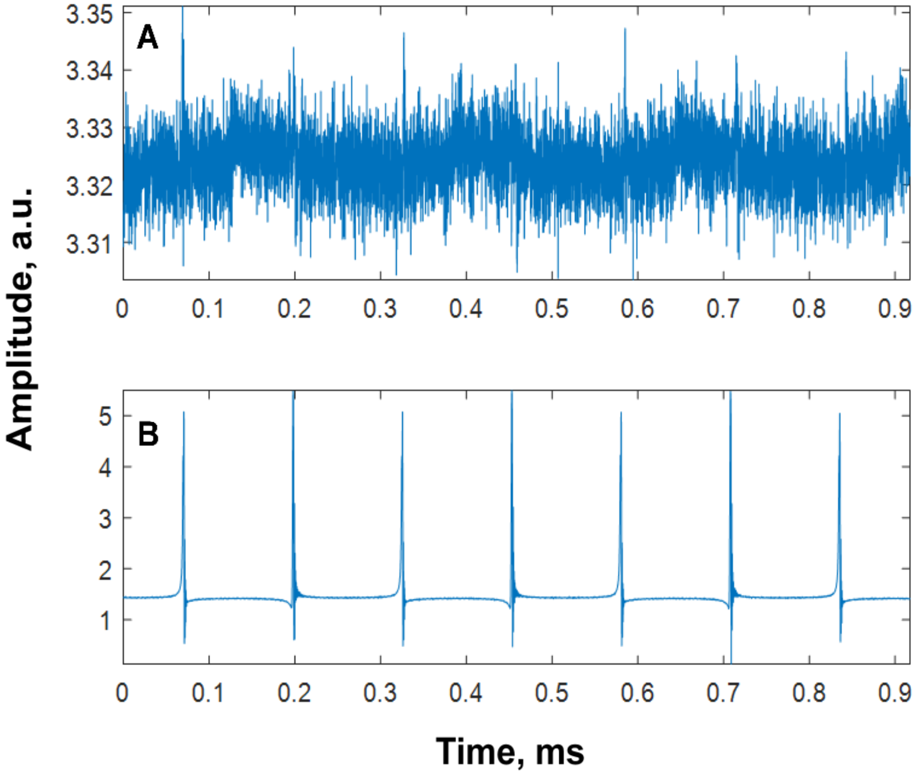

Figure 3.7: Sinusoidal rapid scans of LiPc recorded in 25 mm 700 MHz CLR without (A) and with (B) 2.4 mm ID Alderman-Grant type resonators. Scan frequency = 3.88 kHz, sweep width = 14 G. Incident power ~ 8 µW.

1 GHz CLR

A 25 mm ID 1 GHz CLR, shown in Figure 3.8, consists of two saddle coils for the driven and sample resonators. The resonator characteristics measured on a HP8719D network analyzer are listed in Table 3.5. This resonator can be used for rapid scan or pulse. Rapid scan images collected with this resonator are presented in Chapter 2.

Figure 3.8: 25 mm 1 GHz CLR.

Table 3.5: Characteristics of the 25 mm 1 GHz CLR.

Typical resonant frequency with aqueous sample	934 MHz
Driven resonator Q	20
Sample resonator Q	30
Isolation with aqueous sample	20 dB
Diameter of sample resonator	25 mm

1 GHz LGR for Small Samples

A 2.4 mm ID Alderman-Grant (LGR) resonator similar to the 700 MHz resonator was built by George Rinard for 1 GHz. This resonator resonates around 1.014 GHz and is overcoupled. This resonator was used for low power pulse experiments with non-aqueous samples.

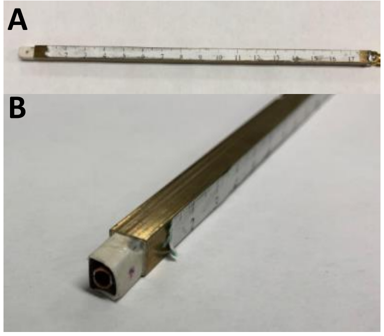

Figure 3.9: 2.4 mm 1.014 GHz LGR (A) Resonator mounted to end of ¼ inch square ruler. (B) Close up of 2.4 mm ID resonator.

3.6 Electromagnet and Gradient Coils

Main Magnet

The electromagnet that supplies the B_0 field consists of 4 coils, each with 24 turns per layer and 20 layers of No 14-square magnet wire (Figure 3.10). The two inner coils have a 19.1 cm average diameter and the outer coils have a 14.7 cm average diameter. The resistance of the magnet is about 7 Ohms, and the magnet coil constant is about 78.5 G/A. The magnet sits on an aluminum base that acts as a heat sink. Power consumption is about 70 Watts at 250 G (700 MHz) and 147 Watts at 360 G (1 GHz). The magnet assembly weights about 60 lbs.

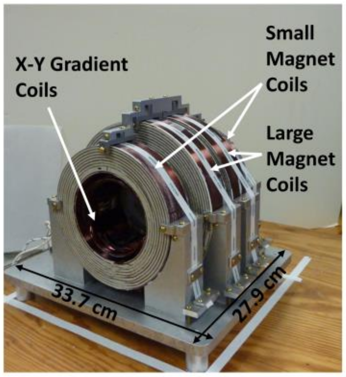

Figure 3.10: Picture of 700 MHz magnet. The outer diameter of the small and large magnet coils is 18.2 and 22.6 cm, respectively. The inner diameter of the small coils is 11.3 cm. The Z-gradient coils are concentric with the main magnet coils, and fit inside the large magnet coils. The Z-gradient coils have the same inner diameter as the small magnet coils. The X-Y gradient saddle coils are pictured inside the main magnet and Z-gradient coils. Figure is reproduced with permission from Ref. 37.

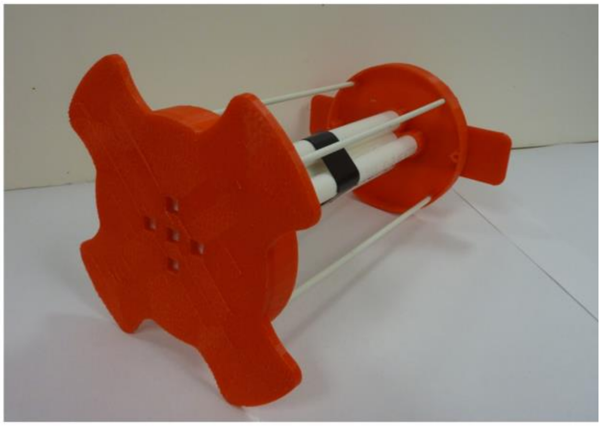

Figure 3.11: 3D printed positioning system used to guide 2.4 mm LGR for field uniformity measurements. Figure is reproduced with permission from Ref. 37.

Field Uniformity Measurements

A procedure to map the magnetic field homogeneity using pulse EPR was developed. The 732 MHz 2.4 mm LGR (Figure 3.5) containing a 1.1 mm ID x 2 mm long LiPc sample was moved to known locations in the magnet using the positioning system shown in Figure 3.11. At each location, a 500 ns pulse was applied to generate a free induction decay (FID). The frequency of the FID is well defined in the Fourier domain and was converted to a magnetic field value using the gyromagnetic ratio of the free electron. The spacings between the coils determine the field uniformity and an iterative process of measuring the field uniformity and adjusting the coil spacings was required to achieve good uniformity. A locally written Mathcad program generated the optimal spacings between coils that were used as a starting point. The field uniformity was measured and fed back into the Mathcad program that calculated the adjustments needed to achieve better field uniformity. Adjustments in the coil spacings were made using a dial indicator. The non-uniformity after the best possible adjustment had residual gradients along X, Y, and Z directions, listed in Table 3.6.

The field uniformity was also measured with the same LiPc sample at approximately 1 GHz using the 1 GHz LGR shown in Figure 3.9. The same residual gradients were measured at 1 GHz as were measured at 700 MHz.

Gradient Coils

Additional coils, designed to generate 10 G/cm, provide linear gradients in $\overrightarrow{B_z}$ for imaging experiments (Figure 3.12). The net field is always along z and is designated $\overrightarrow{B_z}$, but the magnitude of $\overrightarrow{B_z}$, in the presence of gradients, varies with respect to X, Y, and Z.

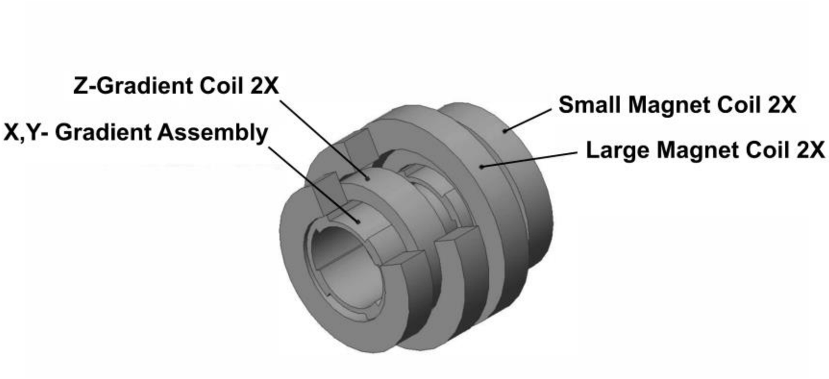

Figure 3.12: Cut-away view of 700 MHz to 1 GHz magnet and gradient coil system.

These gradients can be expressed as $\overrightarrow{\frac{dB_z}{dx}}$, $\overrightarrow{\frac{dB_z}{dy}}$, $\overrightarrow{\frac{dB_z}{dz}}$. The two gradient Z-coils are built into the magnet and are the same diameter as the small outer coils of the main magnet as shown in Figure 3.12. They consist of 7 layers with 12 turns per layer No. 10 square magnet wire. The X and Y gradient coils each consist of 4 coils wound in 2 layers with 10 turns of No. 14 square magnet wire. The X, Y, and Z gradient coils fit snugly inside the main magnet (Figure 3.12).

Gradient coil constants were measured using the same procedure, resonator, positioning device, and LiPc sample that were used for field-uniformity measurements. Gradient currents from 0.1 A to 0.5 A were applied and the FID frequency was recorded for each current value. At each gradient current value, the sample was moved a known distance along X, Y, or Z and the measurements were made again. The change in Gauss over the change in position was plotted versus the applied gradient current (Figure 3.13). The gradient coil constants were calculated from the slope of the line. Small non-zero y-intercept offsets indicate small DC offsets in the magnet power supplies.

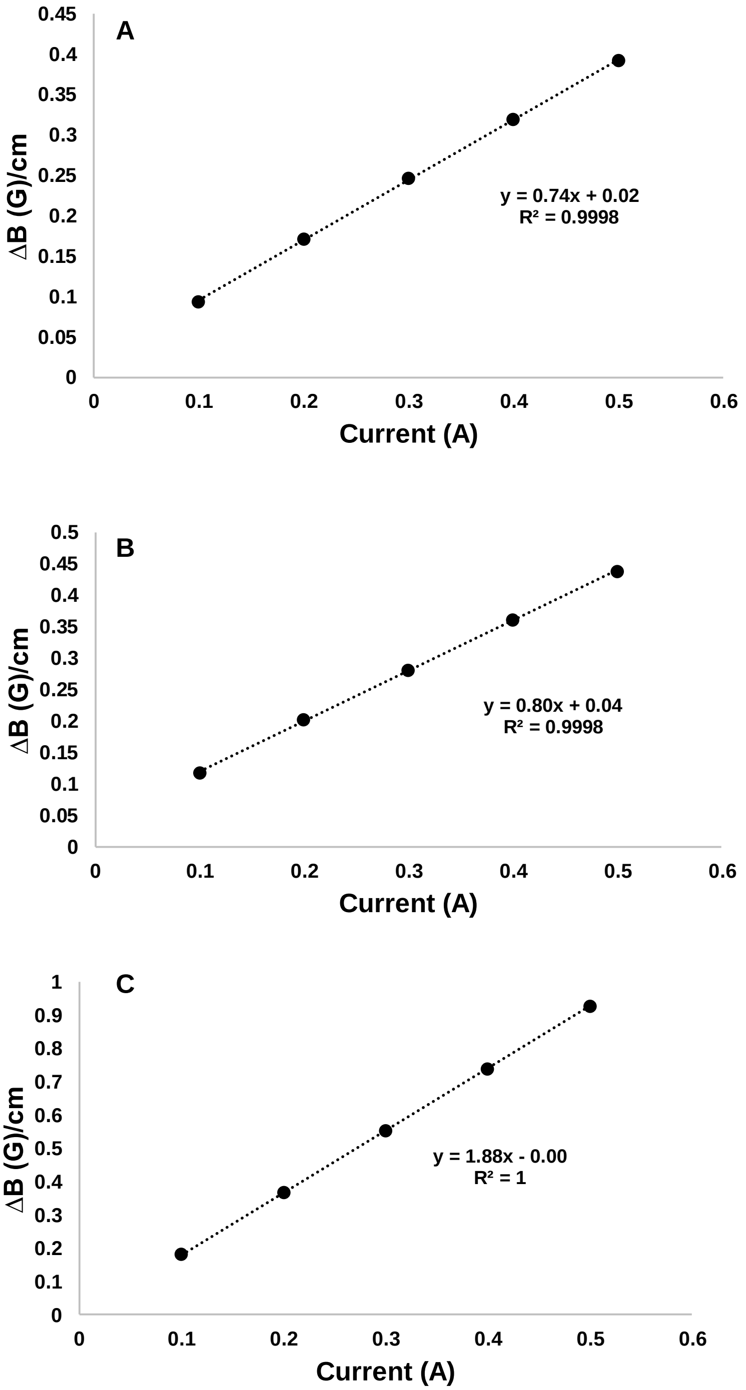

Figure 3.13: Gradient coil constant calibration curves for 700 MHz to 1 GHz spectrometer. (A) X-gradient coil constant calibration curve. (B) Y-gradient coil constant calibration curve. (C) Z-gradient coil constant calibration curve.

Application of gradients equal in magnitude and opposite in direction to the residual gradients after best possible adjustment (Table 3.6) cancel out the residual gradients such that field uniformity is improved.

Table 3.6: Measured residual nonuniformity in magnetic field over the sample space before and after corrections with gradient coils. Ppm is calculated out of 252 G. Table is reproduced with permission from Ref. 37.

Axis	**Residual gradients - No corrections (G/cm)**	**Residual gradients - With corrections (G/cm)**
X	0.034 (135 ppm)	0.001 (4 ppm)
Y	0.049 (194 ppm)	0.002 (8 ppm)
Z	0.006 (24 ppm)	0.006 (24 ppm)

Temperature Measurements

Four thermocouples were placed at locations on the surface of the magnet coils (Figure 3.14), and the temperature of the magnet was measured as a function of time. A small Honeywell fan was blowing air down the bore of the magnet to remove excess heat throughout the measurement. The main magnet was initially energized to 250 G (700 MHz) and all three gradients to 10 G/cm. The 700 MHz CLR and rapid scan coils were placed inside the magnet. The rapid scan current was set to 3.8 A (60 G). These conditions represent an extreme situation at which heating would be at a maximum. After being on for 105 min, the temperature at the thermocouples stabilized between 25 and 38 °C. The main magnet field was then increased to 350 G. After an additional 107 minutes, the temperatures stabilized between 25 and 45 °C. Finally, the field was increased to a maximum value of 385 G (1.08 GHz). Thermocouple 2, located between the sample and inner wall of the resonator, stabilized after 1 hour at 25 °C. The hottest temperature (48 °C) was recorded at the thermocouple position labeled 4, which was placed between the main magnet and the X-, Y- gradient coils on the side opposite of the fan.

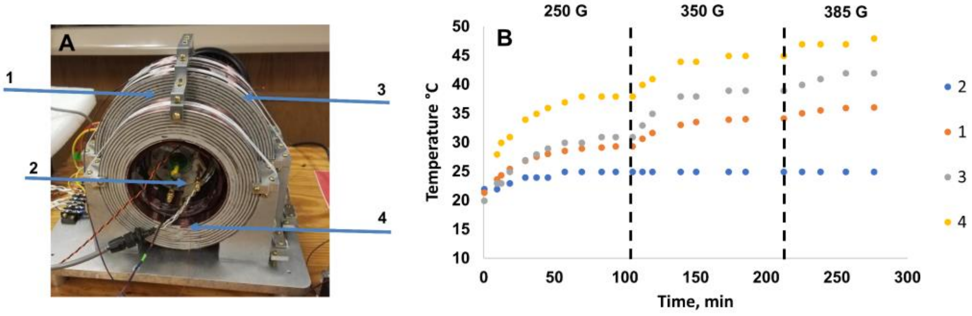

Figure 3.14: Temperature measurements of 700 MHz to 1 GHz electromagnet. (A) Positions (1-4) of four thermocouples. (B) Temperature at thermocouples in (A) as a function of time.

3.7 Magnet Power Supplies

Main Magnet

The B_0 field is controlled by a FAST-PS 0540-200 power supply manufactured by CAEN Technologies (Figure 3.15D). The supply is operated in constant current mode and has 18-bit current setting resolution from -5 to 5 Amps. A noise reducing filter that is specified for a maximum 20 ppm (full scale) peak-to-peak ripple was implemented on the supply to reduce current noise that is common to switching supplies. A key feature of this supply is that it is bipolar, enabling the B_0 reversal procedure outlined in Chapter 2. Remote commands are sent over Ethernet using locally written python code.

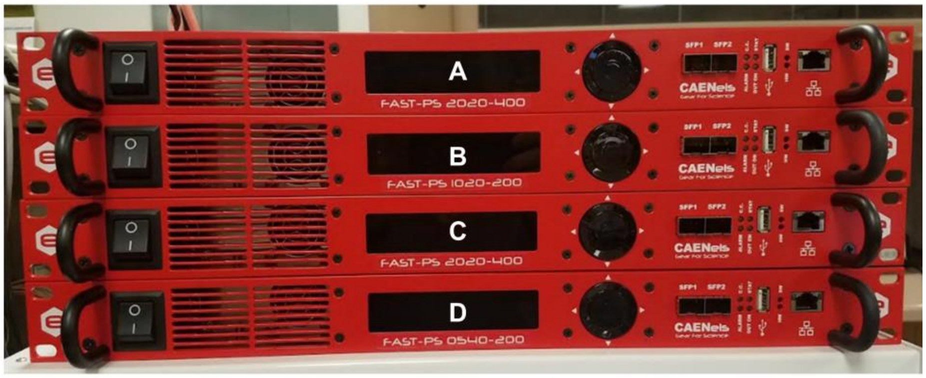

Figure 3.15: CAEN power supplies. (A) X-gradient power supply. (B) Z-gradient power supply. (C) Y-gradient power supply (D) main magnet (B_0) power supply.

Before selecting the CAEN FAST-PS series, several power supplies were tested for magnetic field stability at 260 G. The same procedure, resonator, and LiPc sample were used as for the field uniformity measurements described above. However, for the stability tests, the LiPc sample was placed in a static position and repeated measurements were collected over time. The LiPc FID signal was strong and only 100 averages were collected so that the total data acquisition time for one scan was 10 ms. At least 20 replicate measurements were used to calculate the standard deviation of the position of the FID in the Fourier domain. The standard deviation is reported as the stability of each power supply unit. For these tests, gradients were not in use.

Standard Bruker EPR spectrometers use a Hall probe to sense the magnet field and relay signals in a feedback loop to a Bruker field control unit. Hall probes are field sensing devices commonly used for iron-core magnets. For imaging applications, gradient fields interfere with the field and software corrections are required. Direct current control of B_0 is more practical. Several power supplies were tested for stability in constant current mode (Table 3.6). As a standard for comparison against various power supplies that could potentially be used for direct current control, a conventional Hall probe was tested. To test the Bruker EMX Nano and Bruker ESR2388/EMX080 20A power supplies, a Hall probe simulator device described in Ref. [50] was interfaced with Bruker field controllers to provide a current, instead of field sensing, feedback loop. The HP and CAEN power supplies were connected directly to the magnet without the field controller or Hall probe simulator in the circuit.

The Hall probe simulator was tested against the Hall probe using the same power supply, a Bruker ESR238-EMX080. The Hall probe was slightly more stable than the Hall probe simulator (Table 3.7). The Bruker EMX Nano power supply was considerably more stable than the Bruker ESR2388/EMX080 supply. The HP 6010A supply also performed well. However, the best results were obtained with the CAEN supply which may be in part due to the special filter on the supply to reduce current noise.

Table 3.7: Magnetic field stability at 260 G of several power supplies.

Power Supply	**Volts / Amps**	**Stability**
CAEN FAST-PS 0540-200	±40V / ±5A	± 1 mG (4 ppm)
HP 6010A	0-200V / 0-17A	± 11 mG (42 ppm)
Bruker EMX Nano + Hall Probe Simulator	0-10V / 0-6.5A	± 6 mG (23 ppm)
Bruker ESR2388/EMX080 + Hall Probe Simulator	50V / 20A	± 31 mG (119 ppm)
Bruker ESR2388/EMX080 + Hall Probe	50V / 20A	± 28 mG (77 ppm)

Gradient Power Supplies

The X and Y gradient coils are powered by CAEN FAST-PS 2020-400 supplies, and the Z gradient is powered by a CAEN FAST-PS 1020-200 supply (Figure 3.15 A-C). These bipolar supplies are also controlled remotely over Ethernet using locally written python code.

The stability of the Z-gradient power supply was evaluated by triangular rapid scans of two LiPc samples separated by 1.0 cm. Each LiPc signal had a linewidth of about 200 mG. These relatively spectrally sharp signals aided an accurate determination of field position. The Z gradient current was -1.0 A (~2 G/cm) and the standard deviation of the field separation between the two LiPc signals was measured for 5 replicate measurements (Figure 3.16). The stability of the gradient field was ± 16 mG. The 700 MHz CLR (Figure 3.4) was used for these measurements.

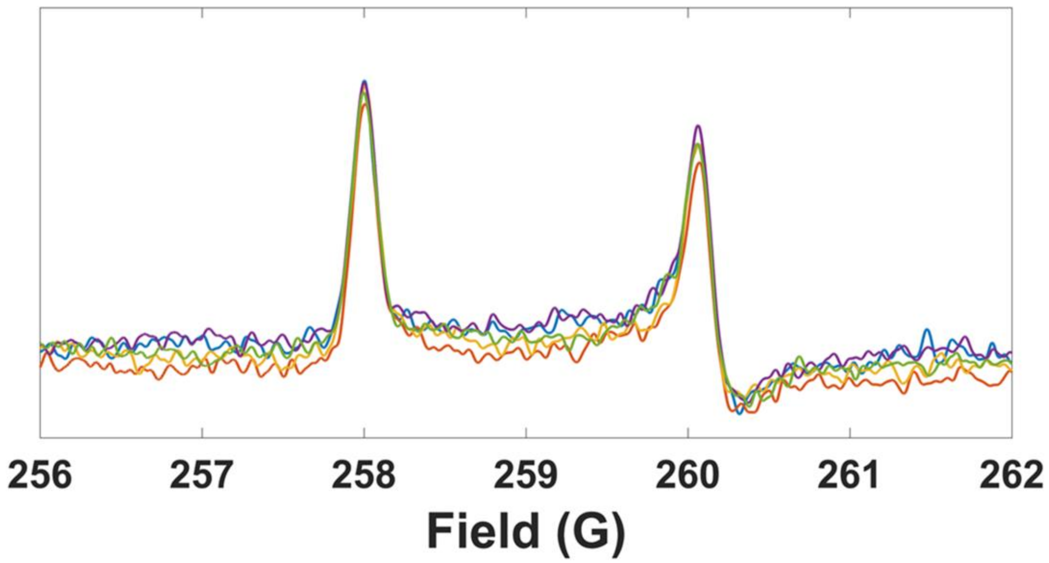

Figure 3.16: Triangular rapid scans of two LiPc samples to assess gradient field stability. The samples were separated by 1.0 cm along the Z axis. Five replicate measurements are shown. Z gradient = 1.0 A, scan frequency = 2.56 kHz, sweep width = 15.7 G.

3.8 700 MHz Rapid Scan Imaging

To demonstrate the capabilities of the new system, rapid scan imaging was performed on aqueous phantoms. Imaging experiments were performed at 700 MHz using the CLR shown in Figure 3.4. The version of Xepr that is on the PC for the 700 MHz spectrometer has a built-in python application programming interface (API) that allows the user to design unique experiments that facilitate incorporation of non-Bruker instruments. Data acquisition of rapid scan projections was performed using locally written python code that interfaced the CAEN power supplies, RSCD, and Xepr data collection software.

Imaging Samples and Phantoms

For 2- and 3D images, air saturated aqueous solutions of 1 mM Proxyl and 0.2 mM triarylmethyl OX63 were prepared. The imaging phantom consisted of a 3D printed cylinder (25 mm diameter x 32 mm long) with a 2 mm divider in the center that divided the cylinder into two equal compartments (Figure 2.23). The wall thickness was 2 mm.

For 4D images, a 0.1 mM OX63 solution was prepared in 2 mM HEPES buffer. Aqueous solutions of 1 mM Tempol (SigmaAldrich, St. Louis, MO) and ^{15}N per-deuterated Tempone (PDT, Cambridge Isotope Laboratories, Tewksbury, MA) solutions also were prepared. These solutions were bubbled with N_2 before being flame sealed in 25 mm diameter x 16 mm long cylinders. The wall thickness of the cylinders was about 1.5 mm. The Tempol and PDT cylinders were placed bottom to bottom to form an imaging phantom 25 mm diameter x 32 mm long (Figure 3.20).

2D Spectral-Spatial Imaging

A 2D spectral-spatial image of 1 mM Proxyl in both compartments of a 3D printed phantom (Figure 2.23) is shown in Figure 3.17. The projections were collected by varying the gradient strength along the Z axis. The gradient strength was varied between ± 10 G/cm

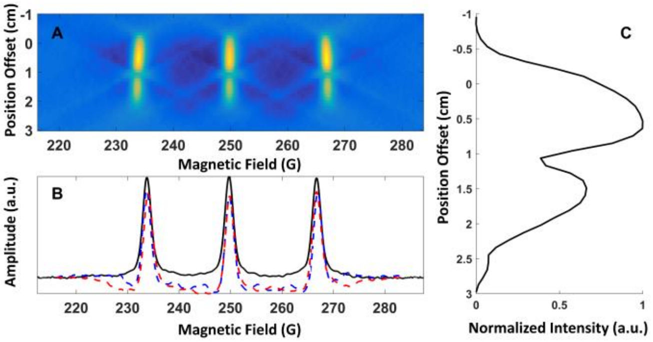

Figure 3.17: (A) 2D spectral-spatial imaging of 1 mM Proxyl at 703 MHz. Z gradient = ± 10 G/cm, scan frequency = 5 kHz, rapid scan sweep width = 76 G, 101 projections, spatial resolution = 1 mm. (B) Spectral slices through Z = 0.3 and 1.5 cm (red and blue dashed lines) superimposed on zero gradient spectrum (solid black line). (C) Spatial slice through B_0 =250 G.

with 0.2 G/cm steps generating 101 projections. Image reconstruction was performed using Matlab routines written by Dr. Mark Tseitlin [51].

2D Spatial-Spatial Imaging

Two dimensional spatial-spatial projections were collected by linearly stepping a gradient of constant strength in a plane defined by two spatial axes, X and Z. The projection step size, θ, was defined as 180° divided by the number of projections. The initial projection angle was θ/2. To generate the appropriate current (I) in the X and Z gradient coils equations 3.3 and 3.4 were used.

$$I_x = \sin(\theta) \quad \text{eq. 3.3}$$

$$I_z = \cos(\theta) \quad \text{eq. 3.4}$$

Imaging data were collected using a python program. When user-created experiments are run with the python API, the Xepr descriptor file does not contain the information needed for image reconstruction using a filtered back projection (FBP) routine in Xepr software. In order to use Xepr software for image reconstruction extra steps are required. First, rapid scan spectra are deconvolved in Matlab to yield the slow scan spectrum, organized into a 2D data set, and loaded back into the Xepr primary window. A 1D deconvolved zero gradient spectrum also needs to be loaded into the secondary window. Using the built-in deconvolution routine in Xepr, the line shape corresponding to the zero gradient spectrum is deconvolved out of the 2D dataset. This procedure assumes that the lineshape is the same throughout the sample. This new 2D data set contains projections with only spatial information. Next, a “dummy” descriptor file needs to be created that contains the correct projection step size, number of projections, number of points, etc. This is done by running a CW imaging experiment in Xepr that is set up with the correct parameters but does not the use the python API. The descriptor file should be renamed to match the deconvolved 2D dataset. The Xepr software can then be used to reconstruct an image from the 2D set of projections. The full CW experiment needs to be run once, and then the descriptor file can be edited for future images.

2D spatial-spatial images of air saturated 1 mM Proxyl (Figure 3.18A) and 0.2 mM OX63 (Figure 3.18B) were reconstructed using this procedure. In each of these images the 3D printed phantom (Figure 2.23) contained the same radical in both compartments. The gradient was 10 G/cm and 25 projections were collected in the XZ plane for each image.

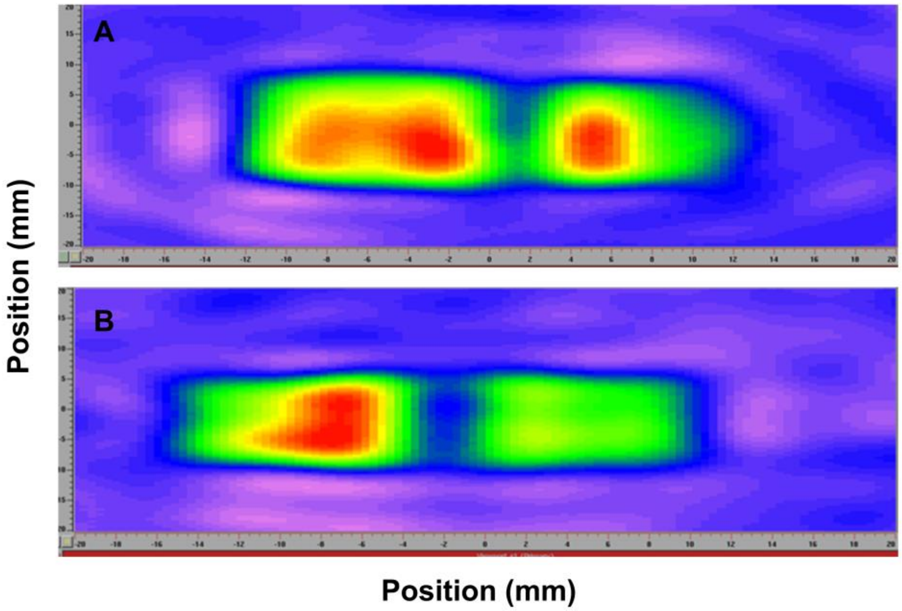

Figure 3.18: 2D spatial-spatial images of 1 mM Proxyl and 0.2 mM OX63 at 703 MHz. (A) 2D (XZ) spatial-spatial image of 1 mM Proxyl. Rapid scan frequency = 5.004 kHz, sweep width = 77 G, gradient = 10 G/cm, 25 projections. (B) 2D (XZ) spatial-spatial image of 0.2 mM OX63. Rapid scan frequency = 5.004 kHz, sweep width = 32 G, gradient = 10 G/cm, 25 projections.

3D Spatial Imaging

Three dimensional (all spatial) linearly spaced projections were collected by sampling a spherical region that contains the sample. A 3D image of the 3D printed phantom (Figure 2.23) containing 1 mM Proxyl in both compartments was acquired. The number of polar angles (θ) was equal to the number of azimuthal angles (φ) generating 100 total projections. The gradient was 10 G/cm and the projection step size was 18°. The same reconstruction procedure for 2D spatial-spatial images was used for 3D spatial images. A new "dummy" file was generated in Xepr to match the number of projections and gradient angles. The output of the Xepr reconstruction routine displays the image as a series of 2D slices (Figure 3.19). Communications with Bruker personnel led to the finding that the software does not have a method to render the slices as a 3-dimensional image. The exact data format was not conveyed to us at the time of communication. Thus, Xepr software has many limitations for image reconstruction with more dimensions than 2D spatial-spatial imaging.

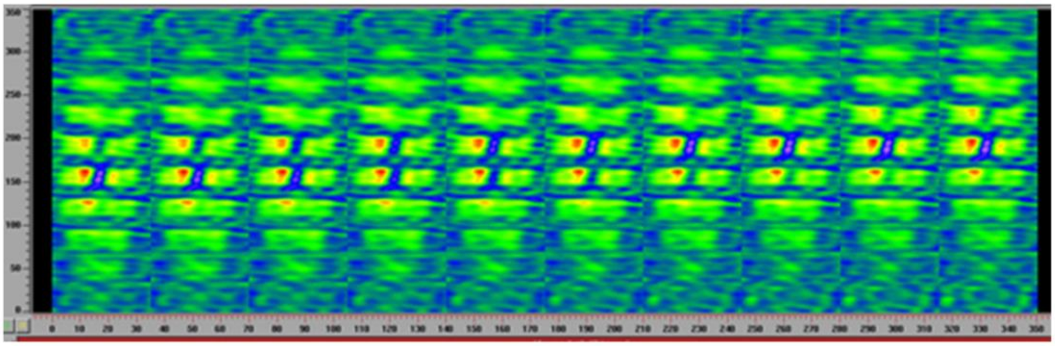

Figure 3.19: 3D spatial image of 0.2 mM OX63 at 704 MHz displayed as a series of 2D slices in Xepr. Rapid scan frequency = 5.013 kHz, sweep width = 62 G, gradient = 10 G/cm, 100 projections.

4D Spectral-Spatial Imaging

4D imaging presents the spectral properties of paramagnetic species as a function of three-dimensional space. This permits imaging of samples for which the EPR spectrum depends on location in the sample. Rapid scan projections were collected with an equal solid angle sampling scheme and the resulting projections were interpolated to yield linearly spaced projections [52]. An FBP algorithm was used for image reconstruction. The Matlab routines used in reconstruction were developed and maintained by Dr. Boris Epel, University of Chicago. A CW example provided at http://epr-it.specman4epr.com/ was modified for use with rapid scan data. Reconstruction of images with 64 bins for each spatial axis took approximately 90 seconds. Nitroxide spectra were reconstructed in three sections using zoom and offset parameters to focus on a portion of the spectrum at a time. The algorithm assumes that the signals from each line do not overlap at high gradient strengths. If overlap occurs the image quality is degraded.

A four dimensional (3 spatial, 1 spectral) rapid scan image of the phantom containing 0.1 mM OX63 and 1mM Tempol (Figure 3.20) is shown in Figures 3.21 and 3.22. Power was adjusted to be in the linear response range for OX63. The nitroxides saturate less readily than OX63. The rapid scan frequency was 3.13 kHz and the sweep width was 75 G. There were 14 spectral projections collected at 10 spatial projections for a total of 924 projections. The maximum gradient was 10 G/cm. The image took about 18 hours to collect. Since the samples were degassed, imaging time was not optimized to be fast. The spatial resolution of the images is about 1.5 mm with 64 bins along each spatial axis. Figure 3.21A-C shows 2D spatial slices corresponding to the compartment containing

OX63. The spectral coordinate in the 2D slices corresponds to the magnetic field position where the amplitude of the OX63 signal is maximum. Figure 3.22A-C shows 2D spatial slices through the 4D image corresponding to the compartment containing Tempol. Figure 3.22D shows the three segments of the spectral slices corresponding to the Tempol spectrum.

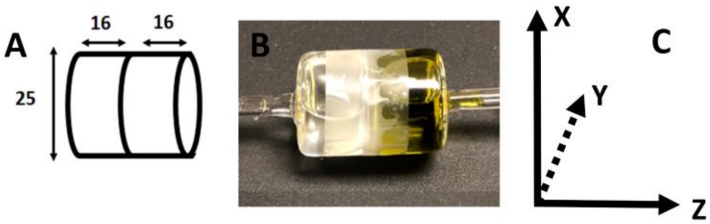

Figure 3.20: 4D imaging phantom. (A) A schematic of the phantom shows OD dimensions in mm. The wall thickness of each tube is about 1.5 mm. (B) Phantom consists of 1 mM Tempol (left) and 0.1 mM OX63 (right). (C) Coordinate system for phantom. The Y axis points into the page. Figure reproduced with permission from Ref. 37.

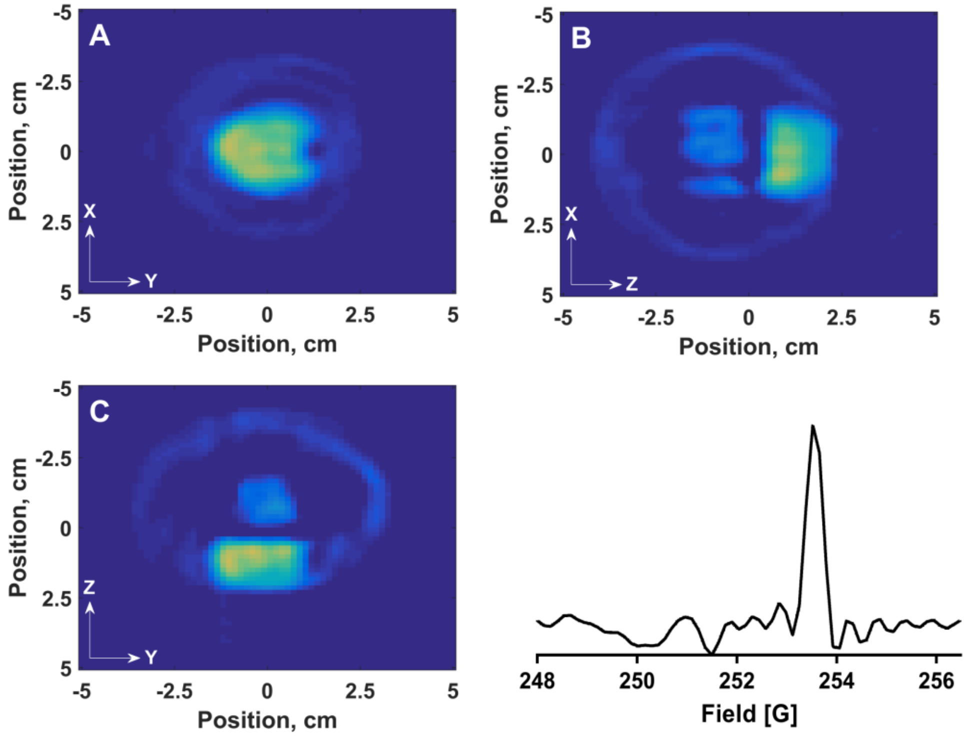

Figure 3.21: 4D image spectral-spatial imaging of 0.1 mM OX63 at 706 MHz. A-C show 2D spatial slices through a 4D image for the spectral region that includes the OX63 and central nitroxide line. (A) shows the intensity in an X-Y slice for fixed Z that is summed for Z = +0.87, +1.03, and +1.19 cm, which is the OX63 compartment. (B) shows the OX63 intensity in an X-Z slice for fixed Y = -0.08 cm. (C) shows the OX63 intensity in a Y-Z slice for fixed X = -0.08 cm. At each position in the 2D spatial slices the intensity corresponds to the intensity at the magnetic field where the amplitude of the OX63 signal is maximum. The OX63 signal is superimposed on the high field wing of the broader nitroxide signal so some intensity is observed for the nitroxide compartments in B and C. (D) shows an OX63 spectral slice at X and Y = -0.08 cm and the sum of Z = = +0.87, +1.03, and +1.19 cm. The X, Y, and Z coordinates are relative to the center (0,0,0) of the image. Figure is reproduced with permission from Ref. 37.

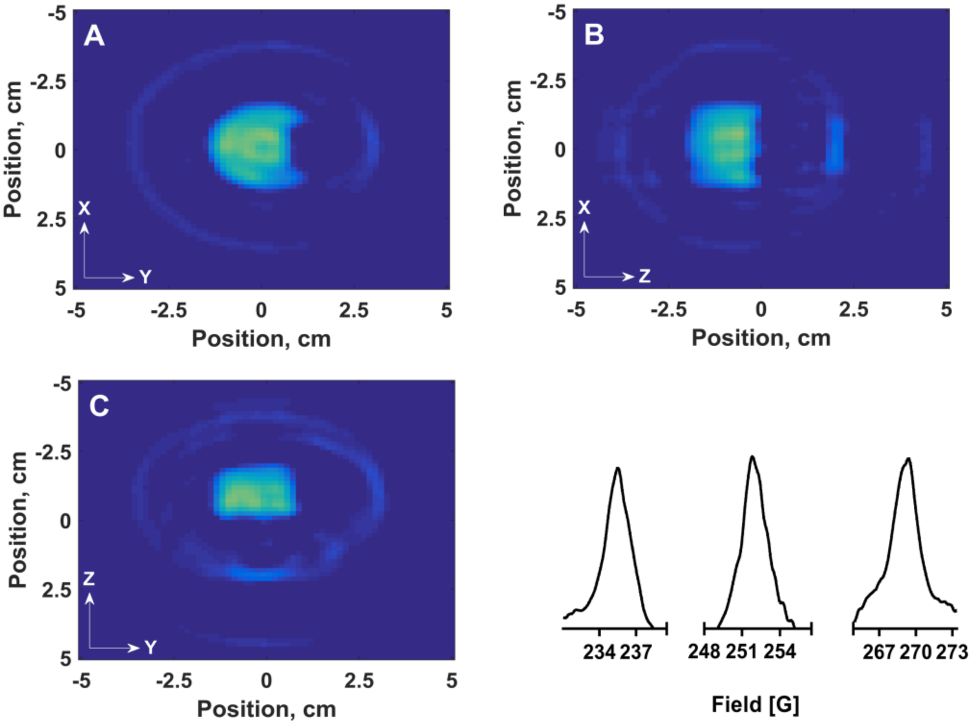

Figure 3.22: 4D spectral spatial-imaging of 1 mM Tempol at 706 MHz. A-C show 2D spatial slices through the 4D image. (A) shows the intensity in an X-Y slice for fixed Z that is summed for -0.87, -0.71, and -0.56 cm, which is the nitroxide compartment. (B) shows the nitroxide intensity in an X-Z slice for fixed Y = -0.08 cm. (C) shows the nitroxide intensity in a Y-Z slice for fixed X = -0.08 cm. At each position in the 2-D spatial slices the intensity is the sum of the nitroxide signals at the 3 magnetic fields where the amplitude is maximum. D shows three segments of the spectral slices, corresponding to the three lines of the nitroxide spectrum, calculated by summing the spectra at X and Y = -0.08 cm and the sum of Z = -0.87, -0.71, and -0.56 cm. The X, Y, and Z coordinates are relative to the center (0,0,0) of the image. Figure is reproduced from Ref. 37.

3.9 700 MHz T_m Measurements of Trityl-CD_3

The 25 mm 700 MHz CLR (Figure 3.4) and the high power (300 W) Tomco amplifier were used to perform high power pulse measurements. An aqueous solution of 0.5 mM trityl-CD_3 (methyl tris(8-carboxy-2,2,6,6-tetramethyl(d3)-benzo[1,2-d:4,5-d0]bis(1,3)dithiol-4-yl)-trisodium salt) was prepared and flame sealed in a cylinder with 25 mm diameter and 25 mm long. The T_m of this sample was measured using a 2-pulse spin echo sequence ($\pi/2 = 200$ ns, $\pi = 400$ ns). Approximately 15.3 W was required to get a 90° turning angle corresponding to the 200 ns $\pi/2$ pulse. The initial spacing, τ, between the pulses was 1.6 μs. Each pulse waveform with a different τ value was generated by the AWG and collected in Xepr as separate transient recordings. The maximum amplitude of each echo was measured in post-processing and plotted as a function of 2τ. The echo decay curve (Figure 3.23) was fit with a single exponential to determine T_m. The average of three measurements was 11.4 ± 0.4 μs. This agrees with previous measurements made at 250 MHz (T_m = 11 μs) and L-band (T_m = 12 μs) for aqueous trityl-CD_3 [53].

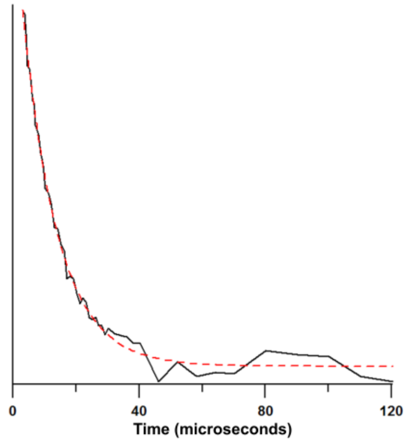

Figure 3.23: Echo decay curve for trityl-CD_3 at 703 MHz. Dashed line is a single exponential fit. T_m =11.1 μs. Figure is reproduced with permission from Ref. 37.

3.10 Summary and Future Directions

The table-top imaging spectrometer was designed for rapid scan and pulse operation between 700 MHz and 1 GHz. The range of frequency was selected to provide adequate signal to noise and maintain imaging penetration depth appropriate for imaging mice. The AWG source provides flexibility in terms of programming over this range of frequencies. Comparison of several RF sources showed that the AWG with GCD programming performs at least as well as other available RF sources. Additionally, four resonators were tested and characterized. The table top magnet requires simple air cooling and is powered by CAEN power supplies in constant current mode. The stability of the main magnet supply was in the range of 1 ppm. Instrument-control python programs were written to integrate the Bruker data acquisition software with the CAEN power supplies to facilitate rapid scan imaging and pulse experiments. Pulse programming was done using Matlab.

To demonstrate the capabilities of the system, rapid scan images were collected at 700 MHz. Image reconstruction above two dimensions is challenging. The Xepr software is not optimized for anything more than two spatial dimensions. The method described by Tseitlin et. al is robust for 2-dimensional spectral spatial imaging but has not yet been extended to more dimensions. The FBP method used for 4D imaging in the Boris Epel software package requires that multiline spectra be reconstructed in pieces and is cumbersome. The applicability to signals that overlap is limited.

Two-pulse echo decay data was collected at 700 MHz for 0.2 mM trityl-CD_3. Currently, the data acquisition software is not optimized to collect pulse data with varying time delays between the pulses. Development of automated data acquisition for pulse experiments is needed to extend the imaging capabilities of the system to pulse imaging.

Chapter 4: New Methods to Measure Electron Spin-Lattice Relaxation

4.1 Introduction

T_1 relaxation is an enthalpic process in which electrons release energy to their environment, and it has important applications for in vivo imaging. In EPR oximetry, molecular collisions between oxygen and a spin probe lead to a faster relaxation rate of the spin probe, which can be quantitatively measured using EPR [54]. To assess local oxygen concentration, it is critical to measure relaxation effects from only oxygen instead of relaxation effects from neighboring spin probes. Low concentrations of spin probe helps reduce unwanted relaxation effects from neighboring spin probes, but the Halpern lab has shown that T_1 is an order of magnitude less sensitive than T_2 (spin-spin relaxation) to these unwanted concentration effects [55]. For this reason, imaging oximetry in the Halpern lab is done by measuring T_1 rather than T_2 as function of space. Although T_1 measurements can be made directly using pulse methods, it is of interest to develop complementary methods that are also capable of measuring T_1 without the use of high power pulses and to consider possible complications from other contributing processes. In this chapter, AWG capabilities are exploited to explore new methods to measure T_1 including rapid scan, frequency stepping, and field jumping.

If there is no unresolved hyperfine and the linewidth is determined by T_2, T_1 can be measured from a continuous wave (CW) power saturation curve. However, when $T_1 \neq T_2$, the relative contributions of T_1 and T_2 to relaxation cannot be separated [56]. If the lineshape is relaxation determined, T_2 can be determined from the linewidth. However, there typically is some inhomogeneous broadening from magnetic field inhomogeneity or unresolved hyperfine so the experimentally observed lineshape is the superposition of many spin packets from which it is difficult to determine T_2. T_1 is conventionally measured by one of two pulse methods. The first method, inversion-recovery monitored by spin echo or free induction decay (FID), uses short microwave pulses to quickly invert the net magnetization as described in Chapter 1. Short pulses are often imperfect due to hardware constraints and have a finite excitation bandwidth which does not uniformly excite wide spectra. To perform inversion recovery, T_m must also be long enough to form an echo after the instrumental dead time that is typically caused by switching transients and finite resonator bandwidth. Pulse power ring down which contributes to instrumental dead time is proportional to resonator Q [57]. Several hundred nanoseconds of instrumental dead time are observed at L-band which limits the samples for which T_1 can be measured with this method.

The second method is saturation recovery (SR), which uses a long saturating pulse to saturate the spin system followed by low power CW microwaves. The Bloch equations predict that the recovery will not purely be T_1 if $T_1 = T_2$ [58, 59] and simulations by George Rinard show that the recovery is very close to the true T_1 if T_2 is much less than T_1. Generally, saturation recovery is used when T_m is too short to observe an echo by conventional pulse methods so this is not a problem. SR is often considered the “gold” standard of T_1 measurement methods because it yields an accurate measurement of T_1 at low B_1 [49]. Accurate measurements of T_1 can be made by SR because the saturating pulse is long enough that any process that moves spins off resonance, such as thermal motion or spin flip transitions, has time to equilibrate the saturated spins with the non-saturated spins by transfer of magnetization through neighboring spin packets. Collectively, these processes that move spins off resonance are referred to as spectral diffusion. To allow for spectral diffusion to occur, the length of the saturating pulse is typically 5 times the expected $T_{1.}$ However, SR is known for low signal to noise because of the low power continuous waves that are used for observation of the recovery. The signal to noise is lower than that which would be obtained with conventional CW because field modulation and a lock-in detector are not used.

Development and results of three new methods to measure T_1 will be presented: rapid scan, frequency stepping and field jumping. The work presented in this chapter was carried out in collaboration with Dr. George Rinard who calculated rapid scan simulations using numerical analysis of the Bloch equations [14] and solved the Bloch equations for special cases in which spin lattice relaxation (T_1) can be found analytically. The solutions for when $\Delta\omega \neq 0$ and B_1 is constant served as the motivation for the field jump and frequency step experiments described in this chapter. The relaxation times measured by these new methods are compared to those measured with conventional methods.

4.2 Resonators and Samples

Three resonators made by George Rinard were used for the experiments described below. One is a 5 mm 1.09 GHz rapid scan CLR similar in design to the 16 mm CLR described in Ref. 33. The second is a 5 mm copper CLR designed for pulse measurements that is similar in design to the resonator described in Ref. 50. The third is a 1.5 GHz 4 mm reflection resonator that is described in Ref. 30.

The 5 mm 1.09 GHz rapid scan CLR (Q = 100) has a resonator efficiency of about 0.1 $G/\sqrt{W}$. The efficiency was calculated by comparing the saturation points on two continuous wave power saturation curves of coal, one measured with a Bruker SHQ resonator (4122SHQ-W1/0913) that had a known efficiency of 2 $G/\sqrt{W}$, and the other measured with the 1.09 GHz rapid scan CLR.

The resonator efficiency of the 5 mm copper resonator was calculated by measuring the power level corresponding to a 90° turning angle for a 500 ns pulse with an aqueous sample of trityl-CD_3 in the resonator. The B_1 needed for a 500 ns pulse can be calculated using equation 4.1.

$$\text{flip angle} = \gamma B_1 t_p \qquad \text{eq. 4.1}$$

Where γ= electron gyromagnetic ratio, and t_p is the pulse length. The calculated resonator efficiency when critically coupled was between 1.04 and 1.2 $G/\sqrt{W}$. An average value of 1.1 $G/\sqrt{W}$ was used to convert power to B_1 in the following experiments.

The efficiency of the 4 mm reflection resonator is 3.9 $G\sqrt{W}$ [30]. It was used for a few spin echo experiments for which B_1 values are not reported.

Samples

Samples include solutions of two trityl radicals that were gifts from Prof. Howard Halpern (University of Chicago). Two of the trityl solutions contained 0.2 mM deuterated Finland trityl (trityl-CD_3), one in a mixture of 1:1 in water:glycerol and the other in distilled water. The solutions were bubbled with N_2 and flame sealed in 4 and 5 mm outer diameter

(OD) tubes, respectively. The third and fourth solutions contained 0.2 mM trityl OX63, which has slightly broader lines than trityl-CD_3 [53]. One solution of OX63 was aqueous and the other prepared as described in [60] with 0.9% weight/volume of NaCl. The aqueous OX63 sample was put in Teflon tubing (0.91 mm inner diameter) and placed in a 4 mm OD tube that was briefly purged with N_2 before flame sealing. The linewidths of these trityl samples are much less than a gauss (Figure 4.1). Three solid state samples were studied. A glassy solution of nitroxide (^{14}N) immobilized in a polyvinyl borate glass [61] was in a 4 OD mm tube. A powdered coal sample (Eaton lab, #16) was in a 4 mm OD tube open to the air. The coal was purchased from a local retailer and labeled “fire place coal”. Lastly, a fused quartz sample (Eaton lab, #55) that had been irradiated at 24 MRad using Co-60 gamma was contained in a 4 mm OD tube, open to air. Rapid scan spectra of solid state samples are shown in Figure 4.2.

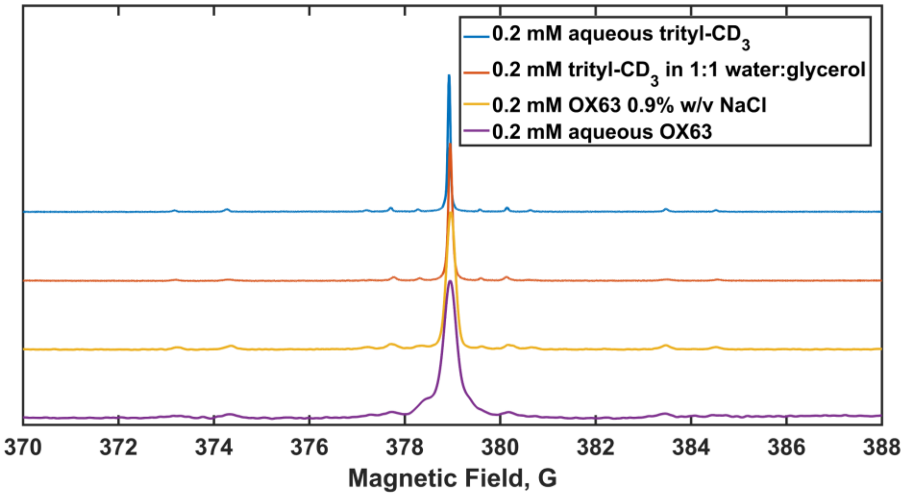

Figure 4.1: Rapid scan spectra of aqueous triarylmethyl samples at 1.09 GHz. Scan frequency = 5.376 kHz, sweep width = 18 G.

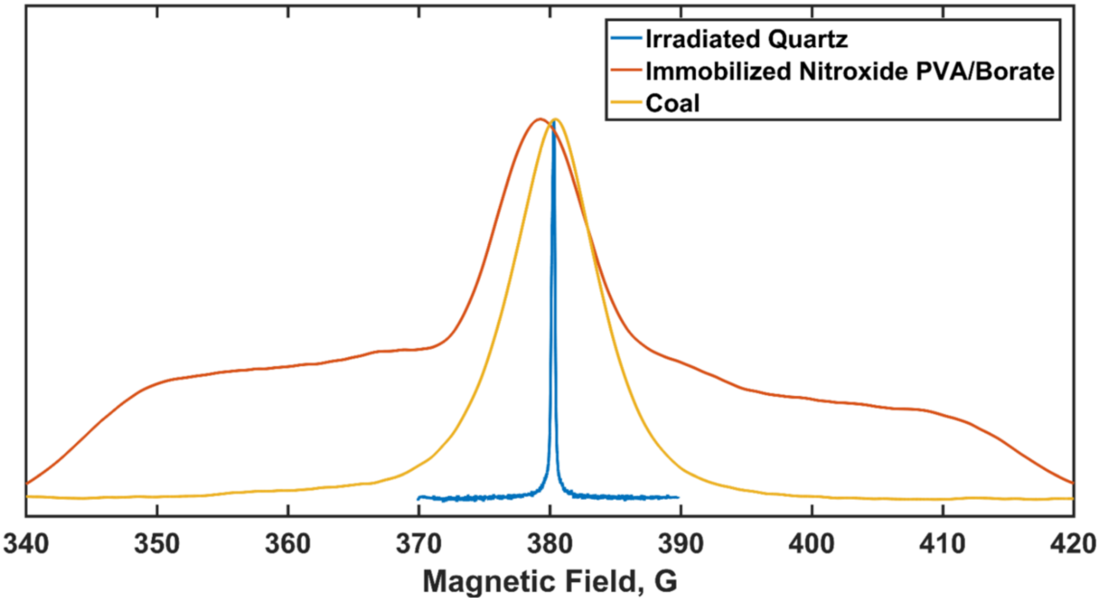

Figure 4.2: Rapid scan spectra of solid state samples at 1.09 GHz. Scan frequency = 5.376 kHz.

4.3 Rapid Scan T_1 Method

It was shown previously that electron spin-spin relaxation (T_2) can be measured by simulation of the rapid scan transient response when rapid scan oscillations are detected [62, 63]. However, there is not an analogous method to measure T_1. Adiabatic passage has been used in magnetic resonance as a method to measure T_1 [64]. Adiabatic trapezoidal field scans have been used in NMR to measure T_1 [65]. One paper describes an EPR spectrometer and technique in which fast adiabatic frequency passage is used to measure T_1 [66]. The rapid field scans described here are not fast enough to achieve adiabatic passage.

In this new method to measure T_1 with rapid scan, an EPR signal is first saturated by applying a constant B_1 on resonance. The magnetic field is then swept through resonance at a rate that is fast compared to electron relaxation.

Rapid scan experiments were performed at L-band using either the water cooled magnet described in [50] or the iron-core magnet described in [44]. The 700 MHz to 1 GHz AWG and bridge described in chapter 3 were used to generate the RF. The rapid scan coil driver (RSCD) described in [34] and 5 mm 1.09 GHz rapid scan CLR were used for rapid scan T_1 measurements. Rapid scan EPR is usually performed using either sinusoidal or triangular scans, driven by the RSCD [67]. In this new method to measure T_1 with rapid scan, the waveforms shown in Figure 4.3 used. They were calculated in Matlab, generated by the AWG and sent to the RSCD via RS232. The scan waveform can be split into two sections. The first half, called the saturation period, lasts for at least $5T_1$s during which the current output of the RSCD is zero. A small DC offset was observed in the RSCD such that the current was not exactly zero but a small value, offsetting the position of saturation in the spectrum. This can be corrected for by offsetting B_0 the appropriate amount to ensure saturation is at the desired place in the spectrum. This was particularly important for narrow trityl samples. During the saturation period of the waveform, the field (B_0) and frequency (ω_0) are set at resonance for a particular EPR transition. In the second half of the scan waveform, the magnetic field is rapidly swept back and forth through the signal of interest using the waveform shown in Figure 4.3A or B. The waveform in Figure 4.3A was programmed to have a linear scan rate of 1.55 MG/s through resonance and the time spent off resonance was one tenth of the expected T_1.

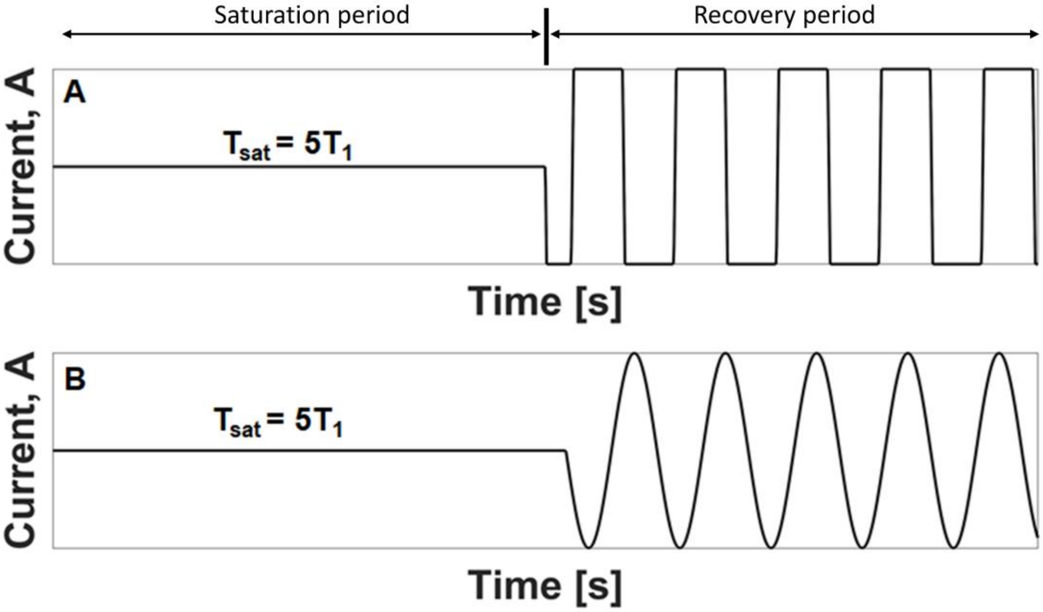

Figure 4.3: Generic rapid scan waveforms used to measure T_1. The experiment is divided into two parts, the saturation period and recovery period. (A) linear waveform (B) sinusoidal waveform.

A constant B_1 is applied throughout the experiment and each pass through resonance is fast compared to electron relaxation. The majority of time during the recovery period is spent off resonance. Since the RF power level is unchanged between the saturation and recovery periods, there are no switching transients, so theoretically there is no instrumental dead time following the saturation period as there is in conventional pulse methods. This permits detection immediately following the saturation period, with the limiting variable being scan frequency. Each time resonance is swept through, a signal is detected. At the beginning of the scans, the signal amplitude is attenuated because the spin system is still partially saturated. As the spin states return to equilibrium, the signal intensity increases. To measure a T_1 time constant, only the peaks of the rapid scan signals are selected and fit with an exponential. Before measuring the peaks of the rapid scan data, a background spectrum was subtracted from the data.

In some data, the relative peak intensities when scanning up field were systematically different in amplitude than when scanning down field. The observation did not depend on the sample and has been observed not only for rapid scan T_1 data, but in rapid scan data in general. It may be the result of imperfect resonator tuning. The intensity of a rapid scan signal is dependent on the position of rapid scan frequencies relative to the resonator dip. If the microwave frequency is not matched to the center of the resonator dip, the asymmetry of the resonator dip could cause up field scans to have different intensities than down field scans.

Scan Coils

The rapid scan coils on the 1.09 GHz 5 mm rapid scan CLR can be interchanged. Ideally the coils should have a low inductance (< 1 mH) so that the scan direction can be changed quickly. The rate at which the scan current can change directions also depends on the slew rate of the power amplifiers built into the RSCD. The current slew rate is 144 V/µs. Early experiments used scan coils with a relatively high inductance (1.6 mH, 40.5 G/A) and the waveform shown in Figure 4.3A. It was later found that the actual rate was less than the programmed rate primarily due to the slew rate of the power amplifiers in the RSCD. The RSCD produces the waveform shown in Figure 4.3A when operating in a non-resonated mode. The slew rate of the power amplifiers in the RSCD placed an upper limit of 250 kG/s that could be achieved using this waveform in non-resonated mode. The scan rate limits the number of points that can be collected to construct the exponential curve from which the fit is T_1.

An earlier version of the RSCD called ‘RCD 2 A/B’ has a “burst mode” function. In this mode, a sinusoidal scan was generated with a 50% duty cycle. For example, if the total repetition time is 400 μs and the rapid scan frequency is 75 kHz, the RSCD generates 15 cycles in 200 μs. During the remaining 200 μs, the current output of the RSCD is zero. A generic waveform of this type is shown in Figure 4.3B. This type of waveform can be generated in a resonated mode where the scan rate is determined by equation 4.2.

$$\text{scan rate} = \pi * \text{sf} * SW \qquad \text{eq. 4.2}$$

According to equation 4.2, the maximum scan rate is now determined by the maximum scan frequency (sf) and sweep width (SW) that RCD 2 A/B can achieve in resonated mode. The sweep width is the scan current times the coil constant of the rapid scan coils. The maximum current the RCD 2B can output is approximately 6 A. The maximum scan frequency is approximately 130 kHz. Faster scan frequencies allow more data points to be collected during the T_1 recovery which define the exponential better. Faster scan rates also permit higher powers to be used because the amount of time spent on resonance during each pass through resonance is decreased. The inductance of the rapid scan coils also affects how well RCD 2 A/B works because it determines how quickly the transition can be made between “on” and “off” in burst mode. It is ideal to have a sharp transition from “off” to “on” so that data collection can begin immediately. For this reason, coils with an inductance of 8 μH (1.4 G/A) were used in some experiments in which RCD

2 A/B was used in burst mode. A third set of coils with an intermediate inductance of 0.5 mH (25 G/A) was also used in some experiments. The tradeoff of using low inductance coils is that the coil constant also decreases, which lowers the maximum sweep width that can be achieved. For samples with a narrow linewidth like trityl-CD_3, this is not a problem. For samples with wide signals, coils with a higher inductance and thus larger coil constant were used.

4.4 Rapid Scan T_1 Results

Irradiated Fused Quartz

The T_1 of the $E^{'}$ center in irradiated quartz measured with conventional saturation recovery is approximately 200 μs at room temperature. At X-band where the g anisotropy is more defined and the linewidth of quartz is 4-5 G, T_1 varies with field position. At L-band, the linewidth of quartz is approximately 350 mG and T_1 does not have a significant field dependence [68].

In the rapid scan T_1 experiments, the scan frequency and sweep width were 12 kHz and 5.8 G, respectively, using the scan waveform shown in Figure 4.3A. Power was applied at the center of the resonator dip (1.09 GHz CLR). Data collected at an intermediate power, approximately 0.9 mW (B_1 = 3 mG), are shown in Figure 4.4A. The peaks of the rapid scan signals were measured and plotted vs. time, as shown in Figure 4.4B. The data were fit to a single exponential with T_1 = 204 μs. The peak of the first rapid scan signal was not used in the calculation of the exponential fit because it occurs as the field is moved away from resonance and is offset from the rest of the rapid scan signals.

The spin-lattice relaxation time of quartz was measured with rapid scan as a function of power. The average of two measurements is shown in Figure 4.5. The measured $1/T_1$ increased with increasing power ranging from about 0.0044 to 0.0065 μs^{-1} which corresponds to a T_1 of 230 (0.1 mW, B_1 = 1 mG) at low power to 150 μs (5 mW, B_1 = 7 mG) at high power. T_1 measurements at low power are likely the limiting T_1 value [69].

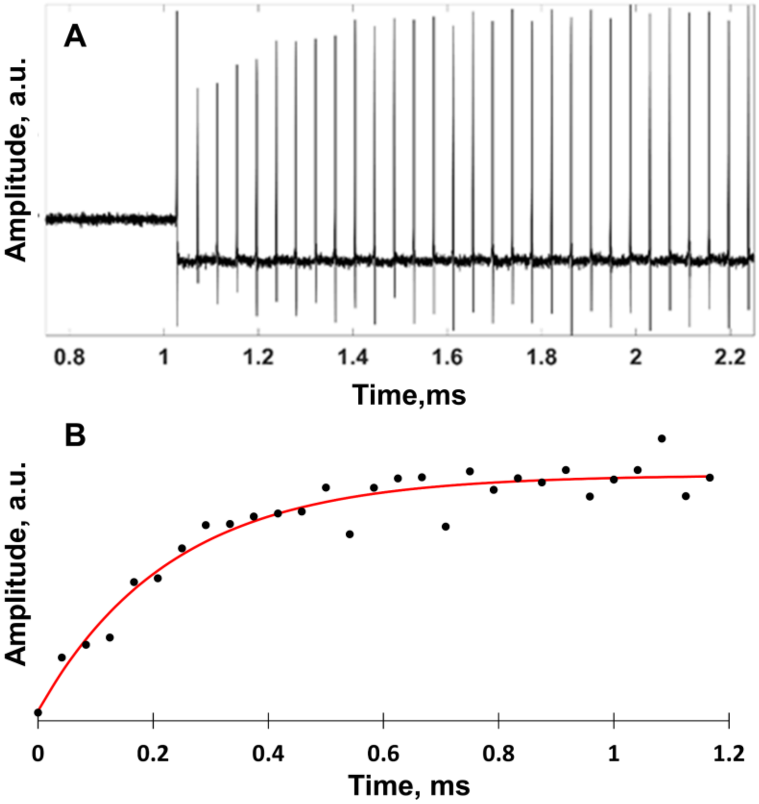

Figure 4.4: (A) Rapid scan T_1 data for irradiated quartz at 1.09 GHz. Scan frequency = 12 kHz, sweep width = 5.8 G, scan rate = 250 kG/s. B_1 = 3 mG. A 3-point smooth was applied to the rapid scan data before measuring peak amplitudes. (B) Amplitude of rapid scan signal peaks (black) and exponential fit (red). T_1 = 204 μs.

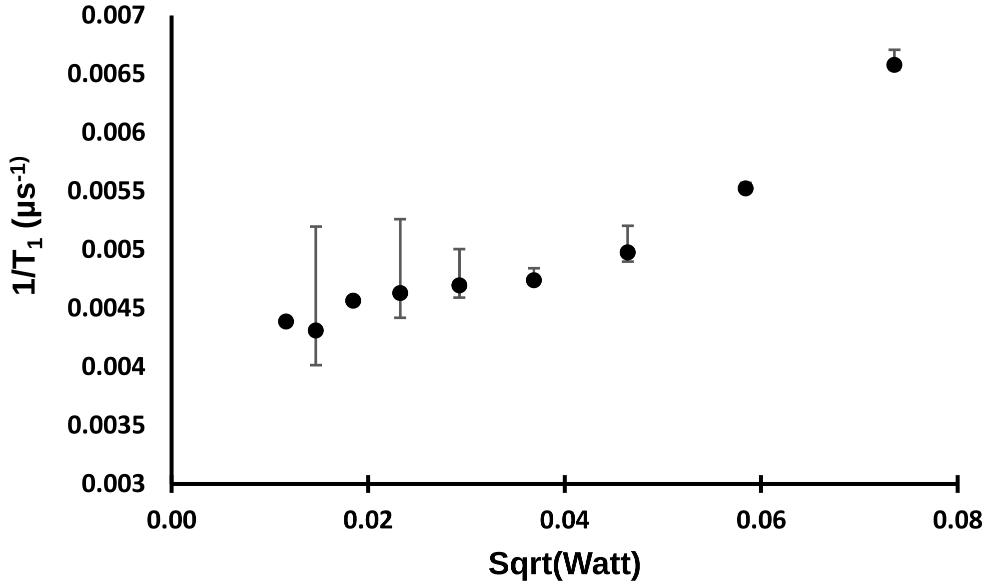

Figure 4.5: $1/T_1$ of irradiated quartz vs. power at 1.09 GHz measured with rapid scan. Uncertainties are calculated as the average deviation of two replicate measurements.

Trityl-CD$_3$ in 1:1 water:glycerol

T_1 and T_m were measured for this deoxygenated sample by spin echo at 973 MHz using a 5 mm copper CLR designed for pulse experiments and the spectrometer described in [44]. The π/2 pulse length was 300 ns and the π pulse length was 600 ns. Power was optimized for maximum echo amplitude. The measured T_1 and T_m were 16.1 ± 0.2 µs and 3 ± 0.1 µs, respectively.

Rapid scan T_1 data were collected at powers ranging 1 to 3 mW (B_1 = 3-6 mG) using the scan wave form shown in Figure 4.3A and the 5 mm 1.09 GHz CLR. The scan frequency was 75 kHz and the rapid scan sweep width was approximately 2.5 G. A faster $1/T_1$ was observed at high observe power compared to low power (Figure 4.6) similar to what was observed for irradiated quartz (Figure 4.5). The average T_1 at relatively low power (1 to 2 mW) is 16.4 ± 1.2 µs. Data collected at 2 mW (B_1 = 4 mG) are presented in

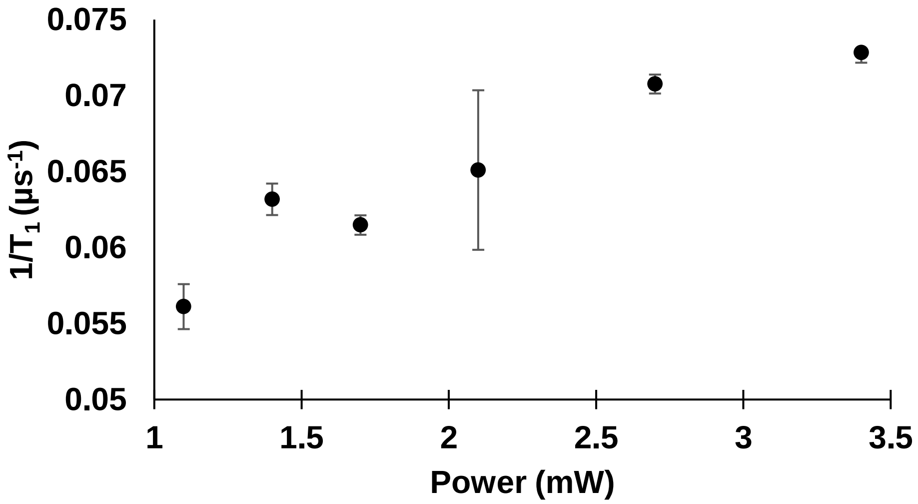

Figure 4.6: T_1 of trityl-CD$_3$ in 1:1 water:glycerol vs. power at 1.09 GHz measured with rapid scan. Uncertainties were calculated as the standard deviation of at least three measurements.

Figure 4.7A and the corresponding peak heights are shown in Figure 4.7B. A three-point smooth was applied to the rapid scan data before measuring the peak amplitudes. The first rapid scan signal was not used in the calculation of the exponential.

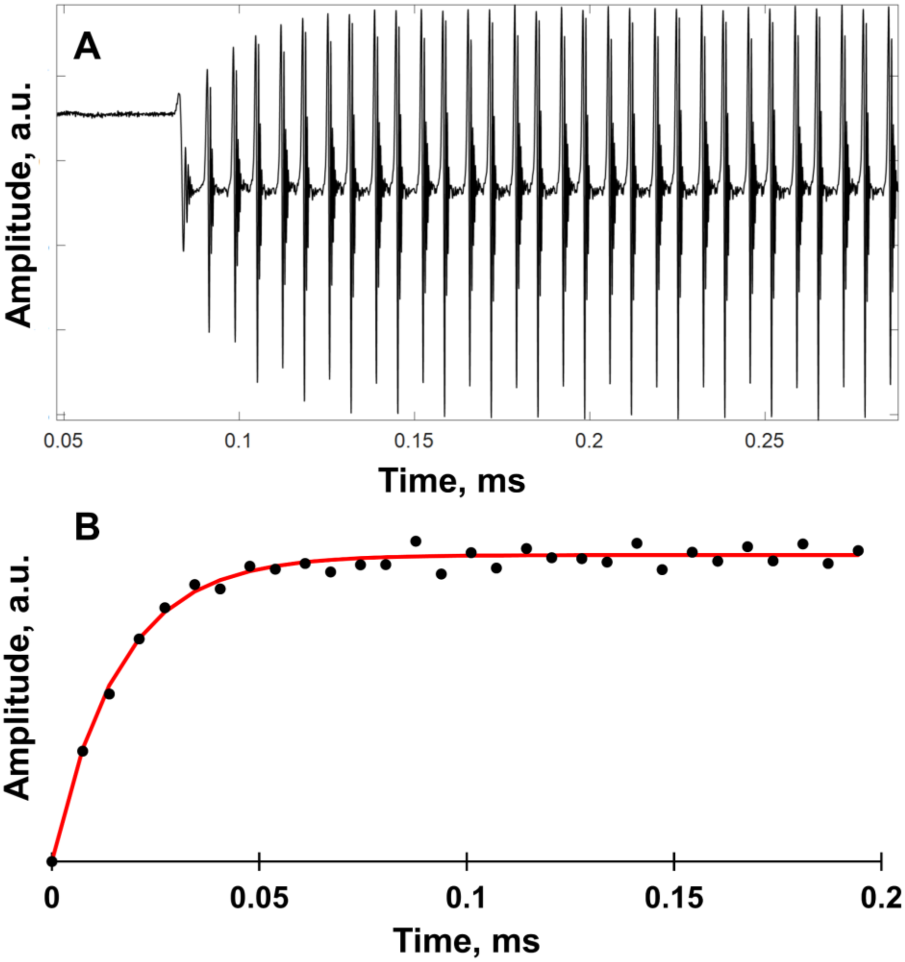

Figure 4.7: (A) Rapid scan T_1 data for trityl-CD_3 in 1:1 water:glycerol at 1.09 GHz. B_1 = 4.1 mG, scan frequency = 75 kHz, sweep width = 2.5 G, scan rate = 250 kG/s. A 3-point smooth was applied to rapid scan data before measuring peak amplitudes. (B) Amplitude of rapid scan signal peaks (black) and exponential fit (red). T_1 = 16.2 µs.

Aqueous Trityl-CD_3

T_1 and T_m were measured by spin echo at 1.5 GHz using a 4 mm reflection resonator and the spectrometer described in [44]. The π and π/2 pulse lengths were 80 and 160 ns, respectively. Power was optimized for maximum echo amplitude. Average values of T_1 = 12.7 ± 0.1 μs and T_m = 8.4 ± 0.1 μs were measured.

Rapid scan measurements used frequencies that were between 70 and 72 kHz and the sweep width ranged from 1 to 1.5 G. The rapid scan waveform shown in Figure 4.3B was used. An average T_1 = 14 ± 2 μs was measured using powers ranging from 0.5 to 11

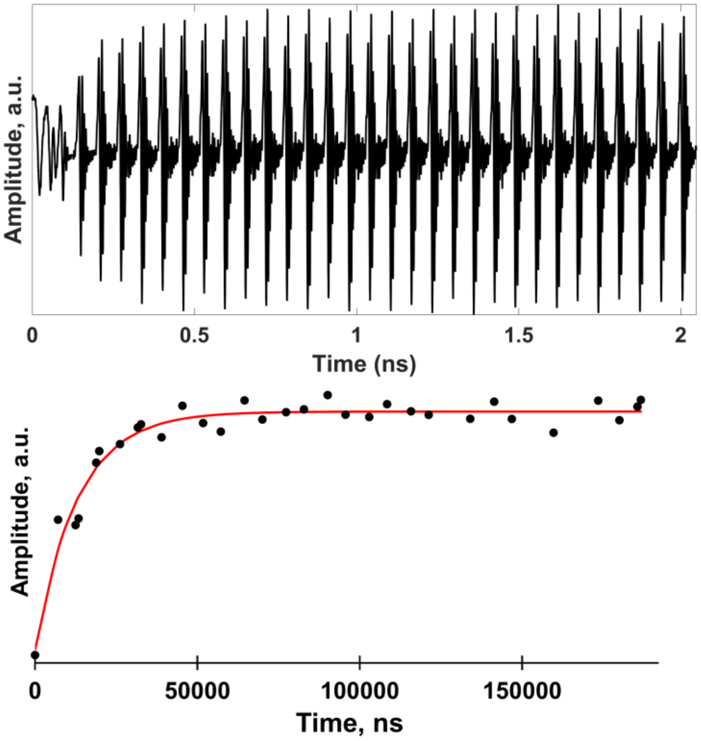

Figure 4.8: (A) Rapid scan T_1 data for aqueous trityl-CD_3 at 1.09 GHz. B_1 = 5 mG, scan frequency = 78 kHz, sweep width = 1.5 G. (B) Amplitude of rapid scan signal peaks (black) and exponential fit (red). T_1 = 13.3 μs.

mW (B_1 = 2-10 mG). A three-point smooth was applied to the rapid scan data before measuring the peak amplitudes. The first rapid scan signal was distorted and not used in the calculation of the exponential. Data collected at B_1 = 5 mG are shown in Figure 4.8.

Coal

Coal is a heterogenous sample with a carbon-based radical exhibiting an unresolved spectrum approximately 8 G wide measured at full width half maximum (FWHM). Conventional saturation recovery was performed at 980 MHz using a 5 mm copper CLR designed for pulse experiments. Experiments were performed on the spectrometer described in [44]. The pump time was 200 μs and a low observe power was used that did not shorten the measured T_1. An average T_1 = 18.6 ± 0.9 μs was calculated using a single exponential fit to the recovery curve. Multiple studies in the Eaton lab indicate that data for coal are typically fit best with a biexponential when the signal to noise is high enough. Because of the low signal to noise and few points available to define an exponential for the rapid scan experiments, a single exponential was used for fitting both the rapid scan and saturation recovery data.

Rapid scan measurements were made using the waveform in Figure 4.3B. Scan frequencies were between 77 and 114 kHz and sweep widths of 40 G were used. The first rapid scan signal was not used in the calculation of the exponential. For powers between 6 and 11 mW (B_1 = 8-10 mG), an average T_1 value of 15.2 ± 2.2 μs was measured. Data collected with $B_1 \sim 9.3$ mG is shown in Figure 4.9.

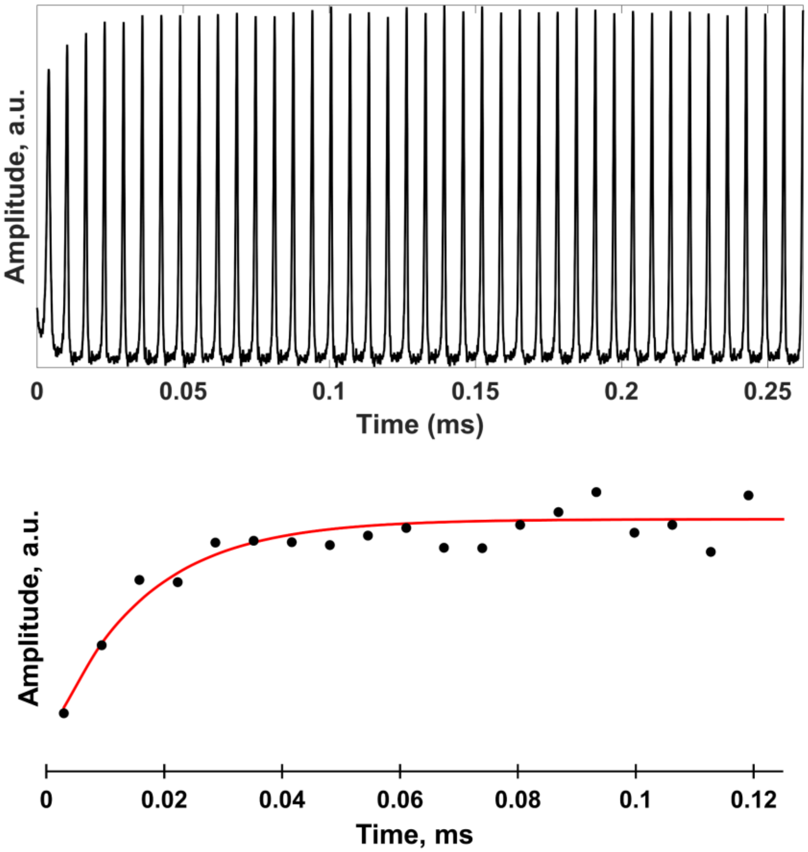

Figure 4.9: (A) Rapid scan T_1 data for coal at 1.09 GHz. Power = 8.6 mW, scan frequency = 77.4 kHz, sweep width = 40 G B_1 = 9.3 mG. (B) Amplitude of rapid scan signal peaks (black) and exponential fit (red). T_1 = 15.4 µs.

4.5 Rapid Scan T_1 Summary

Relaxation times measured with conventional methods are compared with results with rapid scan experiments for four samples: irradiated quartz, trityl-CD_3 in 1:1 water:glycerol, aqueous trityl-CD_3, and coal. These samples were chosen to provide both aqueous and non-aqueous samples with a strong signal and a T_1 that is relatively long. A summary of the results is shown in Table 4.1. The uncertainties reported are the standard deviation of at least three measurements. Reasonable agreement is obtained between the different methods.

A single exponential fit was used to analyze the data obtained in saturation recovery, inversion recovery, and rapid scan experiments. The first rapid scan signal was not used in the calculation of exponential curves to measure T_1 because in some cases, the first signal was distorted or offset from the other rapid scan signals. This occurs as the field is moved away from resonance and the waveform does not represent a complete sweep through resonance.

Table 4.1: T_1 measured with rapid scan and conventional methods. A single exponential fit was used to analyze recovery curves.

	T_1 (Rapid Scan)	**T_1 (Inversion Recovery or Saturation Recovery)**
Trityl-CD_3 (water)	^{b}14 ± 2 μs	12.7 ± 0.1 μs
Coal	^{b}15.2 ± 2.2 μs	18.6 ± 0.9 μs
Trityl-CD_3 in 1:1 water:glycerol	^{a}16.4 ± 1.2 μs	16.1 ± 0.2 μs
Irradiated quartz	^{a}150-230 μs	200 μs*

[a] Measured with a linear wave form.
[b] Measured with a sinusoidal wave form.
*Ref. 68

A greater uncertainty is associated with the rapid scan measurements because of the limited number of points that are available to define an exponential compared to the conventional method. In addition, up-field scans and down-field scans were sometimes observed to have unequal signal intensities independent of the saturation level which increased the noise level in the exponential curves. For rapid scan T_1 measurements of quartz and trityl-CD_3 1:1 in water:glycerol, a shorter T_1 was measured at high power relative to low power measurements. This is a well-known phenomenon in conventional saturation recovery [69] and is expected to also be present in rapid scan measurements.

The current implementation of the rapid scan method to measure T_1 has constraints. In rapid scan experiments, the power level is held constant and there are no switching transients to delay the measurement of T_1 like there are in pulse experiments. This was the initial rationale for testing this method. However, that advantage is offset by the distortion of the rapid scan signal until at least a half cycle after the saturation period. In addition, for the rapid scan method with current scan rates a small number of points is available to define an exponential recovery leading to a greater uncertainty and error associated with the measurement. The current hardware of the rapid scan coil driver is not designed for scan frequencies greater than 130 kHz. The magnetic field scan rates that were used did not achieve adiabatic passage. For rapidly relaxing samples (T_1 <10 μs) it is not feasible to use rapid scan to measure T_1 using rapid scan with the current method implementation. Obtaining higher scan frequencies would improve this method, allowing for more rapid scan signals to be collected in a shorter time.

4.6 Frequency Stepped Method

The recent availability of high frequency AWGs that produce the microwave frequencies needed for EPR have opened up opportunities for new experiments to be performed. Using an AWG, microwave frequency, amplitude and phase can be digitally changed with nanosecond resolution. In the experiments described below, the AWG is utilized to make fast frequency step from on resonance to off resonance. Here, resonance is defined as the position in a spectrum where the signal intensity is at a maximum. Off resonance is defined as in the wings of a spectrum. Different spin packets are measured in the wings of an inhomogeneously broadened spectrum relative to on resonance. The 700 MHz to 1 GHz AWG and bridge described in Chapter 3 were used to generate the RF and experiments were performed using either the water cooled magnet described in [50] or the iron-core magnet described in [44]. Waveforms calculated in Matlab were used to drive the AWG. To measure T_1, a background data set was subtracted from each recovery curve and the corrected recovery was then fit with an exponential.

Analytical solutions to the Bloch equations when $\Delta\omega \neq 0$ and B_1 is constant predict that T_1 could be measured with a constant B_1 by saturating spin packets at one position in the spectrum and then stepping to a region of the spectrum where the level of saturation is less and monitoring the recovery. Both absorption and dispersion recover at the same rate. The full equation for saturated lineshape is given by equation 4.3 [70]:

$$s = \frac{T_2}{1 + T_2^2(\omega_0 - \omega)^2 + \gamma^2 B_1^2 T_1 T_2} \quad \text{eq. 4.3}$$

The term in the denominator, $\Delta\omega$, indicates that at positions offset from resonance, the saturation (s) is less than when $\Delta\omega = 0$. To test this, the signal amplitude as a function of power was measured at two positions in the signal of trityl-CD$_3$ in 7.5 mM NiCl$_2$ at X-band. The excess NiCl$_2$ broadened the trityl-CD$_3$ signal to about 6 G peak-to-peak which allowed separate measurements of signal amplitude at 3508 and 3518 G. X-band spectra were collected from 0.21 mW to 50.5 mW (Figure 4.10A). The amplitude at the two positions were measured at each power. The signal located at 3518 G saturated at around 20 mW, while the signal located at 3508 did not saturate at the powers used (Figure 4.10B). This is evidence that the level of saturation varies with offset from resonance.

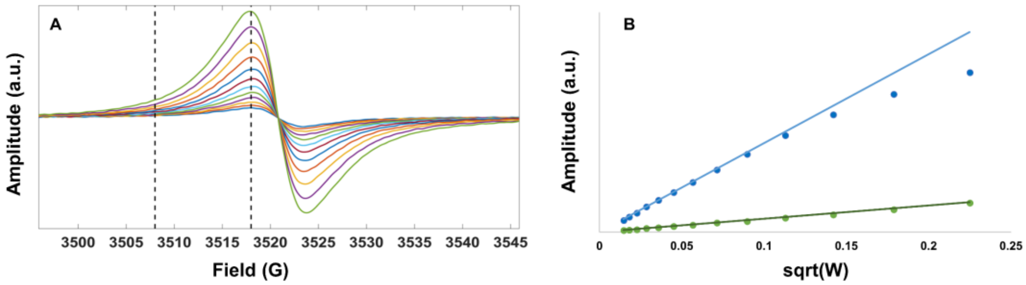

Figure 4.10: (A) X-band CW spectra of trityl-CD$_3$ in 7.5 mM NiCl$_2$ at varying power levels. Dashed lines located at 3508 and 3518 G represent the positions in the signal that power saturation curves were constructed. (B) Signal amplitude at 3508 G (green data points) and 3518 G (blue data points). The solid lines are linear extrapolations from low power data points.

In frequency stepped experiments, the initial field and frequency are selected to saturate the center of an EPR signal. After a period of 5 times the expected T_1, the frequency is offset from the center of the signal while the field is held constant. The spins that were initially saturated are free to relax and their recovery from saturation is monitored with CW microwaves at the stepped frequency. The present model assumes that the same spins that were initially saturated are observed at the stepped frequency. Similar to how spectral diffusion processes can take spins off resonance, transfer of saturation may occur through spin packets from the initial frequency to the stepped frequency. In theory, this technique is similar to pulse electron-electron double resonance (ELDOR) [71], although the steps in ELDOR may intentionally be large to probe spectral diffusion to other hyperfine manifolds.

Resonator Tuning

The 980 MHz 5 mm CLR designed for pulse experiments was used for frequency stepped experiments. The two resonators of the CLR (excitation and detection) can be tuned to the same frequency (Figure 4.11A) or to separate frequencies (Figure 4.11B and Figure 4.11C). There are advantages and disadvantages to each tuning scheme.

When the excitation and detection resonators are tuned to the same frequency as shown in Figure 4.11A (tuning scheme A), the initial (ω_1) and stepped frequency (ω_2) can

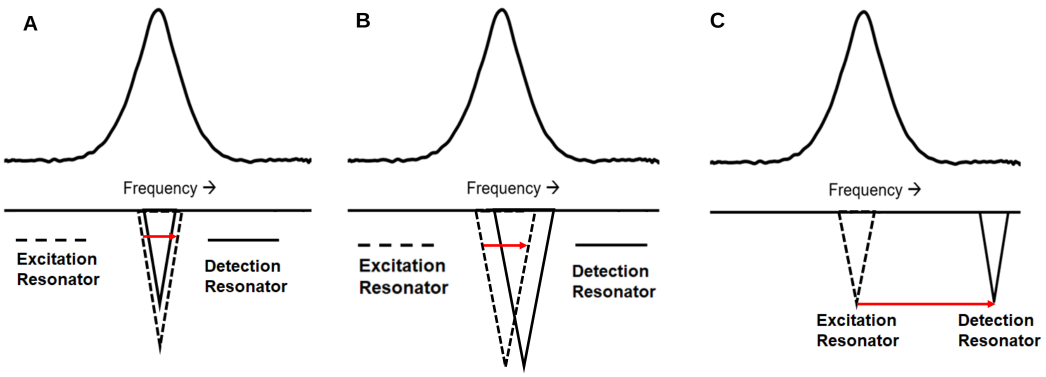

Figure 4.11 Tuning schematic for the frequency step experiment. The resonators are shown relative to a coal spectrum. The red arrows correspond to the frequency step, $\Delta\omega$, for each tuning scheme. (A) Tuning scheme A: the excitation resonator (dashed line) and detection resonator (solid line) are tuned to the same frequency. The frequency is stepped anywhere within the excitation resonator bandwidth. (B) Tuning scheme B: The detection resonator (solid line) is tuned to the stepped frequency, ω_2. The frequency is stepped anywhere within the excitation resonator bandwidth. (C) Tuning scheme C: the excitation resonator and detection resonator are tuned to separate frequencies separated by $\Delta\omega$. The frequency is stepped from the center of the excitation resonator to the center of the detection resonator.

be anywhere within the resonator bandwidth. If the excitation and detection frequencies are selected such that they are at equivalent positions in the resonator dip, the reflected power is constant when the frequency is stepped and thus the resonator efficiency and B_1 remain constant throughout the experiment. The size of the frequency step is limited by the excitation resonator bandwidth which is about 3 MHz when critically coupled. This limits the types of samples that can be studied to narrow line samples. Also, when the frequency is stepped within the resonator bandwidth, a transient reflection is observed due to the phase transition of the waveform being detected as a discontinuity of the RF. The isolation between the resonators helps to protect the detection system from this transient response but does not eliminate it. The detector blanking switch (B1 in Figure 3.3) can be utilized to protect the digitizer from the transient reflection.

Figure 4.11B shows tuning scheme B in which the initial (ω_1) and stepped (ω_2) frequency are still within the bandwidth of the excitation resonator and at equivalent positions relative to the resonator dip. However, the detection resonator is tuned to the stepped frequency, ω_2. The resonators were tuned in this configuration to increase the detection resonator sensitivity at ω_2. This does not change the limitation on the width of the frequency step imposed by the bandwidth of the excitation resonator. Over-coupling the excitation resonator can increase the bandwidth. However, that decreases the resonator efficiency.

When the resonators are tuned to frequencies far apart as shown in Figure 4.11C (tuning scheme C), higher isolation is achieved between the excitation and detection resonators than with tuning schemes A or B. The frequency is stepped from the center of the excitation resonator to the center of the detection resonator, where resonator efficiency is greatest. However, the excitation resonator response to ω_2 is poor because more power is reflected out of the excitation resonator at that position in the resonator dip. Thus, B_1 is unintentionally lowered when the frequency is stepped from ω_1 to ω_2. Even so, better results were obtainable with tuning scheme C than with tuning schemes A and B (Figure 4.11A and B). The increased isolation and elimination of resonator bandwidth constraint outweighed the effect of a less efficient power delivery during the detection period. The 0.2 mM aqueous trityl-CD_3 sample was used to test tuning schemes A and B. A variety of samples were used to test tuning scheme C.

4.6 Frequency Stepped Results

Tuning Scheme A

The 0.2 mM aqueous trityl-CD_3 sample was studied using tuning scheme A because it has a narrow and strong signal. The frequency step for the results presented below was 2.4 MHz. The frequencies, ω_1 = 980.1 MHz and ω_2 = 982.5 MHz, were at equivalent positions in the resonator dip. The transient response to stepping the frequency within the resonator bandwidth required that the detector be blanked during the frequency step. T_1 was measured from B_1 = 3 mG to B_1 = 14 mG, shown in Figure 4.12. T_1 did not vary significantly with increasing RF power. The average value of these measurements is T_1= 12.3 ± 0.6 µs. The T_1 of this sample measured by spin echo at 1.5 GHz using the 4 mm reflection resonator was 12.7 ± 0.1 µs, which is in good agreement with the frequency stepped results.

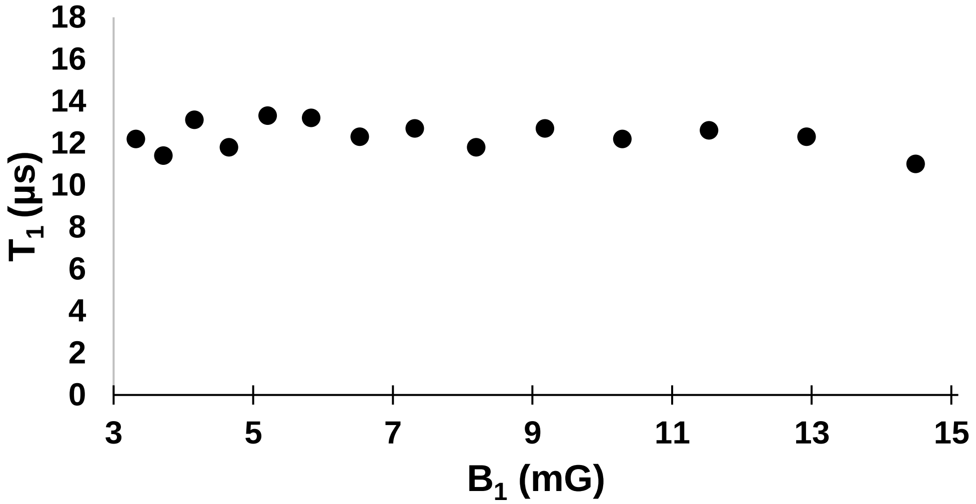

Figure 4.12: T_1 of 0.2 mM aqueous trityl-CD_3 vs. B_1 collected with frequency step experiment. Relaxation times were measured by frequency stepping using tuning scheme A.

Tuning Scheme B

The same 0.2 mM aqueous trityl-CD_3 sample was also studied using the tuning scheme shown in Figure 4.11B. The excitation resonator was overcoupled and tuned to ω_1 = 974.64 MHz. The detection resonator remained critically coupled and was tuned to the stepped frequency, ω_2 = 981.23 MHz. The frequency step was 6.6 MHz wide. The detector was blanked during the frequency step. Results obtained with these parameters are compared to a recovery curve collected with tuning scheme A and a 2.4 MHz wide frequency step. Both were collected at B_1 = 12 mG. Signal to noise was calculated as the maximum amplitude minus the minimum amplitude of the recovery curve divided by the standard deviation of the noise in the baseline. The signal to noise of the recovery curve collected with tuning scheme A and B was 20 and 33, respectively (Figure 4.13).

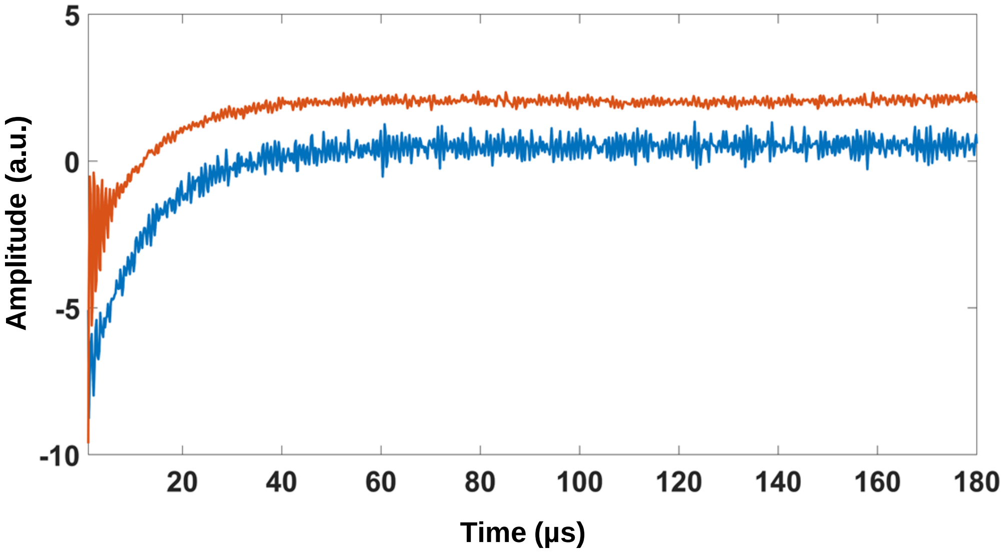

Figure 4.13: T_1 recovery curves of 0.2 mM aqueous trityl-CD_3 using tuning scheme A (blue trace, T_1 = 12.2 µs, Δω = 2.4 MHz) versus tuning scheme B (orange trace, T_1 = 11.5 µs, Δω = 6.6 MHz). The high frequency oscillation at the beginning of the orange trace is similar to an FID and has also been observed in simulations. No post-processing filter was applied to either data set.

Tuning Scheme C

Tuning the resonator to separate frequencies, as shown in Figure 4.11C, increased the isolation eliminating the need for detector blanking and allowed samples with a wider spectrum to be studied. This tuning scheme was the most useful and studied of the three. Table 4.2 summarizes typical frequency stepped parameters for the samples studied. Simulations predicted that for a constant high B_1, the measured T_1 can appear shorter than the true T_1 if the frequency step is not large enough. Conversely, for a constant size frequency step, too high a B_1 can shorten the measured T_1. For these experiments, the frequency step was held constant and the B_1 varied to experimentally determine an appropriate B_1 for a certain frequency step by comparing the measured T_1 to results measured with conventional saturation recovery.

Table 4.2: Summary of typical parameters for frequency stepped experiments using tuning scheme C. Saturation B_1 is listed.

Sample	**$\Delta\omega$ [MHz]**	**B_1 [G]**
Immobilized Nitroxide (PVA/Borate)	31-44	0.4 -0.5
0.2 mM aqueous OX63	3	0.07
0.2 mM OX63 +0.9% weight/volume NaCl	4-5	0.09
0.2 mM Aqueous Trityl-CD_3	4	0.06-0.1
Coal	34 – 36 MHz	0.09 – 0.2
Irradiated quartz	4	0.16

The sizes of the frequency step for the three trityls, coal, and quartz samples were selected such that ω_2 was located in the edges of the spectra. For the immobilized nitroxide, stepping the frequency from the center of the spectrum to the edges of the spectrum requires a step of at least 110 MHz. Although the resonators of the CLR can be tuned to that distance, a signal was not observed. This may have been due to the unintentional decrease in B_1 when ω_2 is so far outside the bandwidth of the excitation resonator. The frequency step size was decreased to 31-44 MHz at which point a signal was observed. The result was a frequency step that was well within the immobilized nitroxide spectrum when ω_1 was located at the center of the spectrum. T_1 recovery curves for each sample are shown in Figure 4.14.

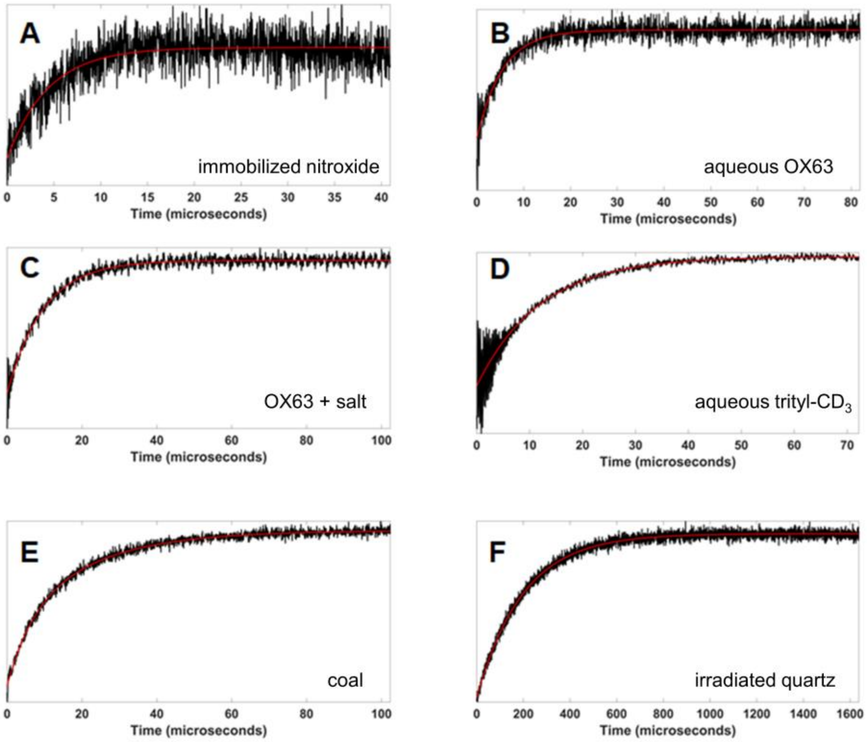

Figure 4.14: Frequency stepped T_1 recovery plots for six samples collected with tuning scheme C. Black trace is T_1 recovery curve. Red trace is exponential fit. (A) T_1 = 4.4 μs (B) T_1 = 5.4 μs (C) T_1 = 9.6 μs (D) T_1 = 11.9 μs (E) T_1 = 21.1 μs (F) T_1 =197 μs.

For comparison with frequency stepped results, saturation recovery data were collected on the spectrometer described in [44]. The 980 MHz 5 mm CLR was used for the saturation recovery experiments. The pump time in saturation recovery experiments was at least 5 times the expected T_1. The pump power used was the maximum power available on the instrument [44], about 170 mW or B_1 = 0.5 G. The observe power was selected by first inspecting the measured T_1 as a function of power. Observe powers were selected that did not shorten the measured T_1.

Data for all samples obtained using both methods were fit with a single exponential except for coal which was fit with a biexponential. Relaxation times measured with the frequency stepped method are compared to those measured with conventional saturation recovery (Table 4.3). The average T_1 reported for each sample corresponds to the parameters listed in Table 4.2. For all samples, except for the immobilized nitroxide, ω_1 was located at the center of the spectrum and stepped up field by the amount listed in Table 4.2. For the nitroxide, the measured T_1 of the low field, center field, and high field lines was 4.3 ± 0.2, 4.4 ± 0.3, and 4.3 ± 0.5, respectively. No significant difference was measured for the three spectral positions. The T_1 reported is an average value for when ω_1 was located at the low field, center field, and high field lines.

Table 4.3: T_1 measured with saturation recovery and frequency stepped method (tuning scheme C). Data for coal were fit with a biexponential. All other data were fit with a single exponential. Uncertainties were calculated as the standard deviation of at least three measurements.

Sample	**T_1 [μs] (Saturation Recovery)**	**T_1[μs] (Frequency Step)**
Immobilized Nitroxide (PVA/Borate)	4.6 ± 0.3	4.4 ± 0.4
0.2 mM aqueous OX63	6.2 ± 0.3	5.2 ± 0.1
0.2 mM OX63 +0.9% weigh/volume $NaCl_2$	9.7 ± 0.5	9.7 ± 0.1
0.2 mM Aqueous Trityl-CD_3	11.6 ± 0.4	12.1 ± 0.3
Coal	[1]24.1 ± 2.3	[1]21.1 ± 1.3
Irradiated quartz	200*	203 ± 10

[1] Longer time constant of a double exponential fit.

*Ref 68

Stepping frequency while keeping a constant B_1 was the initial intent for the frequency stepped experiments. However, to keep B_1 constant, the stepped frequencies (ω_1 and ω_2) must be at equivalent positions within the excitation resonator dip. This limits the size of the frequency step to the width of the resonator bandwidth and thus samples with a narrow signal. To extend the method to samples wider spectra, the excitation and detection resonators can be tuned far apart in frequency. However, this unintentionally lowers the B_1 during the experiment. The proposed advantage of keeping B_1 constant was that higher signal to noise could be obtained relative to conventional saturation recovery. Frequency stepping with the resonators tuned far apart in frequency results in a hybrid method combining frequency stepping and conventional saturation recovery.

4.7 Field Jump Method

Instead of stepping frequency, the field can be jumped from on resonance to an off-resonance position. To perform field jumps, Richard Quine designed and built an external circuit that uses two relay switches (MD-D249) and a high voltage (0-1000V) Glassman power supply. The maximum jump distance is determined by the current output of the Glassman power supply (70 mA). The average current is increased by adjusting the duty cycle. A 10 G field jump is obtainable with a duty cycle of 17%. When the voltage across the coils is high, the field is jumped off resonance. The relay switch is controlled by a 1-bit marker signal generated by the AWG. The disadvantage of jumping field compared to frequency stepping is that field cannot be changed instantaneously. The present hardware has a 200 ns time constant, determined by the inductance of the scan coils and the resistor in the present circuit. A 1 μs data acquisition trigger delay was used to permit the field to settle after the field jump.

The 5 mm 1.09 GHz rapid scan CLR was used for the field jump measurements. measurements. Rapid scan coils that were used for the field jump experiment had a coil constant of approximately 25 G/A and an inductance of 0.5 mH. The saturation time in the field jump experiment was at least 5*T_1. Both the size of the field jump and the B_1 were varied. For field jumps, the excitation and detection resonators are tuned to the same frequency and the power is always incident on the center of the resonator dip. B_1 is not changed during the course of the experiment.

Modifications were made to the 700 MHz to 1 GHz AWG bridge so that saturation recovery could also be performed on the same instrument and resonator as the field jumps with the intent of comparing the signal to noise of the two experiments. Specifically, two electrical switches (MiniCircuits ZFSWA2-63DR), were added before and after the JFW attenuator. This allowed two different paths of operation controlled by a 1-bit marker signal generated by the AWG. In the low state, the RF is transmitted through the JFW attenuator (Figure 3.3). In the high state, the RF is re-directed around the attenuator and transmitted at full power. The latter path is used for the pump path in saturation recovery and the former for the observe path.

4.8 Field Jump Results

Aqueous Trityl-CD_3

The T_1 of 0.2 mM aqueous trityl-CD_3 was measured using the field jump method at several field jump distances and B_1 values. Table 4.4 summarizes the results. For a constant B_1, the measured T_1 decreased for smaller field jumps. For a constant field jump distance, the longest T_1 measurements correspond to the highest B_1. The maximum B_1 available was 49 mG. The unexpected increase in T_1 at higher B_1 for a constant field jump value may be a result of better signal to noise or increased saturation at high B_1.

Table 4.4: T_1 of 0.2 mM aqueous trityl-CD_3 measured with the field jump method. Uncertainties are calculated as the standard deviation of at least three measurements.

B_1 [mG]	**T_1 [µs] Jump = 1 G**	**T_1 [µs] Jump = 0.5 G**	**T_1 [µs] Jump =0.25 G**
49	11.7 ±1.4	10.5 ± 1	10.2 ± 0.4
35	11.3 ± 1	10.3 ± 0.2	10.4 ± 0.2
25	9.2 ± 0.3	9.8 ± 0.1	11.1 ± 0.2
17	9.1 ± 0.3	9.6 ± 0.1	9.5 ± 0.2

For comparison, T_1 was measured with conventional saturation recovery using the same resonator and instrument. The pump time was equal to at least 5^*T_1, and the pump power was approximately 240 mW or 49 mG. A 1 µs trigger delay was used in saturation recovery experiments to allow for switching transients to decay away. The measured T_1 as a function of the observe B_1 is shown in Figure 4.15. The measured relaxation increased as the observe B_1 increased, consistent with expectations [69]. At low B_1, $T_1 = 12.5 \pm 0.5$ µs.

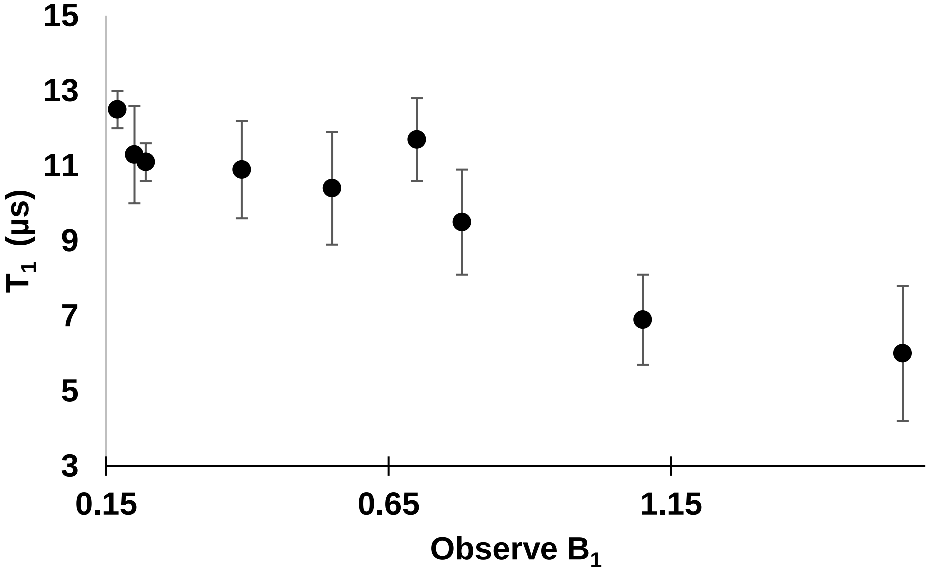

Figure 4.15: T_1 vs. observe B_1 of 0.2 mM aqueous trityl-CD_3 collected with conventional saturation recovery at 1.09 GHz. Pump B_1 = 49 mG. Uncertainties are calculated as the standard deviation of at least three measurements.

A preliminary signal to noise comparison of field jump data to conventional saturation recovery data for 0.2 mM aqueous trityl-CD_3 is shown in Figure 4.16. Both data sets used B_1 = 49 mG to saturate the line and represent the same number of averages. In the saturation recovery data, the observe B_1 was reduced to 0.17 mG. In the field jump data, the B_1 was not reduced, but the field was offset 1 G during the recovery period. The signal-to-noise for both data sets is 13. The same time constant was obtained for both data sets (T_1 = 12.9 μs).

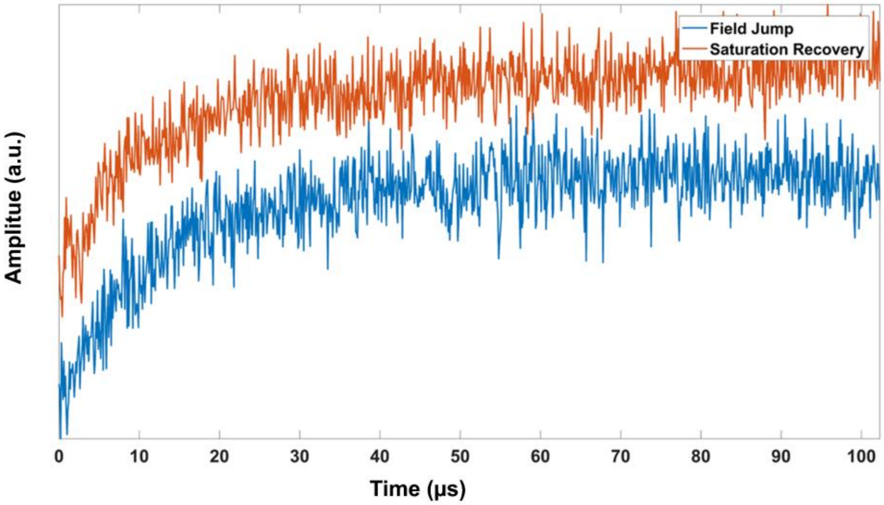

Figure 4.16: Comparison of saturation recovery and field jump data at 1.09 GHz for 0.2 mM aqueous trityl-CD_3. Field jump data taken with B_1 = 49 mG with a 1 G field jump. Saturation recovery data had a pump B_1 = 49 mG and observe B_1 = 0.4 mG. Both were collected with 204800 averages.

4.9 Summary and Future Directions

Proof of principle experiments have been demonstrated using rapid scan, frequency step, and field jumps to measure spin-lattice relaxation times of a variety of samples. T_1 relaxation times measured with these new methods were compared to conventional methods. A summary of all T_1 measurements is shown in Table 4.5.

Table 4.5: Summary of T_1 measurements [μs]. Frequency step results correspond to tuning scheme C.

	Rapid Scan	Frequency Step	Field Jump	Inversion Recovery	Saturation Recovery
0.2 mM aqueous trityl-CD_3	14 ± 2	12.1 ± 0.3	11.7 ±1.4[d]	12.7 ± 0.1	11.6 ± 0.4[b] 12.5 ± 0.5[c]
0.2 mM trityl-CD_3 in 1:1 water:glycerol	16.4 ± 1.2			16.1 ± 0.2	
0.2 mM aqueous OX63		5.2 ± 0.1			6.2 ± 0.3
0.2 mM OX63 + salt		9.7 ± 0.1			9.7 ± 0.5
Immobilized nitroxide PVA/Borate		4.4 ± 0.4			4.6 ± 0.3
Coal	15.2 ± 2.2	21.1 ± 1.3[a]			18.6 ± 0.9 24.1 ± 2.3[a]
Quartz	150-230	203 ± 10			*200

*Ref. 68

[a] Longer time constant of a biexponential

[b] Data collected on spin echo system/copper 980 MHz CLR

[c] Data collected on AWG system/RS 1.09 GHz CLR

[d] Data collected with 1 G jump and B_1 = 49 mG

Future directions of the rapid scan technique depend on scanning at faster scan frequencies and rates to be able to measure samples with shorter relaxation times. However, even with faster scan rates there will be much fewer points that define the recovery curve than for other methods.

Frequency stepping is relatively easy to do with an AWG and can be done with nanosecond resolution. However, the current method implementation has several disadvantages. When tuning scheme A or B is used, the size of the frequency step is limited by the resonator bandwidth. Tuning the resonators (tuning scheme C) to far apart frequencies remedies this problem but also introduces an unintentional drop in B_1. The results of these experiments represent a change in both B_1 and frequency which may result in a decrease of signal to noise relative to simulated predications. In the future, passage phenomena such as adiabatic inversion when the frequency change is fast relative to relaxation times could be incorporated into these techniques. Simulations predict that dispersion, which is less readily saturated than absorption, is measured at the stepped frequency but we have not yet unambiguously demonstrated the relative contributions that are observed.

Field jump experiments are the most promising. Since B_1 is not changed during the field jump, this technique, with further development, may yield higher signal to noise than conventional saturation recovery. The size of the field jump is not limited by the resonator bandwidth as it is in the frequency step method. Here, the size of the field jump is determined by the current output of the high voltage power supply. As the B_1 increased in the field jump experiments, the measured T_1 approached the expected value that was measured with conventional saturation recovery and pulse techniques. The field jump results suggest that a higher B_1 could be used compared to saturation recovery, possibly offering an increase in signal-to-noise. The highest B_1 available for the results presented was 49 mG. The high power Tomco (300 W) amplifier mentioned in Chapter 3 could be used to increase the power at the expense of data collection time.

Chapter 5: Pulse Shaping at 1.5 GHz

5.1 Introduction

The range of frequencies excited by a pulse is the excitation bandwidth. The fundamental idea of pulse shaping is to increase the uniformity of the excitation bandwidth. The excitation bandwidth is predicted by the Fourier transform of the pulse shape. The rectangular pulses that are most commonly used in EPR are the simplest type of pulse to generate. The shorter the rectangular pulse, the greater the power required for a given turning angle (eq. 4.1). Analysis of a rectangular pulse in the Fourier domain reveals a sinc shaped excitation profile (Figure 5.1).

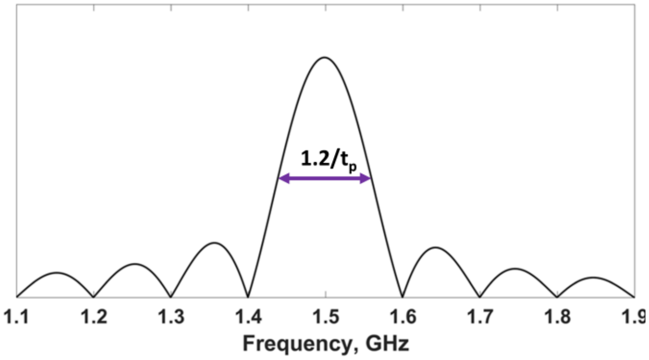

Figure 5.1: FT of 10 ns rectangular pulse centered at 1.5 GHz.

The length of a rectangular pulse (t_p) is inversely proportional to its excitation bandwidth. The "uniform" region of the excitation bandwidth for a π/2 rectangular pulse can be approximated by 1.2/t_p [72]. With that criterium, even a relatively short 10 ns rectangular pulse only excites about 120 MHz (~43 G) of spectra. This is insufficient to cover the bandwidths needed to uniformly excite some immobilized nitroxide radicals [25]. Moreover, the excitation is not uniformly flat over this bandwidth (Figure 5.1). A goal of pulse shaping is to make the excitation bandwidth more uniform.

The first reported use of shaped pulses in EPR was in 1989 when Freed et. al. described phase alternating composite pulses [73]. Since then, AWGs have provided an opportunity to create a variety of pulse shapes by modulating frequency, phase, and amplitude. The bandwidth of EPR spectra can be hundreds of MHz wide, and creating pulses that uniformly excite that entire region is crucial for obtaining data free from artifacts. Variable-rate frequency chirped pulses have been shown to uniformly excite 200 MHz encompassing the spectral width of an immobilized nitroxide at X-band [74]. The use of sech/tanh pulses at X-band increased the inversion efficiency for a Co^{2+} nitroxide biradical spectrum which improved the signal to noise of double electron-electron measurements [75]. Sinc shaped pulses produced images with a more uniform intensity profile at 300 MHz compared to images produced with rectangular pulses [76]. The Frank polyphase sequence was applied at 256 MHz to reduce the power required for pulses [77, 78].

The response function for an EPR resonator limits the uniformity of the pulse excitation. A common goal of pulse shaping is to create a pulse with a uniform excitation bandwidth that takes account of the resonator response (transfer) function. The response function for an EPR resonator has a Lorentzian shape centered around the resonator frequency (ω_0), referred to as the resonator dip [56]. The power response of the resonator dip is logarithmic. The resonator bandwidth ($\Delta\omega$) is defined by the 3 dB points. At the -3dB frequencies, half of the incident power on the resonator is reflected out. The quality factor, Q, of the resonator characterizes the bandwidth of the resonator (equation 5.1) [79, 80].

$$Q = \omega_0/\Delta\omega \qquad \text{eq. 5.1}$$

The resonator Q and bandwidth describe the resonator response function. Figure 5.1 assumes an infinitely low Q and wide resonator bandwidth. Figure 5.2 shows the excitation bandwidth resulting from a 100 ns pulse for two resonator Q values. Although the pulse length is the same and the predicted uniform excitation bandwidth is 12 MHz for both cases, the higher resonator Q value reduces the uniformity for the same pulse length.

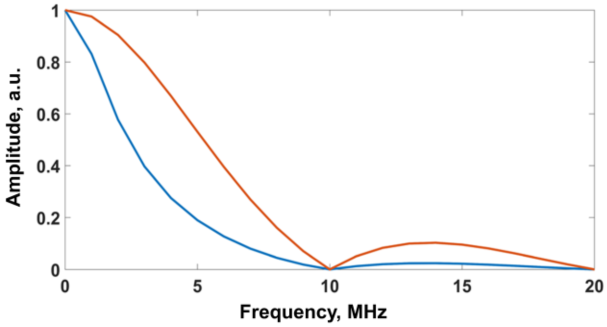

Figure 5.2: Excitation bandwidth of 100 ns rectangular pulse with Q = 100 (orange trace) and Q = 500 (blue trace). Positive frequencies offset from 1.5 GHz are shown. The simulation program to perform this calculation was written by George Rinard.

After a pulse, a resonator rings for a certain amount of time to dissipate the energy of the pulse. This ring down time is directly related to the Q of the resonator by equation 5.2, where τ is the ring down time constant [57].

$$Q = 2\pi\omega_0\tau \qquad \text{eq. 5.2}$$

In addition to the resonator response function, the microwave components of a spectrometer contribute to non-uniform pulse excitation, partly because high-power amplifiers generally operate in a non-linear regime. Doll et. al used nutation experiments to characterize the spectrometer transfer function to create frequency chirped pulses with uniform excitation bandwidths [81]. Optimum control theory has been utilized to provide real time feedback on pulse shaping [82].

The response of a resonator to a pulse is a damped sinusoid (Figure 5.3A) which served as the starting point for the derivation of a new shaped pulse. Dr. George Rinard derived an exponential sine shaped pulse by determining the pulse frequency (ω_1) and time constant (a) that should provide an optimally flat excitation bandwidth for a given resonator Q. The result of the derivation yielded an exponential sine pulse defined by equation 5.3:

$$f(t) = \sin(2\pi\omega_1 t)\, e^{\frac{-t}{a}} \sin(2\pi\omega_0 t) \quad \text{eq. 5.3}$$

Where, $\omega_1 = \frac{\omega_0}{2Q}$, $a = \sqrt{\sqrt{5} - 2}\,\frac{\pi\omega_0}{Q}$, and ω_0 = center of resonator dip

In addition to the exponential sine pulse, three-pulse composite rectangular pulses were tested. A three-part composite rectangular pulse is defined as a series of rectangular pulses with 180° phase changes at two defined positions. Examples of the exponential sine and three-part composite rectangular pulses are shown in Figure 5.3.

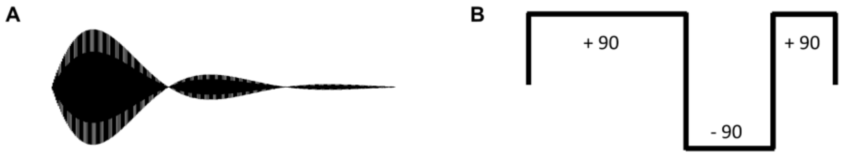

Figure 5.3: Examples of shaped pulses. (A) exponential sine pulse (B) envelope of three-part rectangular composite pulse.

5.2 Experimental Method

Mathcad simulations written by Dr. Rinard were performed to predict the excitation bandwidth and B_1 uniformity resulting from exponential sine, rectangular composite, and conventional rectangular pulses. These simulations guided the selection of resonator Q and pulse lengths for the experiments presented below.

The B_1 uniformity in the resonator is proportional to the product of the excitation bandwidth produced by a pulse and the current in the resonator after a voltage pulse. The exponential sine pulses are designed to account for resonator Q whereas the rectangular pulses do not. The resonator response, determined by Q, to a rectangular pulse distorts the excitation bandwidth and B_1 uniformity in the resonator. To compare rectangular pulses to exponential sine pulses, the resonator Q was varied for different pulse shapes to achieve the desired bandwidth excitation predicted by simulation. The excitation bandwidth of the simulations was measured at the frequencies where the amplitude was down 3 dB (0.707) from the maximum amplitude. The exponential sine pulse was calculated using eq. 5.3 and was truncated after 1.5 cycles where the amplitude of the RF was nearly zero. The rectangular and composite rectangular pulse lengths were determined empirically using Mathcad simulations. For comparison, the rectangular and composite rectangular pulse lengths of the were selected to have the same excitation bandwidth as the exponential sine pulses.

Resonator characterization was done prior to each experiment. The bandwidth and center frequency of the resonator were measured by observing the Fourier transform of a reflected frequency chirped pulse on a high-speed oscilloscope. The Q of the reflection resonator used in these experiments was adjustable. The pulses were applied at the frequency corresponding to the center of the resonator dip (f_0). Pulse power was optimized and selected by varying the RF power until a maximum echo or FID signal was observed.

A 1 cm long 0.2 mM aqueous trityl-CD_3 sample in a 4 mm OD tube was degassed with N_2 and flame sealed. A 4 mm OD sample of 2,5-di-t-butyl-1,4-benzosemiquinone (25DTBSQ) was prepared as previously described [83]. A 0.1 mM aqueous solution of amino substituted triarylmethyl radical ($aTAM_4$) pH = 6.5 was prepared as previously described [84] and placed in a 4 mm OD tube. The $aTAM_4$ and 25DBTSQ samples were purged with N_2 after preparation and during measurements.

Experiments were performed at 1.5 GHz using the spectrometer described in Ref. 44 and a 4 mm reflection resonator described in Ref. 30. The Fluke source on the spectrometer was replaced with the Tektronix AWG 70002A to facilitate pulse shaping. Pulse waveforms were calculated in Matlab. The amplified RF signal from the resonator was detected at the source frequency using an Agilent U1084 digitizer card. The digitizer card sampled the RF signal at 4 Gs/s. In post-processing, two digital reference waveforms were calculated in Matlab. Quadrature data were generated by multiplying two reference waveforms, differing by 90°, by the data and combining the two channels to form a complex signal.

In Fourier transform (FT) EPR the spectrum is acquired via Fourier transformation of an echo or FID. One way to measure the excitation bandwidth of a pulse is to measure the intensity of a frequency peak in the Fourier domain as a function of magnetic field offset from resonance. A trityl-CD_3 sample was used for this measurement because it has a narrow line (~ 150 kHz) [48] and produces a strong FID signal. The magnetic field was stepped in 100 mG steps and at each magnetic field value, a π/2 pulse was applied to generate an FID. The amplitude of the trityl-CD_3 FID signal was measured in the Fourier transform domain at each magnetic field value. A 3-point moving average smoothing filter was applied to the frequency peaks and amplitudes were plotted as a function of magnetic field. The excitation bandwidth was measured at the frequencies where the amplitude was 3 dB down from the maximum. This procedure was used to measure the excitation bandwidth of the exponential sine, composite rectangular, and rectangular pulses. Another way to evaluate the bandwidth excitation uniformity for a given pulse is to excite a broad spectrum on or close to resonance and compare the intensities in the outer regions of the spectrum. This procedure was applied to 25DBTSQ and $aTAM_4$. The excitation bandwidth and the required power to achieve a π/2 turning angle are compared for exponential sine, rectangular, and composite rectangular pulses.

5.3 Results

Three pulse shapes were calculated using Mathcad simulations to excite a 15 MHz bandwidth: a 46 ns rectangular pulse, a 191 ns composite rectangular pulse, and a 190 ns exponential sine pulse. The resonator Q was lower (Q = 53) for the 46 ns rectangular and 191 ns composite rectangular pulses to achieve the excitation bandwidth predicted by simulation. Because the exponential sine pulse accounts for the resonator Q (eq. 5.3), a higher Q (Q=96) was used for that pulse. Two additional pulses were tested: a 190 ns rectangular pulse (Q = 96) and a 96 ns rectangular composite pulse (Q=53). The 190 ns rectangular pulse was tested to compare the relative power requirements for a π/2 turning angle and excitation bandwidth compared to the exponential sine pulse of the same length. The 96 ns composite rectangular pulse was chosen because simulations predicted the same power requirement as the 46 ns rectangular pulse but a wider excitation bandwidth. The 191 ns rectangular composite pulse had two 180° phase inversions: one at 113 ns and another 165 ns. The 96 ns composite pulse inverted phase at 56 ns and 83 ns. Comparisons of the excitation bandwidth plots are shown in Figures 5.4 (Q=53) and 5.5 (Q=96). The excitation bandwidth and power required for a π/2 pulse is summarized in Table 5.1.

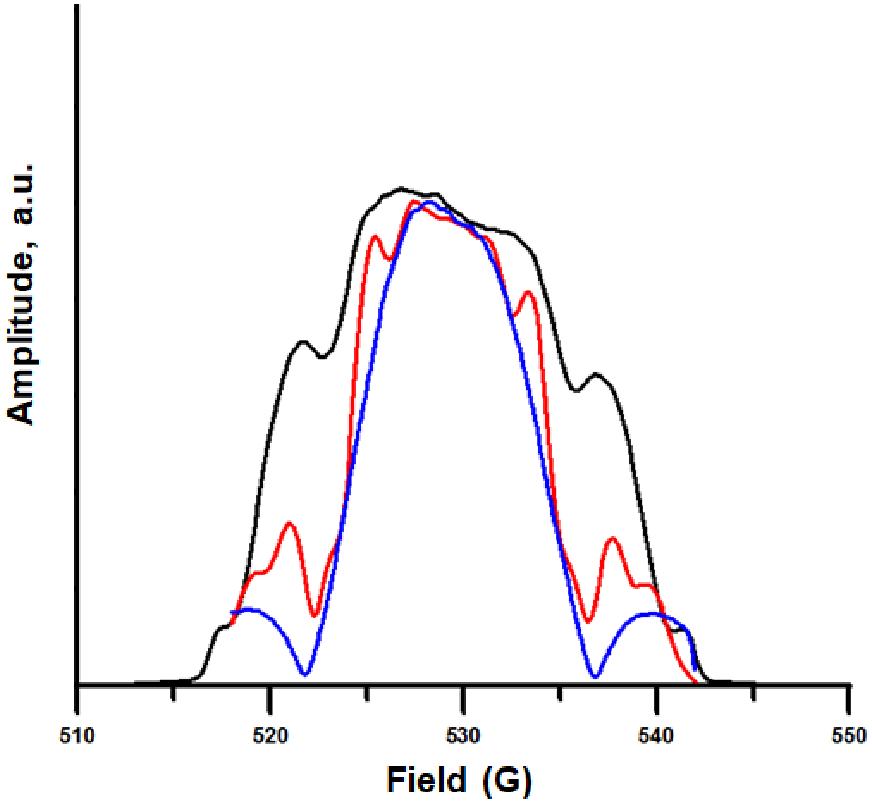

Figure 5.4: Comparison of rectangular pulse and rectangular composite pulses. Excitation bandwidth of 46 ns rectangular pulse (blue), 191 ns composite rectangular pulse (red), and 96 ns composite rectangular pulse (black). Resonator Q = 53.

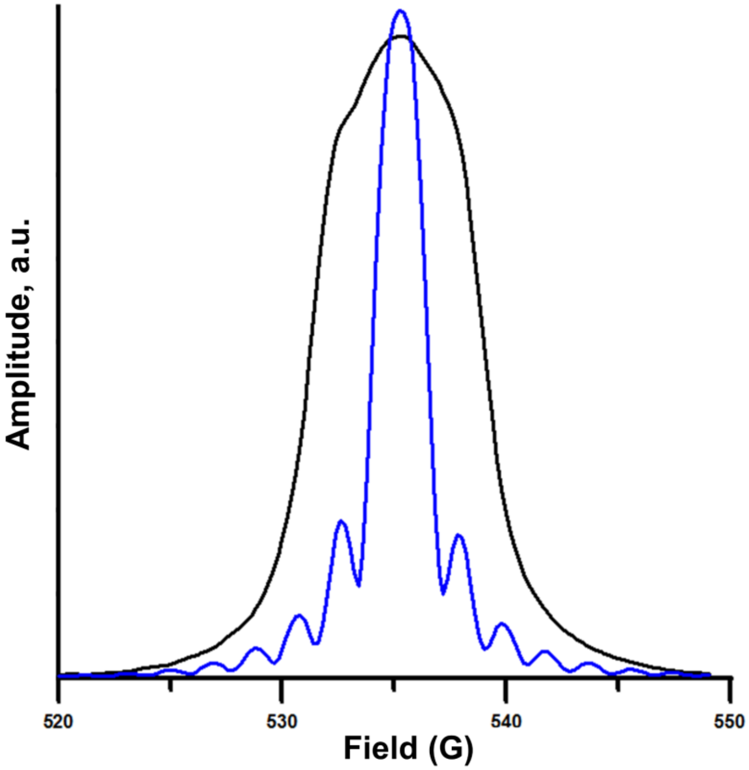

Figure 5.5: Comparison of exponential sine and rectangular pulses. Excitation bandwidth of 190 ns exponential sine pulse (black) and 190 ns rectangular pulse (blue). Resonator Q = 96.

Table 5.1: Comparison of excitation bandwidth and power required for a π/2 turning angle for several pulse shapes.

Pulse	**Measured Excitation Bandwidth (MHz)**	**Power (W)**	**Resonator Q**
46 ns Rectangular	14	0.7	53
191 ns Composite Rectangular	14	0.2	53
190 ns Exponential Sine	13	0.7	96
190 ns Rectangular	4	0.02	96
96 ns Composite Rectangular	25	0.9	53

Three pulse patterns had approximately the same excitation bandwidth (13-14 MHz): the 46 ns rectangular, 191 ns composite rectangular, and the 190 ns exponential sine pulse. Of the three, the 191 ns composite rectangular pulse (Q = 53) required the least amount of power for a π/2 turning angle. The 190 ns exponential sine (Q = 96) and 46 ns rectangular pulse (Q = 53) required the same amount of power that was about a factor of 3 higher than for the 191 ns composite rectangular pulse (Q = 53). A 190 ns rectangular pulse (Q = 96) had a much smaller excitation bandwidth, only 4 MHz, and required much less power than the 190 exponential sine pulse (Q=96). The 96 ns composite rectangular pulse (Q = 53) excited 10 MHz more than the 46 ns rectangular pulse (Q =53) for about the same amount of power. The uncertainty in reported power is relative to attenuation which is about ±1 dB (0 dB = 23 W).

The 46 ns rectangular pulse (resonator Q = 53), 191 ns composite rectangular pulse (resonator Q = 53), and 190 ns exponential pulse (resonator Q = 96) were also tested on the amino substituted triarylmethyl radical (aTAM$_4$) with pH = 6.5. A two-pulse sequence

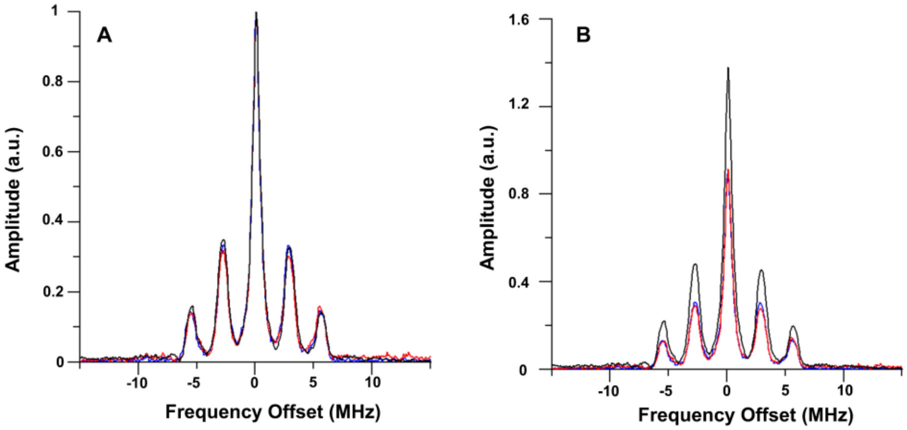

Figure 5.6: FT EPR spectra of aTAM$_4$. (A) Normalized intensities and absolute intensities (B) of spectra produced using a 46 ns rectangular pulse (blue), 191 ns composite rectangular pulse (red), or 190 ns exponential sine pulse (black).

was used to generate an echo using each pulse shape. The 5-line spectrum produced by the FT of the echo is shown in Figure 5.6A and B. The normalized intensities of the spectra produced by all three pulse sequences are the same (Figure 5.6A) indicating that the excitation bandwidth over the range of about ±6 MHz for the three cases is equal. However, the absolute intensity of the spectrum produced with the exponential sine pulse is about 50% larger (Figure 5.6B). This is because the resonator Q that was used with the exponential sine pulse is about twice that which was used for the rectangular and composite rectangular pulses.

25DBTSQ spectra were collected by applying a π/2 pulse slightly off resonance. The Fourier transform of the FID produced the 3-line spectrum spanning about 14 MHz (Figure 5.7). Three different pulses were tested: a 295 ns exponential sine pulse, a 295 ns rectangular pulse, and a 30 ns rectangular pulse. The resonator Q for all pulses was

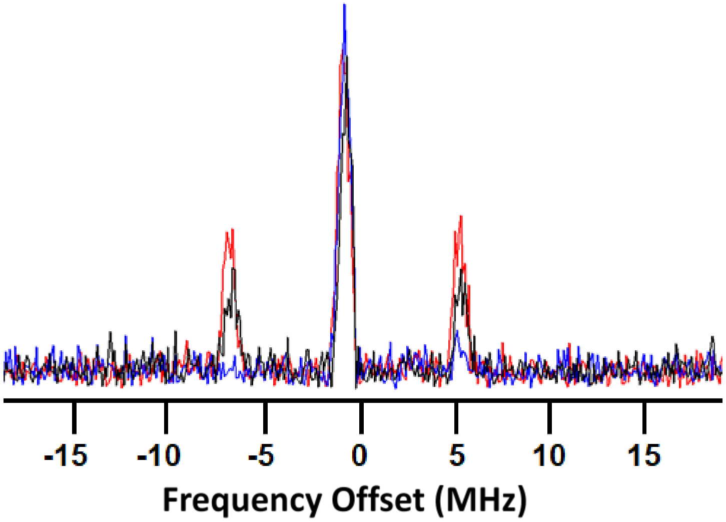

Figure 5.7: FT EPR spectra of 25DBTSQ generated by a 295 ns exponential sine pulse (red), 295 ns rectangular pulse (blue), or 30 ns rectangular pulse (black).

approximately 110. The power required to generate a π/2 turning angle for both the 295 ns exponential sine and 30 ns rectangular pulse was about 1.25 W. However, the excitation bandwidth of the 295 ns exponential sine pulse was more uniform. This can be seen in Figure 5.7 in which the outer lines of the spectrum have a higher amplitude that is closer to the expected 1:2:1 ratio. The 295 ns rectangular pulse only required 25 mW for a π/2 turning angle but clearly had a much narrower excitation bandwidth as can be seen by the low intensity outer lines in the spectrum (Figure 5.7).

Table 5.2: Instrumental deadtime measurements for several pulse shapes at 1.49 GHz.

Pulse Shape	**Deadtime (ns)**	**Power (W)**	**Resonator Q**	**Excitation Bandwidth (MHz)**
71 ns Rectangular	335	0.4	80	13
100 ns Rectangular Composite	335	0.3	80	12
320 ns Exponential Sine	327	0.4	150	12

The deadtime of an EPR instrument is the amount of time after a pulse until a signal can be detected and is a result of resonator ring down and switching transients. The instrumental deadtime following three pulses shapes designed to excite approximately 12 MHz of bandwidth is compared in Table 5.2. The reported deadtime is calculated from the end of the pulse to the point at which the detection system recovers from saturation. The measurements of instrument deadtime are not significantly different for the three pulse shapes.

5.4 Summary and Future Directions

Relative power requirements, excitation bandwidth and resulting instrumental deadtimes were compared for exponential sine, rectangular, and composite rectangular pulses. To achieve equal uniform excitation across the same bandwidth, a lower resonator Q was used for rectangular pulses compared to exponential sine pulses.

When designed to have equal bandwidth excitation, the exponential sine pulse and conventional rectangular pulse required approximately the same amount of power to generate a π/2 turning angle. The relative benefit of using an exponential sine pulse is that for the same power as a rectangular pulse, a higher resonator Q can be utilized and the uniformity is increased. A higher resonator Q increases sensitivity [85]. As previously shown [73], rectangular composite pulses have an increased uniform bandwidth excitation compared to rectangular pulses that require the same power for a π/2 turning angle. The instrumental deadtime corresponding to exponential sine, rectangular and rectangular composite pulses is approximately the same on this spectrometer. The significant contribution to the deadtime may be from switching transients instead of resonator ring down.

The excitation bandwidth and power requirements have been tested for both the exponential sine and rectangular pulses. Going forward, these pulses should be applied to more complex EPR experiments. An important test of uniform spectral coverage would be inversion recovery experiments to measure T_1. Uniform excitation of spectra using shaped pulses may decrease spectral diffusion processes and yield an accurate T_1 measurement.

Using exponential sine pulses and thus higher Q, pulsed EPR imaging could benefit from increased sensitivity and uniform excitation.

References

[1] L. J. Berliner and J. Reuben, "Spin Labeling Theory and Applications," (Biological Magnetic Resonance.) New York: Plenum Press, 1989.

[2] G. M. Rosen, B. E. Britigan, H. J. Halpern, and S. Pou, *Free Radicals: Biology and Detection by Spin Trapping*. New York: Oxford University Press, 1999.

[3] G. R. Eaton and S. S. Eaton, "Electron paramagnetic resonance spectroscopy," *Comp. Coord. Chem. II*, vol. 2, pp. 37-48, 2004.

[4] L. J. Berliner, "In Vivo EPR (ESR): Theory and Application," (Biol. Magn. Reson.) New York: Kluwer Academic, 2003.

[5] M. Elas, B. Williams, A. Parasca, C. Mailer, C. A. Pelizzari, M. A. Lewis, J. N. River, G. S. Karczmar, E. D. Barth, and H. J. Halpern, "Quantitative tumor oxymetric images from 4D electron paramagnetic resonance imaging (EPRI): Methodology and comparison with blood oxygen level-dependent (BOLD) MRI," *Magn. Reson. Med.*, vol. 49, pp. 682-91, 2003.

[6] H. B. Elajaili, J. R. Biller, G. M. Rosen, J. P. Y. Kao, M. Tseytlin, L. A. Buchanan, G. A. Rinard, R. W. Quine, J. McPeak, Y. Shi, S. S. Eaton, and G. R. Eaton, "Imaging Disulfide Dinitroxides at 250 MHz to Monitor Redox Status," *J. Magn. Reson.*, vol. 260, pp. 77 - 82, 2015.

[7] A. A. Bobko, T. D. Eubank, J. L. Voorhees, O. V. Efimova, I. A. Kirilyuk, S. Petryakov, D. G. Trofimiov, C. B. Marsh, J. L. Zweier, I. A. Grigorev, A. Samouilov, and V. V. Khramtsov, "In Vivo Monitoring of pH, Redox Status, and Glutathione Using L-Band EPR for Assessment of Therapeutic Effectiveness in Solid Tumors," *Magn. Reson. Med.*, vol. 67, pp. 1827 - 1836, 2012.

[8] G. A. Rinard, R. W. Quine, S. S. Eaton, and G. R. Eaton, "Frequency dependence of EPR sensitivity," *Biol. Magn. Reson.*, vol. 21, pp. 115-154, 2004.

[9] L. Yong, J. Harbridge, R. W. Quine, G. A. Rinard, S. S. Eaton, G. R. Eaton, C. Mailer, E. Barth, and H. J. Halpern, "Electron Spin Relaxation of Triarylmethyl Radicals in Fluid Solution," *J. Magn. Reson.*, vol. 152, pp. 156-161, 2001.

[10] B. Epel, M. K. Bowman, C. Mailer, and H. J. Halpern, "Absolute Oxygen R1e Imaging *in vivo* with pulse electron paramagnetic resonance," *Magn. Reson. Med.*, vol. 72, pp. 362 - 368 2014.

[11] R. Thomlinson and L. Gray, "The Histological Structure of Some Human Lung Cancers and the Possible Implications for Radiotherapy," *British Journal of Cancer*, vol. 9, pp. 539-549, 1955.

[12] R. Ahmad and P. Kuppusamy, "Theory, Instrumentation, and Applications of Electron Paramagnetic Resonance Oximetry," *Chem. Rev.*, vol. 110, pp. 3212-3236, 2010.

[13] J. M. Brown and W. R. Wilson, "Exploiting Tumour Hypoxia in Cancer Treatment," *Nature Reviews, Cancer,* vol. 4, pp. 437-447, 2016.

[14] F. Bloch, W. W. Hansen, and M. Packard, "The Nuclear Induction Experiment," *Phys. Rev.*, vol. 70, pp. 474-485, 1946.

[15] J. W. Stoner, D. Szymanski, S. S. Eaton, R. W. Quine, G. A. Rinard, and G. R. Eaton, "Direct-detected rapid-scan EPR at 250 MHz," *J. Magn. Res.,* vol. 170, pp. 127-135, 2004.

[16] J. P. Joshi, J. R. Ballard, G. A. Rinard, R. W. Quine, S. S. Eaton, and G. R. Eaton, "Rapid-Scan EPR with Triangular Scans and Fourier Deconvolution to Recover the Slow-Scan Spectrum," *J. Magn. Reson.,* vol. 175, pp. 44-51, 2005.

[17] J. P. Joshi, G. R. Eaton, and S. S. Eaton, "Impact of Resonator on Direct-Detected Rapid-Scan EPR at 9.8 GHz," *Appl. Magn. Reson.,* vol. 28, pp. 239-249, 2005.

[18] M. Tseitlin, R. W. Quine, G. A. Rinard, S. S. Eaton, and G. R. Eaton, "Combining Absorption and Dispersion Signals to Improve Signal-to-noise for Rapid Scan EPR Imaging," *J. Magn. Reson.,* vol. 203, pp. 305-310, 2010.

[19] R. W. Quine, T. Czechowski, and G. R. Eaton, "A Linear Magnetic Field Scan Driver," *Conc. Magn. Reson., Magn. Reson. Engineer,* vol. 35B, pp. 44-58, 2009.

[20] G. A. Rinard, R. W. Quine, J. R. Biller, and G. R. Eaton, "A Wire Crossed-Loop-Resonator for Rapid Scan EPR," *Conc. Magn. Reson. B, Magn. Reson. Engineer,* vol. 37B, pp. 86-91, 2010.

[21] D. G. Mitchell, G. M. Rosen, M. Tseitlin, B. Symmes, S. S. Eaton, and G. R. Eaton, "Use of Rapid-Scan EPR to Improve Detection Sensitivity for Spin-Trapped Radicals," *Biophys. J.* , vol. 105, pp. 338 - 342, 2013.

[22] M. Tseitlin, G. A. Rinard, R. W. Quine, S. S. Eaton, and G. R. Eaton, "Deconvolution of Sinusoidal Rapid EPR Scans," *J. Magn. Reson*, vol. 208, pp. 279-283, 2011.

[23] N. Bloembergen, E. M. Purcell, and R. V. Pound, "Relaxation Effects in Nuclear Resonance Absorption," *Phys. Rev.*, vol. 73, pp. 679-712, 1948.

[24] D. G. Mitchell, R. W. Quine, M. Tseitlin, V. Meyer, S. S. Eaton, and G. R. Eaton, "Comparison of Continuous Wave, Spin Echo, and Rapid Scan EPR of Irradiated Fused Quartz," *Radiat. Meas.*, vol. 46, pp. 993-996, 2011.

[25] Z. Yu, R. W. Quine, G. A. Rinard, M. Tseitlin, H. Elajaili, V. Kathirvelu, L. J. Clouston, P. J. Boratyński, A. Rajca, R. Stein, H. Mchaourab, S. S. Eaton, and G. R. Eaton, "Rapid-Scan EPR of Immobilized Nitroxides," *J. Magn. Reson.*, vol. 247 pp. 67 - 71, 2014.

[26] Y. Shi, G. A. Rinard, R. W. Quine, S. S. Eaton, and G. R. Eaton, "Rapid scan electron paramagnetic resonance at 1.0 GHz of defect centers in γ-irradiated organic solids," *Rad. Measur.*, vol. 85, pp. 57 - 63, 2016.

[27] G. R. Eaton and S. S. Eaton, "Introduction to EPR imaging using magnetic-field gradients," *Conc. Magn. Reson., Magn. Reson. Engineer*, vol. 7, pp. 49-67, 1995.

[28] B. Epel and H. Halpern, "Imaging," *EMagRes*, vol. 6, pp. 149-160, 2017.

[29] S. S. Eaton, Y. Shi, L. Woodcock, L. A. Buchanan, J. McPeak, R. W. Quine, G. A. Rinard, B. Epel, H. J. Halpern, and G. R. Eaton, "Rapid Scan EPR Imaging," *J. Magn. Reson.*, vol. 280, pp. 140 - 148, 2017.

[30] G. A. Rinard, R. W. Quine, S. S. Eaton, and G. R. Eaton, "Frequency dependence of EPR signal intensity, 250 MHz to 9.1 GHz," *J. Magn. Reson.*, vol. 156, pp. 113-121, 2002.

[31] M. Tseitlin, T. Czechowski, R. W. Quine, S. S. Eaton, and G. R. Eaton, "Background Removal Procedure for Rapid Scan EPR," *J. Magn. Reson.*, vol. 196, pp. 48-53, 2009.

[32] L. A. Buchanan, L. B. Woodcock, R. W. Quine, G. A. Rinard, S. S. Eaton, and G. R. Eaton, "Background correction in rapid scan EPR spectroscopy," *J. Magn. Reson.*, vol. 293, pp. 1-8, 2018.

[33] J. R. Biller, M. Tseitlin, R. W. Quine, G. A. Rinard, H. A. Weismiller, H. Elajaili, G. M. Rosen, J. Kao, S. S. Eaton, and G. R. Eaton, "Imaging of nitroxides at 250 MHz using rapid-scan electron paramagnetic resonance" *J. Magn. Reson.*, vol. 242, pp. 162 - 168, 2014.

[34] R. W. Quine, D. G. Mitchell, S. S. Eaton, and G. R. Eaton, "A Resonated Coil Driver for Rapid Scan EPR," *Conc. Magn. Reson., Magn. Reson. Engineer,* vol. 41B, pp. 95 - 110, 2012.

[35] L. Buchanan, G. A. Rinard, R. W. Quine, Y. Shi, S. S. Eaton, and G. R. Eaton, "250 MHz Rapid Scan Cross Loop Resonator," *Appl. Magn. Reson.,* submitted, 2018.

[36] R. W. Quine, G. A. Rinard, S. S. Eaton, and G. R. Eaton, "A pulsed and continuous wave 250 MHz electron paramagnetic resonance spectrometer," *Conc. in Magn. Reso., Magn. Reson. Engineer,* vol. 15, pp. 59-91, 2002.

[37] L. Buchanan, G. A. Rinard, R. Quine, S. S. Eaton, and G. R. Eaton, "Table-top 700 MHz EPR Imaging Spectrometer," *Conc. Magn. Reson., Magn. Reson. Engineer,* accepted for publication, 2018.

[38] H. Sato-Akaba, M. Emoto, G. Hirata, and H. Gujii, "Design and Testing of a 750 MHz CW-EPR digital console for small animal imaging," *J. Magn. Reson.,* vol. 284, pp. 48-58, 2017.

[39] T. Sato, H. Yokoyama, H. Ohya, and H. Kamada, "An active resonator system for CW-ESR measurement operating at 700 MHz," *J. Magn. Reson.,* vol. 159, pp. 161-166, 2002.

[40] S. Matsumoto, F. Hyodo, S. Subramanian, N. Devasahayam, J. Munasinghe, E. Hyodo, C. Gadisetti, J. A. Cook, J. B. Mitchell, and M. C. Krishna, " Low-field paramagnetic resonance imaging of tumor oxygenation and glycolytic activity in mice," *J. Clinical Invest.,* vol. 118, pp. 1965 - 1973, 2013.

[41] H. J. Halpern and M. K. Bowman, "Low-frequency EPR spectrometers: MHz range," in *EPR Imaging and In Vivo EPR*, G. R. Eaton, S. S. Eaton, and K. Ohno, Eds. Boca Raton: CRC Press, 1991, ch. 6.

[42] J. S. Hyde, M. E. Newton, R. A. Strangeway, T. G. Camenisch, and W. Froncisz, "Electron paramagnetic resonance Q-band bridge with gallium arsenide field-effect transistor signal amplifier and low-noise Gunn diode oscillator," *Rev. Sci. Instrum.,* vol. 62, pp. 2969-75, 1991.

[43] T. Oles, J. L. Strangeway, W. Froncisz, and J. Hyde, "X-band low phase noise Gunn diode oscillator for EPR spectroscopy," *Rev. Sci. Instrum.,* vol. 63, pp. 4010-4011, 1992.

[44] R. W. Quine, G. A. Rinard, B. T. Ghim, S. S. Eaton, and G. R. Eaton, "A 1-2 GHz pulsed and continuous wave electron paramagnetic resonance spectrometer," *Rev. Sci. Instrum.,* vol. 67, pp. 2514-2527, 1996.

[45] J. E. McPeak, R. W. Quine, S. S. Eaton, and G. R. Eaton, "An X-band Saturation Recovery EPR Spectrometer Based on an Arbitrary Waveform Generator," *Rev. Sci. Instrum.,* submitted, 2018.

[46] Keysight, "High Accuracy Noise Figure Measurements Using the PNA-X Series Network Analyzer," in *literature.cdn.keysight.com/litweb/pdf/5990-5800EN.pdf* vol. 5990-5800EN, Keysight, Ed., 2014, p. 7.

[47] G. A. Rinard, R. W. Quine, R. Song, G. R. Eaton, and S. S. Eaton, "Absolute EPR Spin Echo and Noise Intensities," *J. Magn. Reson.*, vol. 140, pp. 69-83, 1999.

[48] S. N. Trukhan, V. F. Yudanov, O. Rogozhnikova, D. Trukhin, M. K. Bowman, M. D. Krzyaniak, H. Chen, and O. N. Martyanov, "Hyperfine Interactions of Narrow-line Trityl Radicals with Solvent Molecules," *J. Magn. Reson.*, vol. 233, pp. 29 - 36, 2013.

[49] S. S. Eaton, G. R. Eaton, and L. J. Berliner, "Biomedical EPR - Part B: Methodology, Instrumentation, and Dynamics," (Biol. Magn. Reson.) New York: Kluwer Academic/Plenum Press, pp. 3-52, 2005.

[50] R. W. Quine, G. A. Rinard, Y. Shi, L. A. Buchanan, J. R. Biller, S. S. Eaton, and G. R. Eaton, "UHF EPR Spectrometer Operating at Frequencies Between 400 MHz and 1 GHz," *Conc. Magn. Reson. B, Magn. Reson. Engineering*, vol. 46B, pp. 123 - 133, 2016.

[51] M. Tseitlin, J. R. Biller, H. Elajaili, V. Khramtsov, I. Dhimitruka, G. R. Eaton, and S. S. Eaton, "New spectral-spatial imaging algorithm for full EPR spectra of multiline nitroxides and pH sensitive trityl radicals," *J. Magn. Reson.*, vol. 245, pp. 150 - 155, 2014.

[52] K.-H. Ahn and H. J. Halpern, "Spatially uniform sampling in 4-D EPR spectral-spatial imaging," *J. Magn. Reson.*, vol. 185, pp. 152-158, 2007.

[53] R. Owenius, G. R. Eaton, and S. S. Eaton, "Frequency (250 MHz to 9.2 GHz) and Viscosity Dependence of Electron Spin Relaxation of Triarylmethyl Radicals at Room Temperature," *J. Magn. Reson.*, vol. 172, pp. 168-175, 2005.

[54] B. Epel, G. Redler, and H. Halpern, "How *in vivo* EPR Measures and Images Oxygen," *Adv. Exp. Med. Biol.*, vol. 812, pp. 113-119, 2014.

[55] B. Epel, M. K. Bowman, C. Mailer, and H. J. Halpern, "Absolute oxygen R1e imaging in vivo with pulse electron paramagnetic resonance," *Magn. Reson. Med.*, vol. 70, p. 10.1002/mrm.24926, 2013.

[56] G. R. Eaton, S. S. Eaton, D. P. Barr, and R. T. Weber, *Quantitative EPR*. New York: Springer-Verlag/Wein, 2010.

[57] R. W. Quine, D. Mitchell, and G. R. Eaton, "A General Purpose Q-Measuring Circuit Using Pulse Ring-Down," *Conc. Magn. Reson., Magn. Reson. Engin.*, vol. 39B, pp. 43-46, 2011.

[58] G. Morris and P. Chilvers, "General Analytical Solutions of the Bloch Equations," *J. Magn. Reson., Series A*, vol. 107, pp. 236-238, 1994.

[59] A. Bain, C. Anand, and Z. Nie, "Exact solution to the Bloch equations and application to the Hahn echo," *J. Magn. Reson.*, vol. 206, pp. 227-240, 2010.

[60] Y. Shi, R. W. Quine, G. A. Rinard, L. Buchanan, S. S. Eaton, G. R. Eaton, B. Epel, S. W. Seagle, and H. J. Halpern, "Triarylmethyl Radical OX063d24 Oximetry: Electron Spin Relaxation at 250 MHz and RF Frequency Dependence of Relaxation and Signal-to-Noise," *Adv. Exp. Med. Biol.*, vol. 977, pp. 327 -334, 2017.

[61] A. Rajca, V. Kathirvelu, S. K. Roy, M. Pink, S. Rajca, S. Sarkar, S. S. Eaton, and G. R. Eaton, "A spirocyclohexyl nitroxide amino acid spin label for pulsed EPR spectroscopy distance measurements," *Chem. Eur. J.*, vol. 16, pp. 5778 - 5782, 2010.

[62] M. Tseitlin, A. Dhami, R. W. Quine, G. A. Rinard, S. S. Eaton, and G. R. Eaton, "Electron Spin T_2 of a Nitroxyl Radical at 250 MHz Measured by Rapid Scan EPR," *J. Appl. Magn. Reson.*, vol. 30, pp. 651-656, 2006.

[63] D. G. Mitchell, R. W. Quine, M. Tseitlin, R. T. Weber, V. Meyer, A. Avery, S. S. Eaton, and G. R. Eaton, "Electron Spin Relaxation and Heterogeneity of the 1:1 α,γ-Bisdiphenylene-β-phenylallyl (BDPA) : Benzene Complex," *J. Phys. Chem. B*, vol. 115, pp. 7986-7990, 2011.

[64] J. G. Powles, "The Adiabatic Fast Passage Experiment in Magnetic Resonance," *Proc. Phys. Soc.*, vol. 71, pp. 497-500, 1958.

[65] R. G. Parker and J. Jonas, "Adiabatic Fast Passage Method for Spin-Lattice Relaxation Time Measurements," *Rev. Sci. Instrum.*, vol. 41, pp. 319-321, 1970.

[66] T. Czechowski, M. Baranowski, A. Wozniak-Braszak, K. Jurga, J. Jurga, and P. Kedzia, "The Instrument Set of Generating Fast Adiabatic Passage," *J. Appl. Magn. Reson.* , vol. 43, pp. 331 - 340, 2012.

[67] S. S. Eaton, R. W. Quine, M. Tseitlin, D. G. Mitchell, G. A. Rinard, and G. R. Eaton, "Rapid Scan Electron Paramagnetic Resonance " in *Multifrequency Electron Paramagnetic Resonance: Data and Techniques*, S. K. Misra, Ed.: Wiley 2014, pp. 3 - 67.

[68] B. T. Ghim, S. S. Eaton, G. R. Eaton, R. W. Quine, G. A. Rinard, and S. Pfenninger, "Magnetic field and frequency dependence of electron spin relaxation times of the E' center in irradiated vitreous silica," *J. Magn. Reson. A*, vol. 115, pp. 230-5, 1995.

[69] C. Mailer, J. D. S. Danielson, and B. H. Robinson, "Computer-controlled pulsed electron-paramagnetic-resonance spectrometer," *Rev. Sci. Instrum.*, vol. 56, pp. 1917-1925, 1985.

[70] A. Carrington and A. D. McLachlan, *Introduction to Magnetic Resonance*. Harper and Row, pp. 202, 1967.

[71] Kispert, "Electron-electron double resonance," in *Biomedical EPR- Part B: Methodology, Instrumentation, and Dynamics*, vol. 24, S. S. Eaton, G. R. Eaton, and L. J. Berliner, Eds. (Biol. Magn. Reson.), New York: Kluwer Academic/Plenum Publisher, 2005, pp. 165-197.

[72] P. Spindler, P. Schops, A. Bowen, B. Endeward, and T. Prisner, "Shaped Pulses in EPR," *EMagRes,* vol. 5, pp. 1477-1492, 2016.

[73] R. H. Crepeau, A. Dulcic, J. Gorcester, T. R. Saarinen, and J. H. Freed, "Composite Pulses in Time-Domain ESR," *J. Magn. Reson.,* vol. 84, pp. 184-190, 1989.

[74] A. Doll, S. Pribitzer, R. Tschaggelar, and G. Jeschke, "Adiabatic and fast passage ultra-wideband inversion in pulsed EPR," *J. Magn. Reson.,* vol. 230, pp. 27-39, 2013.

[75] P. Spindler, S. Glaser, T. Skinner, and T. Prisner, "Broadband Inversion PELDOR Spectroscopy with Partially Adiabatic Shaped Pulses," *Angewandte Chemie,* vol. 52, pp. 3425-3429, 2013.

[76] N. Devasahayam, R. Murugesan, K. Matsumoto, J. B. Mitchell, J. A. Cook, S. Subramanian, and M. C. Krishna, "Tailored sinc pulses for uniform excitation and artifact-free radio frequency time-domain EPR imaging," *J. Magn. Reson.,* vol. 168, pp. 110-117, 2004.

[77] M. Tseitlin, R. W. Quine, S. S. Eaton, G. R. Eaton, H. J. Halpern, and J. H. Ardenkjaer-Larsen, "Use of the Frank Sequence in Pulsed EPR," *J. Magn. Reson.,* vol. 209, pp. 306-309, 2011.

[78] M. Tseitlin, R. W. Quine, S. S. Eaton, and G. R. Eaton, "Use of polyphase continuous excitation based on the Frank sequence for EPR," *J. Magn. Reson.,* vol. 211, pp. 221-227 2011.

[79] D. G. Mitchell, R. W. Quine, M. Tseitlin, S. S. Eaton, and G. R. Eaton, "X-band Rapid-Scan EPR of Nitroxyl Radicals," *J. Magn. Reson.,* vol. 214, pp. 221-226 2012.

[80] Poole, C. P. and H. A. Farach, "Electron Spin Resonance," in *CRC Handbook of Spectroscopy*, vol. II, J. W. Robinson, Ed. Cleveland: CRC Press, 1974, p. 215.

[81] A. Doll and G. Jeschke, "Fourier-transform electron spin resonance with bandwidth-compensated chirp pulses," *J. of Magn. Reson.,* vol. 246, pp. 18-26, 2014.

[82] P. Spindler, Y. Zhang, B. Endeward, N. Gershernzon, T. Skinner, S. Glaser, and T. Prisner, "Shaped optimal control pulses for increased excitation bandwidth in EPR," *J. Magn. Reson.,* vol. 218, pp. 49-58, 2012.

[83] H. B. Elajaili, J. R. Biller, S. S. Eaton, and G. R. Eaton, "Frequency Dependence of Electron Spin-lattice Relaxation for Semiquinones in Alcohol Solutions " *J. Magn. Reson.,* vol. 247 pp. 81 – 87 2014.

[84] H. B. Elajaili, J. R. Biller, M. Tseitlin, I. Dhimitruka, V. V. Khramtsov, S. S. Eaton, and G. R. Eaton, "Electron Spin Relaxation Times and Rapid Scan EPR Imaging of pH-sensitive Amino Substituted Trityl Radicals," *Magn. Reson. Chem.,* vol. 53, pp. 280 - 284, 2015.

[85] Poole, C. P. and H. Farach, "Handbook of Electron Spin Resonance." New York: Springer-Verlag, 1999.

Appendix A: List of Laura Buchanan Publications

Improved Sensitivity for Imaging Spin Trapped Hydroxyl Radical at 250 MHz, J. R. Biller, M. Tseitlin, D. G. Mitchell, Z. Yu, L. A. Buchanan, H. Elajaili, G. M. Rosen, J. P. Y. Kao, S. S. Eaton, and G. R. Eaton, *ChemPhysChem Comm.* 16, 528-531 (2014).

Imaging disulfide dinitroxides at 250 MHz to monitor thiol redox status, H. Elajaili, J. R. Biller, G. M. Rosen, J. P.Y. Kao, M. Tseytlin, L. A. Buchanan, G. A. Rinard, R. W. Quine, J. McPeak, Y. Shi, S. S. Eaton, G. R. Eaton, *J. Magn. Reson.* 260, 77-82 (2015).

UHF EPR spectrometer operating at frequencies between 400 MHz and 1 GHz. R. W Quine, G. A. Rinard, Y. Shi, L. A. Buchanan, J. R. Biller, S. S. Eaton, and G. R. Eaton *Conc. Magn. Reson.*, *Magn. Reson. Engineer*, 46B: 123–133, (2016).

Triarylmethyl Radical: EPR Signal to Noise at Frequencies between 250 MHz and 1.5 GHz and Dependence of Relaxation on Radical and Salt Concentration and on Frequency. Y. Shi, R. W. Quine, G. A. Rinard, L. A. Buchanan, S. S. Eaton, G. R. Eaton, B. Epel, S. W. Seagle, H. J. Halpern, *Z Phys. Chem*. 231(4), 923-937, (2017).

Triarylmethyl Radical OX063d24 Oximetry: Electron Spin Relaxation at 250 MHz and RF Frequency Dependence of Relaxation and Signal-to-Noise. Y. Shi, R. W. Quine, G. A. Rinard, L. A. Buchanan, S. S. Eaton, G. R. Eaton, B. Epel, S. W. Seagle, and H. J. Halpern. *Adv. Exp. Med. Biol.* 977, 327-334, (2017).

Rapid-Scan EPR Imaging. S. S. Eaton, Y. Shi, L. B. Woodcock, L. A. Buchanan, J. McPeak, R. W. Quine, G. A. Rinard, G. R. Eaton. *J. Magn. Reson*. 280, 140-148, (2017).

Resonators for In Vivo Imaging: Practical Experience. G. A. Rinard, R. W. Quine, L. A. Buchanan, S. S. Eaton, G. R. Eaton, B. Epel, S. V. Sundramoorthy, and H. J. Halpern. *J. Appl. Magn. Reson.* 48, 1227-1247 (*2017*).

An X-Band Crossed-Loop EPR Resonator. G. A. Rinard, R. W. Quine, J. McPeak, L. A. Buchanan, S. S. Eaton, and G. R. Eaton. *J. Appl. Magn. Reson.* 48, 1219-1226 (2017).

Background Correction in Rapid Scan EPR Spectroscopy. L. A. Buchanan, L.B. Woodcock, R. W. Quine, G.A. Rinard, S.S. Eaton, G.R. Eaton. *J. Magn. Reson.* 293, 1-8, (2018).

Table-top 700 MHz EPR Imaging Spectrometer. L. A. Buchanan, G.A. Rinard, R. W. Quine, S. S. Eaton, G. R. Eaton. *Conc. Magn. Reson., Magn. Reson. Engineer.* accepted.

250 MHz Rapid Scan Cross Loop Resonator. L. A. Buchanan, G. A. Rinard, R. W. Quine, Y. Shi, S. S. Eaton, G. R. Eaton. *J. Appl. Magn. Reson.* submitted.

Appendix B: List of Abbreviations

API	Application Programming Interface
AWG	Arbitrary Waveform Generator
B_0	Magnetic field
B_1	Microwave magnetic field
CLR	Cross Loop Resonator
CW	Continuous Wave
EPR	Electron Paramagnetic Resonance
FBP	Filtered Back Projection
FID	Free Induction Decay
FT	Fourier Transform
FWHM	Full Width Half Maximum
G	Gauss
GCD	Greatest Common Denominator
LGR	Loop Gap Resonator
NF	Noise Figure
NMR	Nuclear Magnetic Resonance
OD	Outer Diameter
Q	Quality Factor
RS	Rapid Scan
RSCD	Rapid Scan Coil Driver
RF	Radio Frequency

SPU	Signal Processing Unit
SR	Saturation Recovery
T_1	Spin-lattice relaxation time constant
T_2	Spin-spin relaxation time constant
T_m	Phase memory time constant
UHF	Ultra High Frequency, includes 700 MHz
VHF	Very High Frequency, includes 250 MHz